Analysis of Glycerophospholipids and Sphingolipids in Murine Brain Using Liquid Chromatography – Electrospray Ionization - Tandem Mass Spectrometry and Matrix-Assisted Laser Desorption Ionization – Imaging Mass Spectrometry

Thao Nguyen

This thesis is submitted to the Faculty of Graduate and Postdoctoral Studies in partial fulfillment of the requirements for the Master's degree in Chemistry.

Department of Chemistry & Biomolecular Sciences
Faculty of Science
University of Ottawa

This thesis and all of my moral as well as intellectual faculties are dedicated to my mother, the strongest and bravest person I have ever come to know.

"*It is our choices, Harry, that show what we truly are, far more than our abilities.*"

- Albus Dumbledore –

TABLE OF CONTENT

ABSTRACT

Mass spectrometry is an indispensable tool in lipidomics research. Current advances and progress in the technology of mass spectrometry have allowed for the identification, quantification and characterization of lipid molecular species to further our understanding of their biological roles. In this thesis, I assessed the influence post-mortem times have on quantitative lipidomics. Using liquid chromatography - electrospray ionization tandem mass spectrometry (LC-ESI-MS/MS) on a triple-quadrupole mass spectrometer and multiple-reaction-monitoring (MRM) mode, the glycerophosphocholine (GPC) metabolites and second messengers in the hippocampus of N3 & N4 C57BL/6 x 129/SV were profiled at various post-mortem interval (PMI). I found that disruption to the GPC metabolite and second messengers lipidome occured as early as 1 hour post-mortem and fluctuate up till at least 12 hours post-mortem. Therefore, PMI is a variable in lipidomic studies that must be controlled for, and brain samples which are collected with PMI variations must be matched to avoid misinterpretation. Subsequently, I developed a working protocol to visualize the location and distribution of different classes of glycerophospholipids, ceramides, and sphingomyelin in whole mouse brain sections. This visualization technique is novel because it does not require tissue staining or immunohistochemistry; instead, it was performed using an atmospheric-pressure matrix-assisted laser desorption/ionization (AP-MALDI) source coupled to an orbitrap mass spectrometer. As part of this lipid visualization technique, I also developed a protocol for sublimation as a simple, effective and reproducible matrix application method for brain tissue. The lipid-compatible matrix, 2,5-dihydroxybenzoic acid (DHB), was assessed and optimized for imaging lipid targets. The high mass-resolution and accuracy characteristics of the orbitrap mass spectrometer and its capability to perform tandem mass spectrometry via high-collision dissociation allowed for the identification of approximately 200 different lipid species directly from brain tissue using the visualization technique I developed.

Altogether, the work in this thesis has showed that post-mortem changes in the lipidome are quantifiable and has provided a novel avenue to further assess these changes by means of imaging mass spectrometry.

ACKNOWLEDGEMENT

There were times when all of this would have been a mere imagination. Those were when I was never able to imagine myself having a chance to practice science outside of the textbook, to expand my understanding of the universe, to do something meaningful, at least to myself.

I would never be where I am today if it was not for my mother who has worked so hard her whole life just to give me a better education, and just so I could pursue my passion even if that would take forever. She has loved and supported this wild-spirited and wandering child in me all the way through.

Part of this thesis is also dedicated to Eunnara Cho. Thank you for loving me and your patience for me, who at times I myself can hardly bear. You have introduced me to a world so simple yet amazingly beautiful.

I am indebted to Mr. Caskanette, my very first chemistry teacher who always had faith in me even when I doubted myself the most, who spent time listening to my stories, and allowing me to practice chemistry in his classroom during lunches and after school. Casper, I owe my success and my scientific achievement today to you. (and yes, I have stopped trying to put my hand into a beaker of acetone!)

I would like to thank my supervisor Dr. Maxim Berezovski, for giving me the golden opportunity to pursue my Master's study in his laboratory and introducing me to the awesome project in which I was fortunate to take part. Thank you for all the supports and guidance.

I would like to express my sincerest gratitude to my co-supervisor Dr. Steffany Bennett. Thanks Stef for having faith in me, from day one of knowing me. Thanks for being much more than a supervisor. You are a true mentor, a source of inspiration, a friend who I can always come to for ideas and, of course, problems.

I need to thank Dr. Ignacio. I got a chance to encounter this brilliant scientist and wonderful human being half way into my M.Sc., at the point where I was so clueless and lost. He reminded me the meaning of practicing science, and why I was motivated to be in this field in the first place. Most of all, he taught me the beauty of never stop learning in science, that no technique stands alone on its own as the ultimate solution to all problems, that different techniques, just as different minds, work together to answer questions. And that is where **good** science unites this world.

I can't thank Drs. Darija "Magic" and Ana, and Nadia Al-Youssef enough for keeping me sane this long. They have helped me so much from the beginning and their support is still ongoing (plus the chocolate they share!). Thank you, Arlen, for all the "meowy" times, for her unconditional love and listening ears that kept me company all throughout my thesis. Also huge thanks to Pavel, Evan, Chris, Shahrokh, Sam Sherman, Mark Akins, Matthew Granger, Dr. Hongbin Xu, Graeme McDowell and all of the members, past and present, of both Berezovski and Bennett labs. Humble thanks to Dr. Sharon Curtis and Dr. Sander Mommers from the John Holmes Mass Spectrometry Facility, who truly opened my eyes to the world of mass spectrometry and were always willing to offer suggestions and inputs to my learnings.

Thanks, Gleb for your constant mockery. Although you were truly annoying, I must admit that it did make a better me by motivating myself to know better. Yes, just so I can argue with you.

Thanks 'Estie' – my beloved mass spectrometer for being very cooperative (at times) during the last year and a half. We took time to know each other, went through some tough times but learned from each other so much from that. You have been a good peer all along.

Everyone, at different points in their life, picks up something to be a source of motivation to help them go through life. Some are temporary, some carry sentimental values of a loved one or memorable past, some could be joy, and some are scars. Growing up, I befriended books and fell in love with my own imagination. Three important people who have made up a me of today are

Socrates, Professor Einstein and Madame Curie. They are the inspiration of my dedication to life-long learning and remind me constantly to never stop examining my thoughts and actions, valuing mistakes, accept my limits but keep working to go beyond them. I thank them for their enormous contributions to humanity and for being the role models I always look up to.

And finally, I want to offer my deepest gratitude to my extended family in Canada, who has been there for me since my first day in this country. They always play the biggest supporting role in every step I take in my life. While watching my growth quietly, they are the "home" I always end up coming back to, where I feel the constant love, care, support and understanding, despite how strongly it is storming outside.

PREFACE

Lipids are forgotten molecules in biochemistry. When lipids are introduced in biochemistry textbooks, they are often limited to their roles in membranes (namely, the phospholipid bilayer) and as an energy source for cellular function (such as triacylglycerols). Little emphasis is placed on the fact that, besides being structural building blocks of cell membranes, lipids also actively serve as bioactive autacoids and second messengers transducing signals initiated at membrane boundaries[1]**.** The seemingly dull role of lipids could be blamed on the central dogma of biochemistry, which reads that (almost) all of life is coded by the nucleic acids that make up our genes, which produce the proteins required to catalyze all biochemical pathways, and ultimately carry out, maintain and repair all cellular processes. This dogma relegates lipids to function as a gate, or a boundary against intruders, for the more important machinery is coded in our genome and translated into our proteome.

Another part of the reasons why lipids have not gained sufficient appreciation and recognition for their role, frankly, is because we do not understand them well enough. Subtle structural differences, defined, for example, by a single acetyl group or the presence or absence of a double bond in a hydrocarbon chain, confers lipid identity at the molecular level[2]. Hence, individual species are difficult to separate and identify. The role this structural diversity has on function is not as intuitive as is the structural underpinning of protein conferring a lock-and-key model of enzyme's activity, or the mis-folding of a protein as a result of an upstream missense mutation[3]. This diversity begs the question: Why do we have so many different lipid species? If one was to extrapolate the area of a single cell's plasma and intracellular membranes, the extended bilayer would cover an area of over tens of thousands of square meters[4]. Perhaps, when there is so much of something, we tend to fail to appreciate it fully. To quote Sir Arthur Conan Doyles' character, Sherlock Holmes: "There is nothing more deceptive than an obvious fact." The precise yet diverse

lipid composition of membranes of cellular and subcellular compartments co-exists with the tightly regulated biochemical processes of lipid remodelling that regenerates structural lipids while transiently producing bioactive second messengers. Clearly, one cannot fully grasp the insights into how living systems work without understanding the functions and roles of membranes and their lipid constituents.

The life sciences have just witnessed the past era of genomics, is witnessing the current era of proteomics rapidly revealed, and has begun to witness the emerging era of lipidomics starting to unfold. Within the last decade, lipidomics has separated itself from the realm of metabolomics. As an emerging field, lipidomics seeks to better understand the lipid composition at the molecular level, map changes in diseased states, and extrapolate function to establish how lipid composition regulates cell function. Hence, the motivation of this thesis is to participate in further understanding the complexity of biological lipidome by exploiting different lipid-centric developments in mass spectrometry (MS) as the analytical tool.

LIST OF EQUATIONS

LIST OF FIGURES

LIST OF TABLES

LIST OF ABBREVIATIONS

9-AA	9-aminoacridine
AA	Arachidonic acid
AC	Alternating-current
AD	Alzheimer's disease
ACN	Acetonitrile
AGC	Automatic Gain Control
AMU	Atomic mass unit
ANOVA	Analysis of variance
AP	Atmospheric pressure
ATP	Adenosine triphosphate
ADP	Adenosine diphosphate
CAD	Collision-activated-decomposition
CCD	Charged-coupled device
CDP	Cytidine-5'-diphosphocholine
Cer	Ceramide
CID	Collision-induced dissociation
CSF	Cerebrospinal fluid
DAN	1,5-diaminonapthalene
DC	Direct-current
ddMS/MS	Data-dependent tandem mass spectrometry
DHB	2,5-dihydroxybenzoic acid
DMAN	1,8-bis-(dimethyl-amino) naphthalene
DNA	Deoxyribonucleic acid

ESI	Electrospray ionization
eV	Electrovoltage
FA	Formic acid
FDR	False discovery rate
FFA	Free fatty acid
FF	Formalin-fixed
FFPE	Formalin-fixed and paraffin embedded
FT-ICR	Fourier-transform ion cyclotron resolution
FWHM	Full-width at half-maximum
GP	Glycerophospholipid
GPA	Glycerophosphatidic acid
GPC	Glycerophosphocholine
GPE	Glycerophosphoethanolamine
GPI	Glycerophosphoinositol
GPS	Glycerophosphoserine
HCD	High-energy C-trap dissociation
HPLC	High-performance/pressure liquid chromatography
HR-MS	High-resolution mass spectrometry
IMS	Imaging mass spectrometry
IR	Infrared radiation
ISD	In-source decay
IT	Injection time
LIT	Linear ion trap
LIPID MAPS	LIPIDS metabolites and pathways strategy

LPCAT	*lyso*-phosphatidylcholine acyltransferase
LPC	1-acyl-*sn*-glycero-3-phosphocholine (*or, lyso*-phosphatidylcholine)
LPC(*O*)	1-alkyl-*sn*-glycero-3-phosphocholine
LPC(*P*)	1-alkenyl-*sn*-glycero-3-phosphocholine (*or, lyso*-plasmalogen PC)
LPAF	*lyso*-platelet activating factor (*or,* 1-alkyl-*sn*-glycero-3-phosphocholine, see LPC(*O)*)
MALDI	Matrix-assisted laser desorption ionization
MRM	Multiple reaction monitoring
MS	Mass spectrometry
MS/MS	Tandem mass spectrometry
NP-HPLC	Normal-phase HPLC
ns	Nanosecond
OCT	Optimal cutting temperature
PAF	Platelet-activating-factor
PAF-AH	Platelet-activating-factor acetylhydrolase
PB	Phosphate buffer
PC	1-Acyl-2-acyl (diacyl) -*sn*-glycero-3-phosphocholine / phosphatidylcholine
PC(*O*)	1-alkyl-2-acyl- *or* 1-alkyl-2-alkyl- *or* 1-alkyl-2-acetyl- (see PAF) -*sn*-glycero-3-phosphocholine
PC(*P*)	1-alkenyl-2-acyl-*sn*-glycero-3-phosphocholine (*or* plasmenyl, *or* plasmalogen)
PDF	Pulsed dynamic focusing
PE	1-Acyl-2-acyl (diacyl) -*sn*-glycero-3-phosphoethanolamine / Phosphatidylethanolamine
PFA	Paraformaldehyde

PG	Phosphatidylglycerol
PIS	Precursor ion scan
PLA_1	Phospholipase 1
PLA_2	Phospholipase 2
PLS-DA	Partial least square discriminant analysis
PMI	Post-mortem interval
PNA	*p*-nitroaniline
PUFA	Polyunsaturated fatty acid
QqQ	Triple quadrupole
RF	Radio frequency
RP-HPLC	Reverse-phase HPLC
RNA	Ribonucleic acid
ROS	Reactive oxygen species
RT	Retention time
SEM	Standard error of the mean
SM	Sphingomyelin
sn	Stereospecifically numbered
TFA	Trifluoroacetic acid
TLC	Thin layer chromatography
TOF	Time-of-flight (mass spectrometer)
UV	Ultraviolet
VIP	Variable importance plot

CHAPTER ONE: GENERAL INTRODUCTION

1.1 THE METABOLISM OF GLYCEROPHOSPHOCHOLINES (GPCS)

This thesis focuses primarily on exploring new methods of imaging glycerophospholipids (GPs), and to a lesser extent sphingolipids and cholesterol, in brain and addressing critical changes in lipid metabolism post-mortem that could impact on lipidomic assessment of lipid signatures of human disease using post-mortem tissue. As such, I begin first with reviewing the metabolism of the primary lipid subclass of interest, GPCs. GPCs are a subclass of GPs, the major lipid constituent of cellular membranes in all organisms[5-6]. GPs are chemically defined as the derivative of a phosphorylated glycerol molecule[7-8]. The position of the phosphate group is ***s****tereospecifically* ***n****umbered (sn)* at position 3 on the naturally occurring L-glycerol[9]. Hence GPs are a family of lipids derived from *sn*-glycero-3-phosphoric acid, which assumes the replacement of the two remaining hydroxyl groups at position *sn*-1 and *sn*-2 on the glycerol by two fatty acids[7-8]. The head-group substituent that is esterified to the phosphate group at the *sn*-3 position determines the subclass: a choline head group signifies glycerophosphocholines (GPC), an ethanolamine head group signifies glycerophosphoethanolamines (GPE), a serine head group signifies glycerophosphoserines (GPS) and an inositol head group signifies glycerophosphoinositols (GPI). At the *sn*-2 position, the fatty acid is most commonly esterified to the glycerol, and this linkage is known as *O*-acyl[10]. Ether linkage at *sn*-2 is also possible although much less observed[11-12]. On the other hand, the fatty acid residue at the *sn*-1 position could contain the *O*-acyl, or *O*-alkyl (ether) or *O*-alk-1'-enyl (vinyl ether or alkenyl) linkage (Figure 1.1)[11-13]. The alkyl-acyl GPC with the *O*-alkyl linkage at the *sn*-1 position comprises the precursor for the powerful ether lipid platelet-activating-factor (PAF, 1-alkyl-2-acetyl-*sn*-glycero-3-phosphocholine), a pro-inflammatory molecule that can cause platelet aggregation[14]. The alkenyl-acyl GPC with the *O*-alk-1'-enyl

Figure 1. 1. Structure of glycerophosphocholines (GPC).

GPs are derived from glycerol. Fatty acids (hydrocarbons, R1 and R2) are linked to the glycerol backbone at the stereospecifically-numbered (sn) position 1 and 2, while a phosphate group is esterified to the glycerol at position sn-3. The phosphate group carries functional group moiety that determines the class of glycerophospholipid, such as a hydrogen atom (glycerophosphatidic acid, GPA), a choline (glycerophosphocholine, GPC), an ethanolamine (glycerophosphoethanolamine, GPE), an inositol (glycophosphoinositol, GPI), a glycerol (phosphoglycerol, PG), a serine (glycerophosphoserine, GPS). Hydrocarbons are commonly esterified to the glycerol at sn-2 (with rare exceptions), whereas three types of linkage are possible at sn-1 position. These are ester, alkyl ether, alkenyl ether linkages dividing GPs into three subclasses known as O-acyl, O-alkyl ether, O-vinyl ether GP, respectively. Hydrocarbon chains (R1 and R2) that dictate molecular identity of individual species within subclasses are defined by their number of carbons and degrees of unsaturation in addition to linkage to the glycerol backbone.

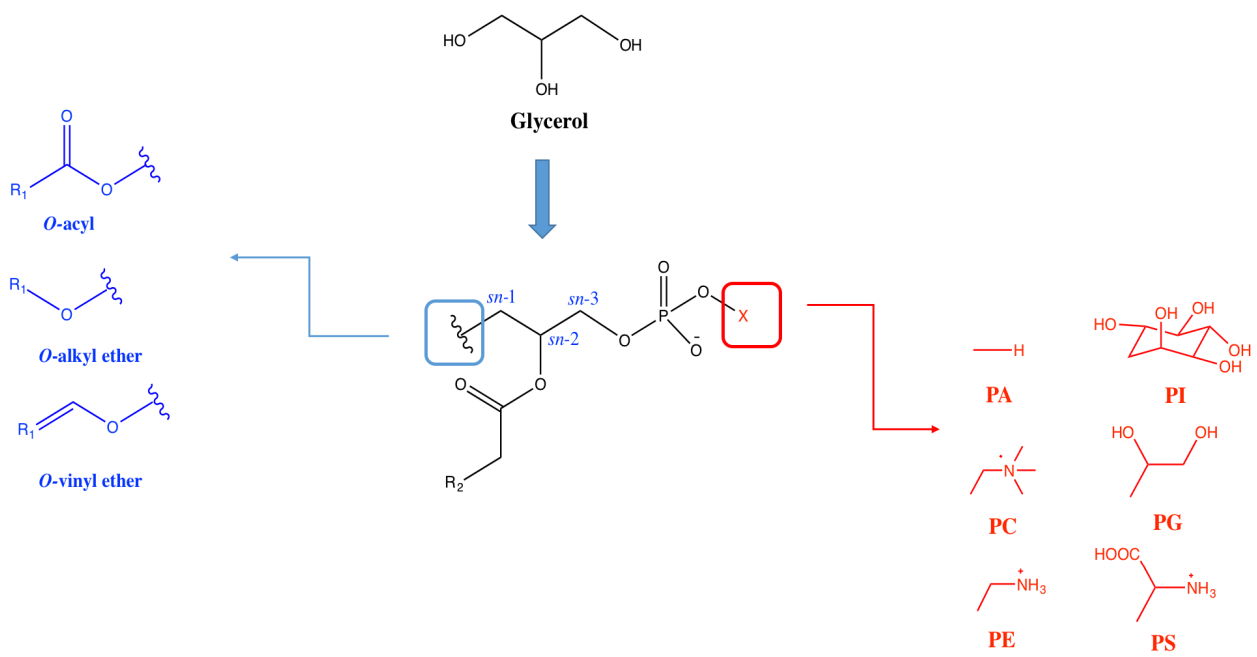
Glycerol
O-acyl
O-alkyl ether
O-vinyl ether
sn-1
sn-2
sn-3
X
PA
PI
PC
PG
PE
PS

linkage at the *sn*-1 position defines the lipid class of plasmalogens (1-alkenyl-2-acyl-*sn*-glycero-3-phosphocholine), which are very abundant in the neuronal membrane[13]. The alkyl ether and vinyl ether linkages are usually abbreviated as *O*- or *P*-, respectively, followed by the notation of fatty acyl chain (number of carbons : number of unsaturation), as described in most literatures as well as in the database of the LIPIDS Metabolites and Pathways Strategy (LIPID MAPS) consortium[15].

In this thesis, the nomenclature for GPCs is as follows: the 1-acyl-2-acyl linkage is referred to as PC (phosphatidylcholine); 1-alkyl ether-2-acyl linkage is referred to as PC*(O);* and 1-alkenyl-2-acyl linkage is referred to as PC*(P*) or plasmalogen PC. When these lipids undergo *sn-2* hydrolysis (where the *sn*-2 fatty acyl chain is removed from the glycerol backbone), the ester linkage is reduced to an alcohol group, converting the molecule into a *lyso*-GP. The notation for these hydrolyzed structures will only indicate the one *O*-acyl linkage in position *sn*-1 and written as LPC, LPC(*O*), and LPC(*P*) for *lyso*phosphatidylcholines, 1-alkyl-*sn*-glycero-3-phosphocholine (or *lyso*-PAF), and 1-alkenyl-*sn*-glycero-3-phosphocholine (or *lyso*-plasmalogen PCs), respectively. Following the above notation, the number of carbon present in each fatty acyl chain at the *sn*-1 and *sn*-2 position and the number of unsaturation units at each position are further indicated. This is indicated by (carbon number at *sn-1* : unsaturation unit / carbon number at *sn-2* : unsaturation unit). In cases where the exact molecular structure of each fatty acyl chain is not known but the GP mass is known, the total number of carbons and unsaturation units is predicted and written as (total carbon number : total unsaturation unit). For example, PC(16:2/16:0) can also be referred to as PC(32:2) if exact *sn*-1 and *sn*-2 structure was not identified.

Among all the GPs that make up the membrane, GPCs are the most abundant[16-18]. Within the GPC subclass, PCs alone comprise 70% of membrane phospholipids in mammalian cells[19-20]. The GPC component of cell membrane is the reservoir of free fatty acids (FFA) and second metabolites

that are bioactive mediators and important for many cellular processes[21]. Accumulating evidence has shown that in patients with Alzheimer's disease (AD), break-down of neuronal membrane as a result of extensive metabolism of GPC decreases PC content in both the cerebrospinal fluid (CSF)[22] and post-mortem brain[20, 23-24]. Within the brain, both PC and diacyglycerophosphoethanolines (PE) showed a significant decrease in the parietal and frontal cortex of AD patients compared to healthy controls[25]. Breakdown products of PC, such as LPC and FFA, in turn, increase following these degradation events. Hence, the profiles of not only GPCs but also their metabolites reflect different physiological states in diseased versus healthy metabolism.

Although the cell membrane is often represented as a well-structured "wall" of phospholipids, this wall is anything but rigid. Instead, the cell membrane is very dynamic and undergoes constant remodeling[26]. The most abundant components of this wall, GPCs, are continuously catabolized to LPCs, LPC(*O*)s, and LPC(*P*)s (where the specific metabolite produced depends on type of linkage between the GPC backbone and the fatty acid). These metabolites can then be anabolized enzymatically to PCs, PC(*O*)s or LPC(*P*)s, respectively, depending on the availability of FFA conjugated to co-enzyme A (CoA) in the membrane. The LPCs, LPC(*O*)s and LPC(*P*)s are important molecules in cell signaling. LPC specifically is synthesized enzymatically from PC by phospholipase A1 (PLA_1) and phospholipase A2 (PLA_2)[27]. These enzymes hydrolyze the acyl ester bond at the *sn*-1 or *sn*-2 position, respectively. The lack of a hydrophobic fatty acyl chain causes LPCs to have less amphipathic character than their parent PCs and hence unfavorable for membrane-forming[28]. Consequently, the presence of LPCs in the plasma membrane disturbs its structure and increases its permeability. LPCs have been suggested to participate in cell membrane fusion, and consequently mediates intercellular communication and signalling[29-30]. The role of LPCs have also been extended to regulate the activity of membrane-bound receptors and

enzymes[31-32]. In the brain, it was proposed to be an effective carrier of docosahexaenoic acid through the blood-brain barrier and may also participate in neurotransmitter release[33]. Under normal physiological condition, LPCs appear to be active molecules that are constantly involved in metabolic processes and are found at low concentrations[34]. However, in pathological conditions, LPCs tends to accumulate and are known to cause neuron demyelination and break-down of the blood-brain barrier[35].

A constant remodelling cycle of de-acylation and re-acylation known as the Land's Cycle is absolutely critical for maintaining the homeostasis of cellular phospholipids and FFA (Figure 1.2)[26, 36]. Remodeling is mediated by PLA_2; there is little known, however, about the role of PLA_1[37]. Polyunsaturated FAs (PUFA) are commonly found at the *sn*-2 position of most GPs. One particular PUFA, arachidonic acid (AA), is of particular interest due to the preference of cytoplasmic PLA_2 ($cPLA_2$) for GPs with AA at the *sn*-2 position. Upon hydrolysis, AA is released and can be further metabolized into another class of molecules known as eicosanoids, which participate in many important cellular processes[17, 37-38]. If conjugated to CoA, AA can be re-incorporated into the Land's cycle to generate new GP species through the actions of acyl-CoA lysophospholipid transferases[39]. There are four lysophosphatidylcholine acyl transferases (LPCATs)[40], all of which are involved in PCs and PAFs remodelling pathways[41-44] . Two of the LPCAT enzymes, specifically LPCAT1[44] and LPCAT2[42], are capable of transferring acyl-CoA chains to both ester- and ether-linked PCs. When LPC(*O*)s, are generated from an *O*-alkyl-ether-linked PC(*O*) at the *sn*-1 position they become precursors for PAFs[45]. The addition of an acetyl group at the *sn*-2 position of an LPC(*O*) by LPCAT1 or LPCAT2 converts *lyso*-PAFs to

Figure 1. 2. Land's cycle of GPC remodelling

Land's cycle GPC remodeling. Structural GPCs found in membranes are constantly used to generate enzymatically important signaling molecules and second messengers that are, in turn, remodeled back to structural membrane lipids. The phospholipase 2 (PLA_2) family of enzymes is responsible for hydrolyzing GPC at the sn-2 position, yielding a FFA and an LPC. These enzymes can also hydrolyze PC(O) and PC(P) generating LPC(O) and LPC(P) respectively. The reverse reaction of this process is carried out by the LPCATs using acyl-CoA to re-acylate a FFA at the sn-2 position. LPCATs can also convert LPC(O) to PAFs via acetylation at the sn-2 position using acetyl-CoA as well as PAF-like "acyl-PAFs" and alkenyl-PAFs. The three PAF-AH enzymes carry out the reverse reaction by removing the acetyl group and re-forming LPC(O). PAF-AH 1b specifically hydrolyzes ether-linked PAFs. Secreted PAF-AH and PAF-AH II are more promiscuous and can hydrolyze acyl-PAFs and alkenyl-PAFs. In addition, PAF-AH II has acetyl-transferase activity and can acetylate nearby lipid substrates.

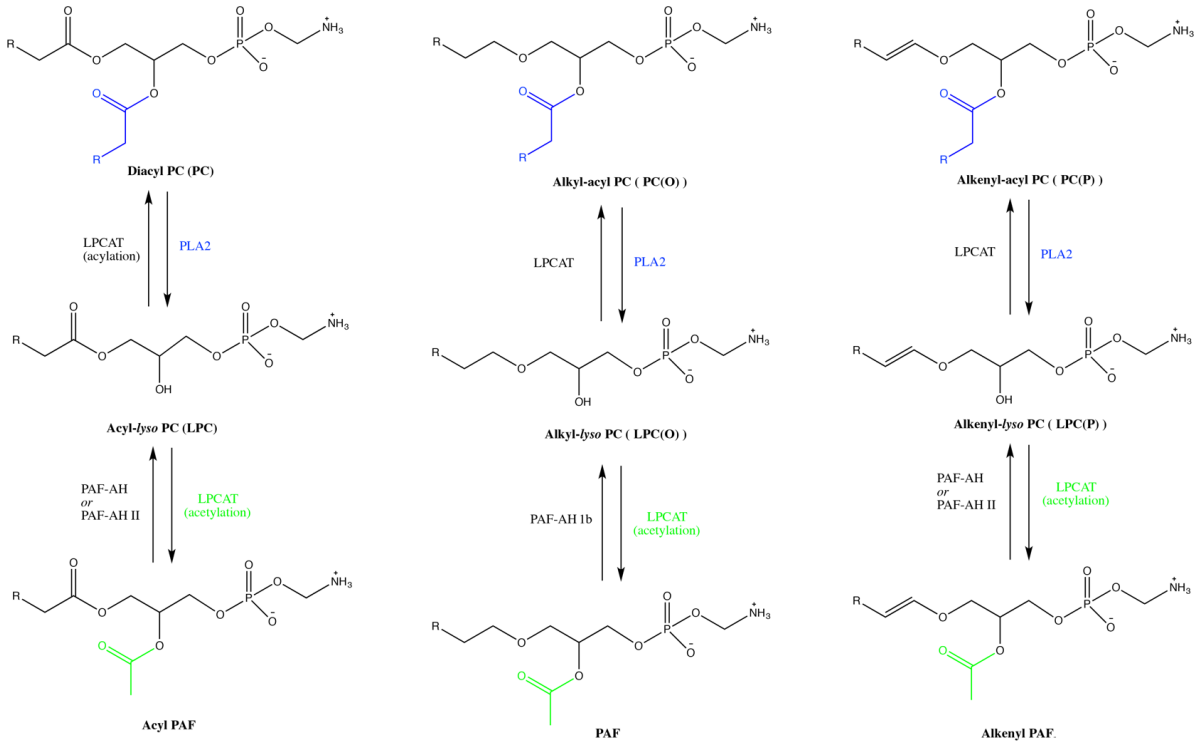
Diacyl PC (PC)
LPCAT
(acylation)
PLA2
Acyl-lyso PC (LPC)
PAF-AH
or
PAF-AH II
LPCAT
(acetylation)
Acyl PAF
Alkyl-acyl PC (PC(O))
LPCAT
PLA2
Alkyl-lyso PC (LPC(O))
PAF-AH 1b
LPCAT
(acetylation)
PAF
Alkenyl-acyl PC (PC(P))
LPCAT
PLA2
Alkenyl-lyso PC (LPC(P))
PAF-AH
or
PAF-AH II
LPCAT
(acetylation)
Alkenyl PAF.

PAFs[42, 46]. Likewise, LPCs and LPC(P)s can be converted to acyl-PAFs and plasmenyl-PAFs, respectively. The reconversion of PAFs back to *lyso*-PAFs involves the deacetylation of the acetyl group at the *sn*-2 position by one of three PAF-acetylhydrolases (PAF-AH1b, PAF-AHII and secreted PAF-AH)[47]. Interestingly, PAF-AHII also has transferase activity such that it can transfer the acetyl directly from PAF to another *lyso*-GPC, thus generating acyl-PAFs or alkenyl-PAFs[48]. The *lyso*-PAF metabolite can in turn be remodelled back to an *O*-alkyl-ether linked PC(*O*) by LPCAT using acyl-CoA as a substrate[17, 49-51].

1.2 MASS SPECTROMETRY (MS) IN LIPID ANALYSIS

1.2.1 Ionization techniques

Lipidomics depends upon MS. In MS, ionization should be considered the most important step. To be detected and analyzed by the mass spectrometer, a molecule must carry one or more charges. At first, MS was not possible for the analysis of biomolecules. It was designed to study more volatile molecules that can transit into the gas phase easily, such as small organic compounds. The analysis of biological macromolecules was made possible by the introduction of soft ionization techniques, such as electrospray ionization (ESI) in the 1960s-1980s[52] and matrix-assisted laser desorption ionization (MALDI) in the 1990s[53]. Unlike earlier ionization methods such as electron impact, ionization methods such as ESI and MALDI do not require molecules to be in the gas phase for ionization. Furthermore, molecules ionized by ESI or MALDI may be kept intact before entering the mass spectrometer for further analysis. This is especially useful for separating and analyzing biomolecules from complex matrices, when their structural identities correspond to their mass-to-charge (m/z) ratio, or the molecular peaks, and not peaks that are of their fragments. Soft ionization is also able to minimize in-source decay/fragmentation (ISD), an event where the analytes are activated to fragment after receiving excess energy during ionization[54]. This event occurs in the source, which can lead to complications in interpretation of ion signals in the mass

spectra. ISD is not very common in ESI, although the two can be coupled to work together in specific sophisticated experiments. More commonly, ISD is coupled with MALDI. In MALDI, laser energy can be controlled in order to reduce ISD events. Alternatively, the technology of atmospheric-pressure (AP) MALDI can also be adapted, which has been reported to be a softer ionization method than vacuum MALDI[55].

Lipid molecules are non-volatile and thermal-labile; given that lipids are comprised mostly of carbon, hydrogen, oxygen, nitrogen and phosphate, their structures are best analyzed intact, before fragmentation is performed by a mass spectrometer. This way, the molecular and structural information necessary for identification of molecular identity is retained, and reliable species quantification is also possible. Hence, the ability to ionize intact lipids using soft-ionization methods without ISD and fragmentation is important for lipid analysis. There are many different ways to ionize lipids[56-57]; however, only ESI, MALDI and AP-MALDI will be discussed, as per the scope of the research presented in this thesis.

i. ESI

(a) Principles of ESI

MS analyzes molecules in their gaseous state. ESI efficiently produces these gas phase ions from lipid molecules. The electrospray phenomenon generally consists of three events[58], beginning from the moment sample is sprayed from the ESI capillary to when it is transferred into the mass spectrometer at the sample cone (stage 1 – 3 in Figure 1.3).

Stage 1. Production of charged droplets (nebulisation)

This is the event at which ions of either positive or negative polarity accumulate at the tip of the ESI capillary. To generate charged droplets from a solution eluting from either a syringe pump

Figure 1. 3. Schematic diagram of the ionization event by electrospray ionization (ESI)

Samples are introduced to the ESI source via direct infusion (by a syringe pump) or following LC. Samples are then sprayed from the ESI capillary going through 3 stages to form gaseous ions before entering the mass spectrometer. At stage 1, charged droplets are formed. At stage 2, the charged droplets start shrinking due to application of desolvation gas, leading to accumulation of charges and surface tension on the shrinking droplet. At stage 3, the droplet bursts when these charged repulsion approaches Rayleigh's limit and produce gas-phase ions. As samples are sprayed from the ESI capillary and form charged droplets, a constant electric field is applied between the capillary and the mass spectrometer inlet, effectively rendering the ESI source an electrophoretic apparatus.

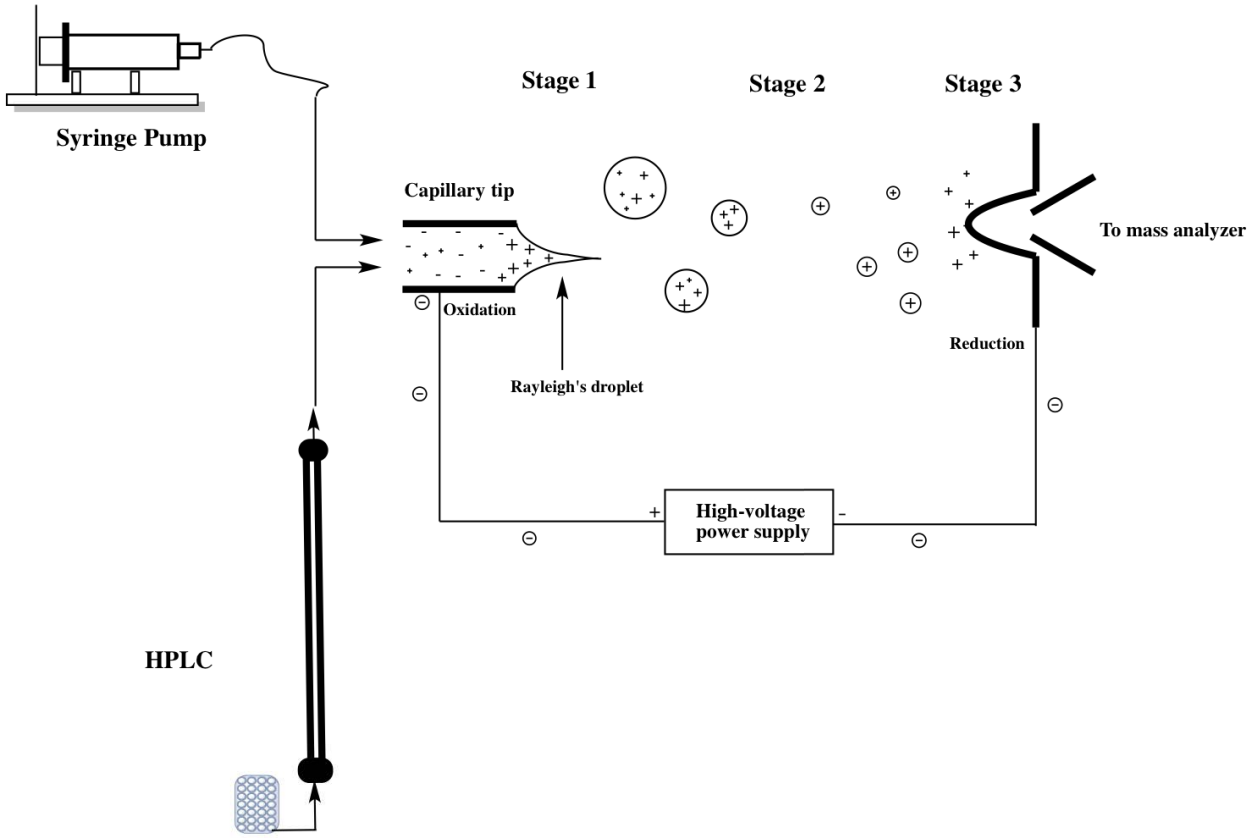
Syringe Pump
Stage 1
Stage 2
Stage 3
Capillary tip
To mass analyzer
Oxidation
Reduction
Rayleigh's droplet
High-voltage
power supply
HPLC

or HPLC, an electric field is first applied to the solution flowing in the capillary. This electric field is produced by the generation of a potential difference between the capillary and the MS inlet opposite from it[59]. In positive-ion mode, the capillary is an anode while the sample cone is a cathode. As sample flows through the capillary, electrons are drawn from the solution; positive ions then repel from the capillary wall, concentrate, and accumulate at the tip of the ESI capillary. In negative-ion mode, the reverse occurs. These electrophoretic phenomena characterize the ESI source as an electrochemical cell. Oxidation occurs at the capillary tip and reduction occurs at the MS inlet in positive-ion mode.

Stage 2. Shrinkage of charged droplets

By combining several optical diagnostic techniques, Gomez and Tang[60] were able to capture an image of the droplet as it develops at the tip of the ESI capillary. Generally, the first step is the formation of a spherical drop in the last few micrometers of the capillary. As more ions accumulate, charge density increases due to Coulombic repulsion and these pressures elongate the drop at the capillary tip. Finally, when enough charge accumulates and the increased Coulombic repulsion matches the surface tension of the sample's solvent, the drop reaches what is known as the Rayleigh's limit and breaks, forming a cone-like shape at the tip of the capillary. This is known as Taylor's cone. and is the point at which spraying occurs[52, 59-61].

Stage 3. Production of gas-phase ions

In order to explain the transition from Coulombic repulsion of charges to release of gas-phase ions, there are two accepted theories: the charged residue theory[62] and the "evaporation" theory of ions from small droplets[63]. In the first theory, Dole *et al* propose that after Taylor's cone is formed, droplet fission occurs. This allows offspring droplets of smaller size to form from the parent droplets at the beginning of the spray. These offspring droplets get smaller and smaller, until each one carries only a single ion. Finally, the ion is released into the gas-phase when desolvation

occurs. In the second theory, based on an ion mobility experiment, Iribarne and Thomson suggest that ions within droplets whose radii are less than 10 nm can "evaporate" and escape into gas phase. This theory was based on the finding that there were a significant number of gas phase ions existing when the droplet was still considerably larger than an ion and was carrying multiple charges. Although the two ideas do not support one another, together they could explain how ESI is able to form both single-charged and multiple-charged ions.

Two other factors that occur during the ESI event that should be mentioned are nebulisation and desolvation. During nebulisation (stage 1), a stream of gas is applied outside of the capillary, coaxially to the outcoming flow of samples, to assist with droplet formation. At stage 2, after Taylor's cone is formed, the droplets encounter a stream of heated, inert gas (usually nitrogen) that causes desolvation to remove solvent from samples[59].

The development of ESI has allowed lipids to be analyzed intact, in solution, and away from oxygen (thus avoiding any secondary oxidation reactions due to extensive exposure to air)[64]. ESI further enables the analysis of numerous lipid species from a complex matrix at the same time. ESI, either by itself or coupled to a separation technique such as HPLC, is a powerful technique for lipidomic research.

(b) Direct infusion - shotgun lipidomics

Application of ESI in lipidomics is very diverse due to its effective ionization ability and the ability to easily couple ESI to other devices. Shotgun lipidomics was termed by Han and Gross[65] and Ejsing *et al* in 2004, and it refers to the direct introduction of lipid extracts to the mass spectrometer without prior separation[66]. As the name implies, the purpose of this approach is to analyze lipids from biological samples on a large scale by maximally exploiting all characters of all lipid classes and species[67]. Shotgun lipidomics allows the discovery of novel lipid species because there are no complications by chromatographic separation. Furthermore, the molecular

ions of all lipid species are displayed in one mass spectrum, allowing for easy, direct spectra comparisons from different samples. This feature is also beneficial for quantification by direct infusion/ESI of lipids. In this kind of shotgun analysis, lipid extracts are introduced into the ESI source at one specific flow rate via a syringe pump (flow rate of μL / min),[68] after which they are sprayed into the mass spectrometer. The lipid extracts could also be introduced directly into the mass spectrometer via a static nano-ESI-source without a syringe pump, at a much lower flow rate of nL/min[69]. Because there is no pre-mass spectrometer separation, all lipid species are analyzed at a constant concentration and at the same time. As a result, integration of peak intensity is also uniform among all ions[70]. By manually adding an internal standard for each lipid class present in the extract, quantitation of endogenous lipid species can be performed effectively in direct-infusion. Post-source analyses of lipids, such as tandem MS-approaches or high-mass accuracy analysis that are usually done with liquid chromatography-based lipidomics, are also compatible with direct infusion methodologies.

(c) Lipid analysis with separation – liquid chromatography-based lipidomics

In lipid analysis, ESI can also act as the interface between chemical and mass-to-charge separation. Chemical separation is carried out by HPLC, in which different lipid species are separated by differences in their hydrophobicity. The eluted analytes are then introduced to the mass spectrometer and further separated by a mass-to-charge ratio (m/z). The separation by HPLC operates based on the principle of attraction between molecules with similar chemical properties, *i.e.,* polarity[71]. Compounds within a mixture are separated as they elute from a tightly packed column with just a few micrometers in diameter. The column support is usually silica, but other polymers, such as polystyrene, may also be used. The silica surface contains an acidic, hydrophilic silanol functional group (Si-OH), which can react with other functional groups and results in an increased hydrophobicity of the column (Figure 1.4A, B and C). Altogether, this constitutes the

stationary phase of the column. Differences in hydrophobic interactions between biomolecules and the stationary phase leads to biomolecules exiting the column at different times, which in turn results in differences in retention times (RT) among the biomolecules. This resolution between biomolecules can be enhanced by the choice of solvent system; the solvent system is also known as the mobile phase.

In general, there are two types of HPLC: normal-phase (NP) and reverse-phase (RP). Each method is useful for different purposes in lipid separation. NP-HPLC is commonly used to separate different classes of lipids, while RP-HPLC resolves individual species within a lipid class[70]. In NP-HPLC, the stationary phase is polar; hence, the silica support may retain the silanol group, or it may be slightly modified by the addition of less hydrophobic groups, such as a cyano group or a short hydrocarbon chain. The mobile phase is non-polar and highly hydrophobic. Common choices include hexane and tetrahydrofuran. By contrast, RP-HPLC requires modifications to the silica support by addition of hydrophobic groups, such as long chain hydrocarbons (e.g. C18), to create a non-polar stationary phase. The mobile phase is polar and the most common choices are water, alcohol and acetonitrile[71]. In terms of choosing the type of hydrophobic alkyl chain for the stationary phase, the chain length is important and depends on the size of the analyte[72]. For example, a larger molecule with many hydrophobic moieties on its structure would be able to interact with the polar stationary phase well; hence, a choice of C4 would be a more appropriate choice over C18.

Figure 1. 4. Schematic illustration of the silica network formed by Si-O-Si bridges.

(A) The silanol -OH groups are on the surface of the silica bead. This group can chemically react with other less polar groups, such as the C4 chain, to form the butyl silyl-moiety on silica as in **(B)**. Other common choices for R-groups to create the stationary phase with a desired polarity are depicted in **(C)** with hydrophobicity characters indicated. Figures were adapted from Harris 2007 (Reference 71).

A

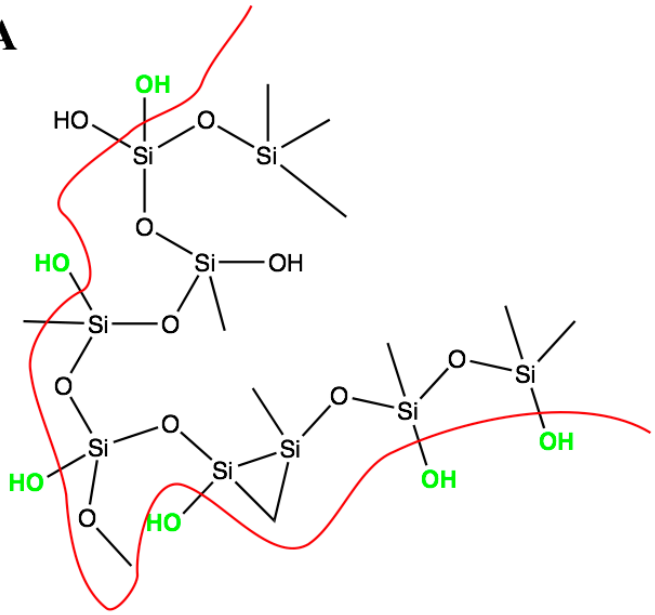

B

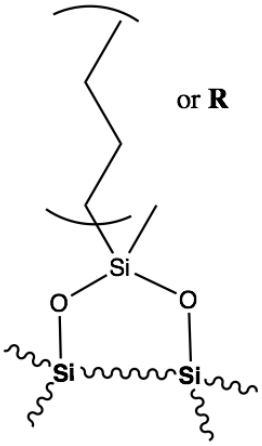

C

R	Structure	Hydrophobicity
Amino	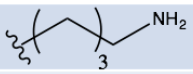	
Phenyl	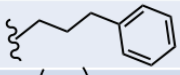	
Cyano	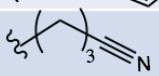	
C4 (butyl)	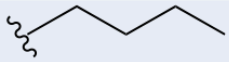	
C8 (octyl)	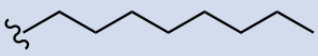	
C18 (octadecyl)	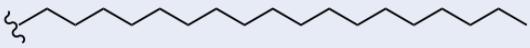	

The selection of HPLC method to be applied for lipid separation heavily depends on the focus of the study. GPs are the major class of membrane lipids[3, 17]. They are amphipathic in nature due to their polar head-group and non-polar fatty acid chains at the *sn-1* and *sn-2* linkages. Because the head-group is polar, they can interact with the stationary phase during NP-HPLC separation. Hence, NP-HPLC is used to separate lipid classes based on the differences in head-groups[70]. The polarity and acidity of a functional group are strongly related; therefore, the relative polarity of each phospholipid class can be predicted based on its pKa. The elution conditions of the HPLC column commonly contain a small addition of trifluoroacetic acid (TFA) or formic acid (FA), keeping the mobile phase pH around 1.5-2.2[72]. At this pH, only the phosphoric acid functional group becomes deprotonated. The presence of additional functional groups in the phosphate affects this pKa, therefore changing the polarity of the head-group. Phosphatidic acid (PA) contains only a phosphate head-group, with two ionizable protons. The pKa of the first proton is 3.0, while the pKa of the second proton is 8.0. The first proton on the phosphate group is compared to other ionizable protons on other head-groups. In increasing order, the pKa of GPC, GPE, GPS, GPI, and phosphatidylgylcerol (PG) are 1.0, 1.7, 2.5, 2.5, and 2.9 respectively[73-74]. Increasing pKa corresponds to a decreased acidity and polarity. Hence, the hydrophobicity of all head-groups (hence the resulting phospholipid) can be ranked as follows: choline (PC) < ethanolamine (PE) < serine (PS) = inositol (PI) < glycerol (PG) < hydrogen (PA). Therefore, in NP-HPLC, GPCs would spend the most time interacting with the polar column, while GPA would elute from the system first (Figure 1.5). Overall, NP-HPLC is a useful method to separate different classes of lipids in biological extracts.

On the other hand, RP-HPLC operates under reverse conditions compared to NP-HPLC; RP-HPLC has a non-polar stationary phase and a polar mobile phase. The silica base of the column is

Figure 1. 5. Normal-phase high-performance liquid chromatography (NP-HPLC).

In NP-HPLC, lipids are separated based on the interaction of their head-groups with the polar column. Each head-group (showed above as hydrogen, glycerol, inositol, serine, choline, ethanolamine) contains different functional groups and it is the phosphoric acid proton ($-HPO_4$) that becomes deprotonated during the separation condition (mobile phase contains 0.1% TFA, giving pH of 1.8-2.0). Examining the pKa of each head-group, GPC would interact most with the polar column while GPA elutes very quickly due to its lower polarity at this pH. Predicted eluting sequence of different lipid classes is: GPA, GPG, GPS=GPI, GPE, GPC.

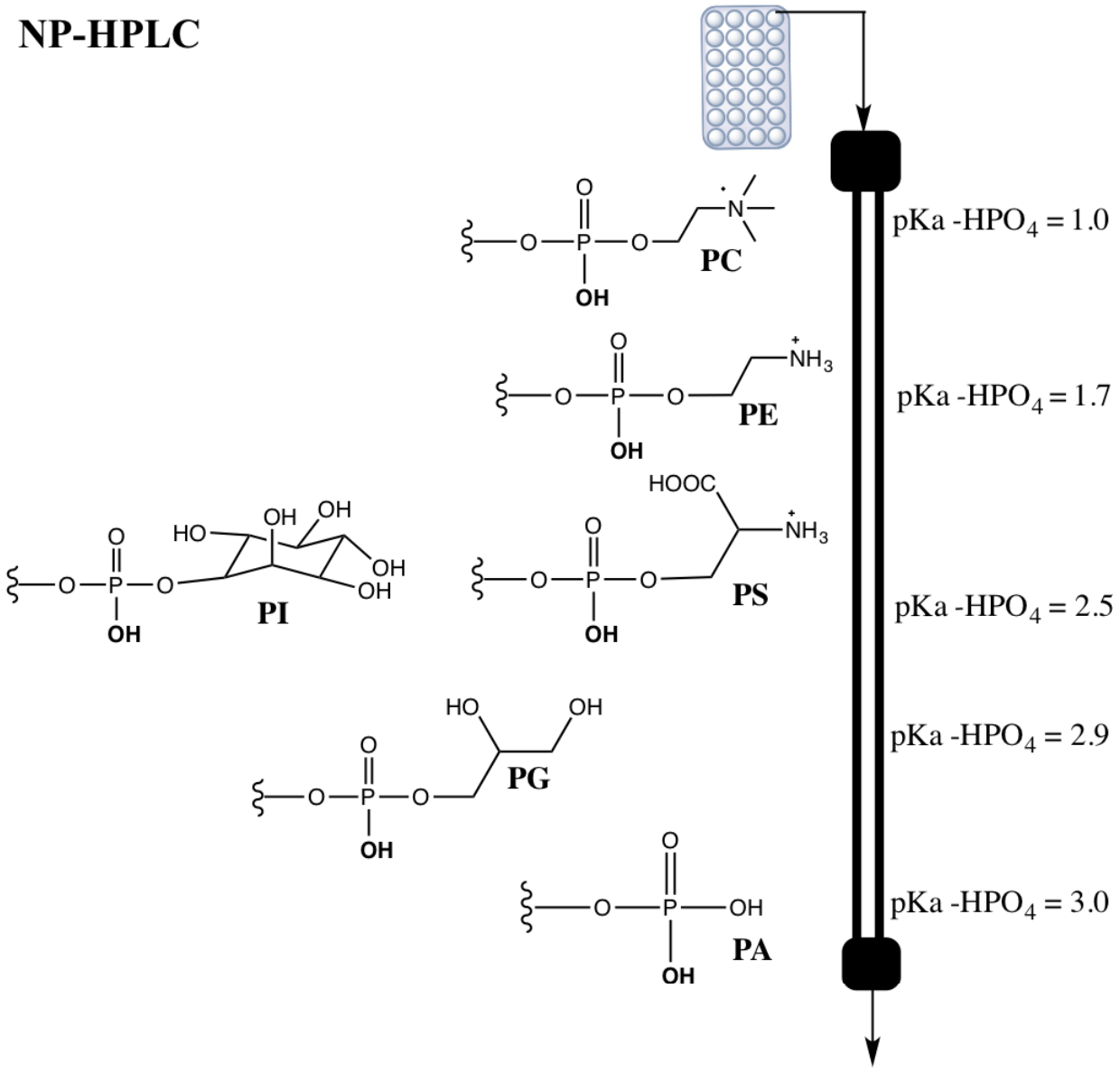
NP-HPLC
PC
PE
PI
PS
PG
PA
pKa -HPO4 = 1.0
pKa -HPO4 = 1.7
pKa -HPO4 = 2.5
pKa -HPO4 = 2.9
pKa -HPO4 = 3.0

usually modified to reduce polarity by covalently bonding it to a nonpolar functional group. Long hydrocarbon chains are often used to accomplish this reduction in polarity, as shown in Figure 1.5C. The mobile phase in RP-HPLC contains two solvents, A and B, which are by convention aqueous (water) and organic, respectively. Most often, the mobile phase contains a small addition of acid such as TFA or FA; the acids act as a proton source as well as to improve signal[72]. In RP-HPLC, lipid molecules are separated based on the hydrophobic interaction between the fatty acyl chains with both the non-polar stationary phase and the polar mobile phase. The hydrophobicity of fatty acyl chains depends on the length, number, and configuration of unsaturation of the chain. An increasing chain length corresponds to a higher hydrophobicity, while multiple unsaturations decrease hydrophobicity[67]. Because lipids from different classes can have similar molecular weights and degrees of hydrophobicity, using RP-HPLC to resolve lipid molecules in a mixture of different classes can be quite complicated. Thus RP-HPLC is more useful when separating individual lipid species within a pre-isolated lipid class of interest.

There are several advantages to performing HPLC separation prior to MS analysis of lipid extracts. First and foremost, separation simplifies the analysis step, which usually involves samples containing numerous classes of lipids, and a large number of species within each class. Modification and optimization of the separation technique would lead to better resolution and detection of individual lipid species. One issue in direct-infusion MS is that the more abundant lipid species can suppress signals from low-abundance species, as direct infusion is performed on complex lipid extracts. HPLC separation reduces this effect of ion suppression and allows low-abundance species to be detected[12]. Furthermore, HPLC is also very powerful for the identification of lipid molecules by providing an extra parameter, RT, to each detected species in addition to the m/z signal found by MS[56]. The RT of each lipid molecule is tied to its hydrophobicity character. Lipids with similar masses can still be separated by using their different RTs. Correct identification

of lipid species is very important, especially when quantification is desired to enhance the understanding of lipidomic changes in different disease states. Using a combination of NP-HPLC and RP-HPLC to create a two-dimensional separation setup would make separating lipid classes and species possible and enrich the analysis of lipids in biological extracts[70]. Overall, LC, coupled to ESI-MS, plays an essential role in discovering novel lipid species and is the gold standard in lipidomics.

ii. MALDI

(a) Principle of MALDI-MS

MALDI is a method of ionizing molecules for mass spectrometric analysis by, as the name implies, desorption with the assistance of a matrix compound. Hence, the principle of ionization by MALDI relies strongly on the ability of the analytes to desorb[75]. This characteristic of MALDI involves two main contributors: a laser light source and a laser light-absorbing compound - the matrix[76].

Common MALDI laser sources includes both an infrared (IR) and an ultraviolet (UV) lamp; the latter, however, being more popular. The main difference between the two laser sources lies in the duration of the radiation pulse: an IR source produces a longer pulse that lasts from 6 - 200 ns, while a UV-based pulse is very short, approximately 3-10 ns[76]. A shorter pulse duration is preferred for ionization, as it is able to effectively cause fast ablation of the sample with little or no thermal degradation[77]. In addition to duration of the pulse, another parameter known as "laser fluence" is also important in sample ablation and ion generation. Laser fluence is the amount of energy, in this case optical energy, delivered per unit of area in one laser pulse[76]. The commonly-seen unit of laser fluence in MALDI-MS is W/cm^2 and it varies based on the laser light source and combination of analyte and matrix system. This is due to the fact that different matrix compounds absorb laser light differently, and that each is able to assist in the ionization of the analyte with

different efficiency[78]. Generally, ion formation occurs at or above the threshold laser fluence, which is approximately 10^6 (W/cm^2)[76]. Laser sources that are capable of short pulse-duration paired with a suitable matrix and analyte combination can lower this threshold, leading to effective analyte ablation and ion formation. Figure 1.6A represents a schematic diagram of the MALDI process at the interface of the source and the mass spectrometer inlet, where desorption, ionization, extraction and transmission of ions occur.

(b) Matrices in MALDI of lipids

The core principle of MALDI lies in the ability of the chemical matrix compounds to form microcrystals in a homogeneous distribution among the analytes, to absorb laser energy effectively, and to transfer this energy to the surrounding analyte molecules, leading to desorption[79]. These are probably the only processes in the MALDI method that are understood with certainty. In contrast, the ionization mechanism of the analyte following the event of energy transfer is still not thoroughly understood, and very few successful efforts have been made to deduce the molecular processes behind this[80].

During the sample preparation step in MALDI, care is taken to maximize the matrix's effectiveness at desorption and ionization. The concentration ratio of matrix to analyte sample is determined experimentally, and usually differs between high-molecular weight molecules and small molecules (for example, proteins versus lipids). In proteomics, peptide or protein analytes are highly saturated by the matrix; thus matrix to protein ratios of 500:1 or even 1000:1 are very common[81]. In lipidomics, depending on the abundance of the particular lipid species of interest, the molar ratio of matrix to lipid is often much less than 500:1. Adjustment of matrix to analyte ratio is based on the signal to background noise ratio. Lipid concentrations that are too low produce very poor ion signal, whereas high lipid concentrations lead to complete suppression of the signal[81]. The same holds true for matrix concentration[82]. Therefore, the proper molar ratio of

matrix to lipid is often solved empirically. Generally, the amount of matrix applied needs to be abundant enough to prevent the analyte molecules from forming clusters with one another[83], and to absorb the laser wavelength strongly and sufficiently enough to, upon evaporation, generate molecular ions of the analytes[84].

In general, most matrices used in positive ion mode are weak acids, which often have aromatic compounds with carboxylic acid functional group(s) attached. These acids are capable of giving off an H^+ for subsequent ionization of the analytes, while basic compounds are used in negative ion mode for efficient abstraction of protons from the analytes[79, 85]. Several matrices have been demonstrated to be effective for lipid analysis. These include 2,5 dihydroxybenzoic acid (DHB)[85-86] and 1,5-diaminonapthalene (DAN)[87] for both positive and negative ion mode, and 9-aminoacridine (9-AA)[88], *p*-nitroaniline (PNA)[89], and (DMAN)[90-91] for negative ion mode. These matrices are preferred due to their ability to incorporate well into lipid analytes to generate a homogeneous co-crystal[84], to produce simple matrix-compound spectra in which only few matrix background signals are observed[85], and to enhance the ion signal of the lipid analytes.

(c) Ionization mechanism in MALDI

There are multiple separated events that occur and make up the entire process of MALDI. These are (1) the ionization of the matrix[92], (2a) the desorption of the matrix, leading to (2b) the desorption of the analyte[77], and (3) the ionization of the analyte[92]. Within this set of events, (2a) and (2b) are probably the best understood. The ionization event of the matrix in (1) is straight-forward, while there are multiple competing theories proposed to explain the ionization of the analyte in (3). In this section, I will summarize the generally-accepted explanation for the desorption events of (2a) and (2b), and I will briefly discuss the two most popular theories that explain the ionization events of the matrix (1) and of the analyte (3) (Figure 1.6B).

The most important role of the matrix compound in MALDI is to absorb the energy at the specific wavelength emitted by the laser. This is the reason why most MALDI matrices are aromatic compounds[84]. Following absorption, the laser energy is quickly converted into thermal energy by the matrix solid crystals, causing a partial sublimation of these crystals). As mentioned earlier, matrix and analytes are mixed so as to form homogenous co-crystals. Hence, as the crystals desorb, they also pull some of the intact analyte into the vapor phase of the expanding plume. The next step, which is ionization of the analyte, requires the matrix to first be charged. The matrix, either a weak acid (used in positive ion mode) or a base (used in negative ion mode), is charged using photoionization. This event is summarized by the following set of equations[54, 76, 92], in which *m* is the matrix*, e* represents electrons, while H represents a hydrogen atom (proton):

$$m \xrightarrow{h\nu} m^{**} \longrightarrow m^{\bullet +} + e^{-} \qquad \textbf{(Equation 1.1)}$$

$$m + e^{-} \longrightarrow m^{\bullet -} \qquad \textbf{(Equation 1.2)}$$

$$m^{\bullet +} + m \longrightarrow [m + H]^{+} + [m - H]^{\bullet} \qquad \textbf{(Equation 1.3)}$$

$$m^{\bullet -} + m \longrightarrow [m + H]^{-} + [m + H]^{\bullet} \qquad \textbf{(Equation 1.4)}$$

Following photoionization, the matrix molecules are excited and receive enough energy for the photoelectric effect to occur, which results in the release of an electron (likely the delocalized π electrons of the aromatic ring) to produce positive matrix ions (Equation 1.1). This photoelectron collides with another neutral matrix molecule, giving rise to a negative matrix ion (Equation 1.2). Hence, both positive and negative matrix ions, as well as their derivatives, are produced; however,

Figure 1. 6. The process of matrix-assisted laser desorption/ionization (MALDI) and formation of ions.

The process of MALDI and formation of ions are illustrated in (A) and (B) respectively. (A) Nitrogen laser source emits light at 337 nm focused at a lens and an angled mirror such as reflected light intersects the mobile X-Y stage which holds the sample stainless steel plate. Sample (red) and matrix (cyan) compounds are deposited onto the plate such that both co-crystallize on the plate. Upon laser firing, matrix absorbs laser energy and releases an electron due to the photoelectric effect. Subsequent collision with other neutral matrix leads to formation of protonated matrix (Event 1, 2a and 2b). Desorption of the matrix brings with it the co-crystallized neutral sample molecules. Gas-phase proton-transfer between the protonated matrix ion and the neutral sample, leads to formation of protonated sample ions (Event 3). Schematic depicts gas-phase ionization model that explains the ionization mechanism by MALDI.

A)

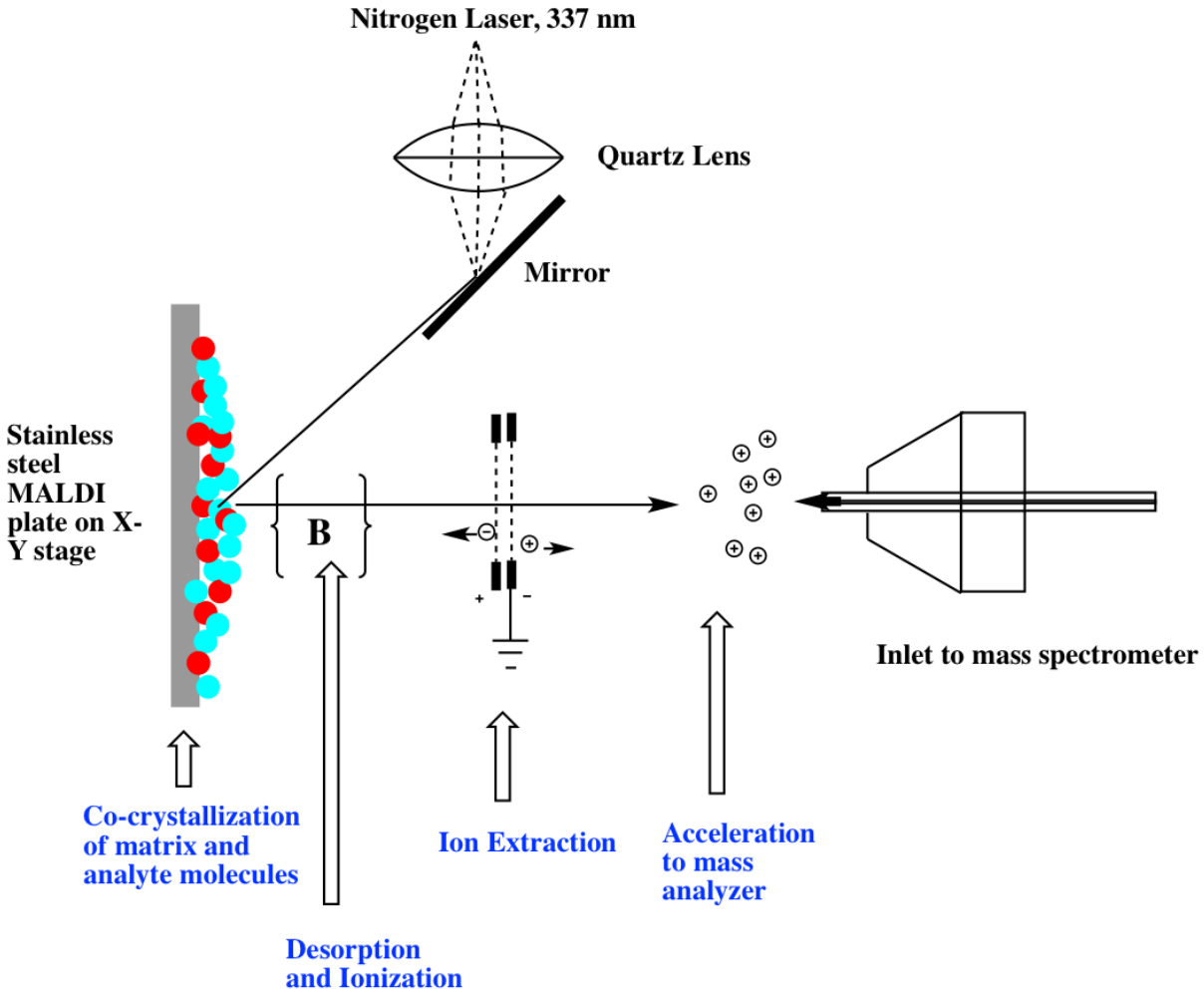
Nitrogen Laser, 337 nm
Quartz Lens
Mirror
Stainless steel MALDI plate on X-Y stage
B
Inlet to mass spectrometer
Co-crystallization of matrix and analyte molecules
Ion Extraction
Acceleration to mass analyzer
Desorption and Ionization

B)

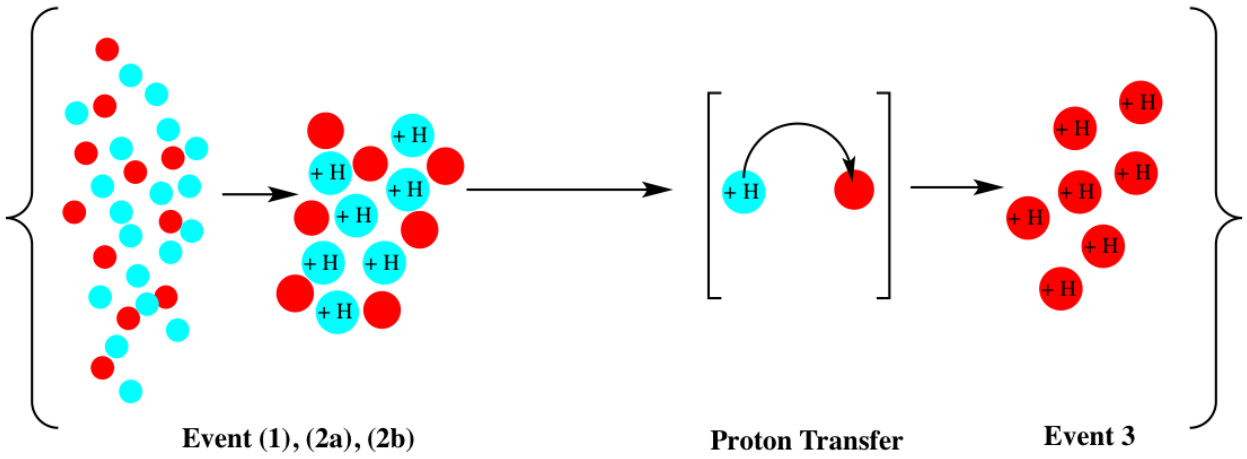
+ H
Event (1), (2a), (2b)
Proton Transfer
Event 3

the operating polarity of the mass spectrometer determines which one is detected. Further products are derived from the collision of the positively-charged or negatively-charged ions and other neutral matrix molecules, leading to proton transfers between molecules and giving rise to protonated or deprotonated matrix ions (Equation 1.3 and 1.4).

Success of photoionizing the matrix is important for subsequent ionization of the analyte. Reports have shown that a good yield of matrix ions (approximately 10^{-4} or 10^{-5} ions to neutral molecules)[93-94] leads to high intensity of analyte ions (up to 10% higher than that of the matrix signals)[95]. The signals of these two entities are dependent on each other; hence, it is strongly believed that a charge transfer event occurs after photoionization of the matrix[92]. There are currently two competing theories that explain how analyte molecules receive their charges: the gas-phase ionization theory and the Lucky Survivor model[96].

In the gas-phase ionization theory, it is argued that as analytes and matrix ions are vaporizing in the expanding plume post-photoionization, protons from protonated matrix ions (generated as shown in Equation 1.1-1.4) are transferred from the matrix to the neutral analytes in positive-ion mode[92, 96-99]. In contrast, proton abstraction occurs in negative-ion mode. This model relies on gas-phase collision and gas-phase proton affinity or basicity of both the matrix and the analytes.

In the Lucky Survivor model, ions are theorized to be pre-charged in the matrix crystal before desorption [100-101]. This model applies to MALDI experiments in which the analyte solution is prepared with the typical addition of TFA to induce protonation[76, 79]. For example, in traditional MALDI (spot-MALDI), the analyte solution is usually mixed with the matrix solution before spotting on the MALDI plate, followed by solvent evaporation and matrix-analyte co-crystallization. A similar procedure is applied in MALDI-imaging MS, in which the matrix solution is sprayed to coat the tissue sample.

In this thesis, sublimation, a dry and solvent-free method of matrix application, is used. Thus, it is more likely that the event of analyte protonation occurs according to the gas-phase protonation theory than the Lucky Survivor model. Regardless, both models assist in explaining different aspects of MALDI desorption and ionization. Jaskolla and Karas have showed that both theories contribute greatly to elucidation of the overall mechanism of MALDI, and both theories successfully highlight the important fact that following ionization, singly-charged ions dominate the MALDI mass spectra[102].

(d) Atmospheric-pressure MALDI

Atmospheric-pressured (AP) MALDI operates at atmospheric pressure, outside of the vacuum environment of the mass spectrometer. The nature of vacuum MALDI requires that it is built inside the mass spectrometer, such as in the popular incorporation of a MALDI source in a time-of-flight instrument. AP-MALDI, however, allows for the easy installation and removal of the source from any mass spectrometer that has an atmospheric pressure interface[80]. For this reason, it is possible to couple AP-MALDI with AP ionization sources such as ESI.

One of the main advantages of AP-MALDI over traditional vacuum MALDI is its ability to reduce in-source decay, which affects labile molecules such as lipids and peptides. This is a phenomenon commonly observed with vacuum MALDI. Generally after desorption in vacuum MALDI, ions emerge from the matrix embedment, and their internal temperature is raised due to 1) the energy the matrix absorbs from the laser, 2) the collision of ions with matrix molecules and the subsequent transfer of the very efficiently-absorbed laser energy, and 3) the effect by the electric field at the interface between the MALDI plate and the capillary inlet that is meant for transfering ions[92, 103]. All of these factors contribute to increasing the temperature of the ions, which makes them prone to fragmentation before entering the mass spectrometer. In AP-MALDI, thermalization of the matrix and of analytes takes place more easily and efficiently after laser

irradiation, leading to very few fragmentations in the source[80]. Indeed, AP-MALDI is considered to be a softer method of ionization than traditionally MALDI.

In the past, the efficiency of ion transfer in AP-MALDI was a concern due to its ambient-pressure operation. When it was first introduced in 2000 by Laiko[104], the transmission of ion into the vacuum of the mass spectrometer required the assistance of a continuously applied electric field and by a flow of dry nitrogen gas. Even so, transmission efficiency was still poor and this diminished the usefulness of AP-MALDI when compared to vacuum MALDI. Ions formed in an atmospheric environment disperse more easily and tend to get lost before being transmitted into the mass spectrometer. The most recent version of AP-MALDI has been improved by adding the technology of pulsed dynamic focusing (PDF) into the source to enhance ion transmission[55]. The PDF setup converted the continuous ion-extraction by electric field into pulsed-extraction, in which the high-voltage electric field between the MALDI target plate and the mass spectrometer inlet is removed temporarily for a very short amount of time (less than 1 ms). This removal period is known as hold time, and is meant to allow ions to travel into the mass spectrometer by following the intake flow field of the instrument's inlet. Hence, PDF technology allows the user to manipulate the guiding of ions into the instrument by controlling the amount of time before the removal of the electric field (known as "delayed time"). To summarize, following the event of laser firing and ion generation, ions are faced with a high-voltage electric field that is removed after a set delayed time. By the time the electric field is removed, the ions are sufficiently close to the MS inlet to be drawn into the mass spectrometer by the intake flow field, which is believed to be more efficient in transmitting ions than the pre-MS-inlet electric field. A benefit of the availability of PDF is that it allows the user to have better control over ion transmission, as well as the ability to tune the source and instrument to achieve an optimized condition for ionization.

AP-MALDI offers a flexible option for the ionization source as it is easy to switch with other AP sources. It is also very convenient for optimization; the source and the instrument are two separate entities, and changing parameters in one does not affect the other. The much softer ionization ability of AP-MALDI, compared to traditional MALDI, makes AP-MALDI an ideal ionizer for labile biomolecules such as lipids, with the additional possibility of imaging the distribution of biomolecules on tissue surfaces.

1.2.2 Mass analyzers

After ionization, ions are transferred into the mass analyzer so they can be separated based on their m/z. An analyte may carry a single or multiple charges depending on the nature of the molecules, the sample preparation, and the mode of ionization. Currently available mass spectrometers commonly contain more than one fundamental mass analyzer. In this thesis, lipids were analyzed and quantified on a triple-quadrupole mass analyzer and imaged on a quadrupole-orbitrap mass spectrometer.

i. Quadrupole and triple quadrupole (QqQ)

A quadrupole is a mass-analyzer itself, able to filter ions based on their m/z. The quadrupole contains two pairs of hyperbolic rods; each pair carries a polarity (positive or negative). The two rods in each pair are positioned parallel to each other, and the two polarities are anti-parallel, forming a structure as per Figure 1.7. One pair carries positive potential energy (Equation 1.5), while the other carries negative potential energy (Equation 1.6)[105-106]:

$$\phi = + (U - V \cos \omega t) \qquad \text{(Equation 1.5)}$$

Figure 1. 7. Schematic diagram of a 2D-quadrupole mass analyzer

Ions are trapped and separated in a three-dimensional radio frequency quadrupole, which is made up of four cylindrical electrode rods. Opposite rods carry the same potential. As ions enter the quadrupole, they are selected based on their trajectories, which are affected by the voltage applied to the rods. The trajectories, ultimately are directly associated to their m/z.

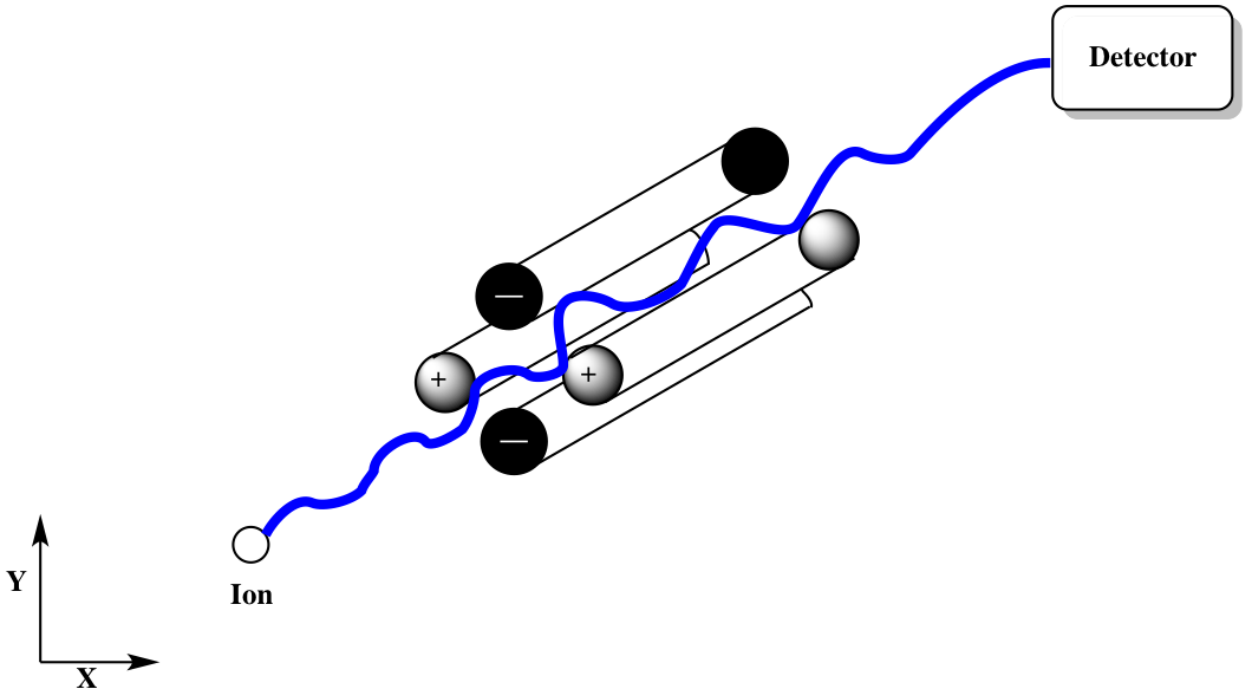
Detector
Ion
Y
X

$$\phi = -(U - V \cos \omega t) \qquad \text{(Equation 1.6)}$$

In the above equations, U is the direct-current (DC) potential applied in the rod, $V \cos \omega t$ represents the alternating-current (AC) potential, V is the amplitude of the radio-frequency (RF) voltage, and ω is the angular frequency of the RF field[106-107]. The total electric field resulting from the applied voltage interferes with the trajectories of the ions travelling through it. By changing the applied DC and AC, only ions whose m/z match the resulting offset voltage survive the trip through the quadrupole and are then observed by the detector[108-109].

The invention of the quadrupole revolutionized the trapping and detecting of ions by MS. Prior to this advancement, mass analyzers were magnet-based. Ions were isolated using a device with a fixed magnetic field and alternating voltage[107]. It is difficulty to generate a stable magnetic field in practice; thus, detecting ions using this approach resulted in complications when the resolution of the instrument resolution was low. Quadrupole design eliminated the use of magnetic fields altogether and replaced them with electric fields. Using these electric fields, ion trajectories are more stable and convenient for detection.

The QqQ mass analyzer, as the name implies, consists of three quadrupoles. In a QqQ, the first and third quadrupoles (Q) operate as analyzers, scanning for ions of selected mass. The second quadrupole (q) functions as a collisional cell and only has RF applied on it. Either an inert or a reactive gas may be used for the collision event inside the second quadrupole to induce fragmentation; this fragmentation occurs by transferring internal energy from the collision gas molecules to the ions or by reactions between ion and gas molecules, respectively[106]. The practical application of QqQ to lipidomics will be discussed in section 1.3: Practical aspects of MS to lipid analysis.

ii. Orbitrap

(a) Principles of orbitrap

The orbitrap analyzer was first introduced in 2000 by Makarov[110]. Its design was adapted from the original Kingdon design in 1923[111], which found a way to trap ions via the principle of electrostatiscity. Since then, the Kingdon trap has been combined with several mass spectrometer set-ups. For example, Knight in 1981 coupled this trap to a Nd:YAG laser source which ionized solid samples[112], and Oksman combined the Kingdon trap with a time-of-flight mass spectrometer[113]. The Kingdon trap, also known as the core of the orbitrap design, is composed of two electrodes: a cylindrical anode and a wire cathode in the centre of the anode. When a DC voltage is applied between the two electrodes, a radial potential is generated that will interfere with the motion of any charged particle travelling through[114]. In the 1981 study done by Knight, the Kingdon trap was modified to also measure the frequency of oscillizations of ions in the confined space (axial movement along the central electrode) of the trap, in addition to the frequency of rotations of the ions (radial/orbital movement around the central electrode). This was very close to the orbitrap model we see today. The overall electrostatic potentials generated in the mass analyzer are described as[110-112, 115-116]:

$$U\,(r,z) = \frac{k}{2}\left(z^2 - \frac{r^2}{2}\right) + \frac{k}{2}\,(R_m)^2\,ln\left[\frac{r}{R_m}\right] + C \qquad \text{(Equation 1.7)}$$

where the first term describes the electrical potential in the symmetrically cylindrical inner space of the orbitrap, and the second term is the logarithmic function of the radial potential between the two electrodes. In this equation, *r* and *z* are the radial coordinates, while *k* is the axial restoring force and strictly depends on the shape of both electrodes and the voltage applied on them. R_m is the spherical radius of the orbitrap, while *C* is a constant. In other words, in the setup of a Kingdon trap or orbitrap, a stable ion is one that orbits around the central electrode and also moves axially

along the z-axis at the same time. The orbitrap mass analyzer that was created by Makarov derived the m/z ratio based on the frequency of the previouly-mentioned axial movement. He argued that, when m/z ratio is determined by the radial oscillation of ions orbitting the electrode, it heavily depends on the initial velocity and radius of orbitting of ions as they are injected into the trap. Consequently, this leads to poor mass resolution. By eliminating this dependence and replacing it with the axial motion of the ions along the electrode, the orbitrap design was created. The most advantageous feature of this design is the ability to derive the m/z of ions with very high resolution and accuracy[110, 116]. The frequency of axial oscillation of the ion is closely associated to its m/z:

$$\omega = \sqrt{\frac{kq}{m}} \qquad \text{(Equation 1.8)}$$

where m and q are mass and charge of the ion, respectively.

As ions oscillate their way through the orbitrap, radially or axially, the resulting currents are recorded, amplified and undergo Fourrier transform to produce the mass spectra.

(b) Ion storage and injection - automatic gain control (AGC)

The orbitrap mass analyzer is commonly preceded by a linear ion trap (LIT). LIT is essentially a quadrupole ion trap, with the addition of electrodes at both ends of the quadrupole to generate trapping fields. Hence ions are effectively trapped by LIT both radially (as in the classic quadrupole) and axially. LIT is known for its high ion storage capacity, and for its ability to eject ions efficiently either via the axial axis of the quadrupole or radially through an ion exit perpendicular to its axis[117]. The orbitrap operates under extremely high vacuum (10^{-10} mbar) and the quadrupoles and/or LIT are usually arranged before the orbitrap to ramp down the pressure and create differential pumping for ion injection into the orbitrap.

The Q-Exactive Plus instrument that is used in this thesis (Chapter 3) contains a quadrupole, and a curved linear ion trap, known as a C-trap, leading to the orbitrap. The C-trap traps ions in

the same manner as the LIT; however, with the curved area inside the trap, ions become more concentrated in this confined space, which allows for injection into the orbitrap as a pack of ions[118-119]. Hence, the C-trap is useful for storing ions and injecting them into the orbitrap. This ion storage is controlled by the development of AGC, which is set up to minimize the accumulation of the space charge effect but could negatively influence mass accuracy[120]. AGC was first invented by Schwartz, Zhou and Bier in 1995 for the Paul ion trap, which was later adapted by others for the orbitrap mass analyzer[121]. The main purpose of AGC is to control the number of ions that enter the ion trap in order to avoid ion saturation, which lead to loss of accurate detection by space-charge effect. In an orbitrap instrument, AGC occurs in the C-trap and controls the number of ions that are injected into the mass analyzer. The role of AGC is important in this thesis because its operation directly affects the construction of images by the AP-MALDI source. This will be explained further in section 1.3.2.iv.

iii. Collision-induced dissociation

Lipidomics studies benefit from applying different MS methodologies to comprehensively profile lipid composition. Chromatography allows for separation of different lipid classes and species; high-resolution mass spectrometer (HR-MS) resolves lipid species with very close monoisotopic masses; and desorption and imaging techniques offer the opportunity to visualize and localize different lipid species at the same time[122]. However, lipids that possess similar elemental component but are structurally different cannot be resolved by HR-MS[123]. In this kind of situation, tandem MS (MS/MS) offers another level of experimentation to fully elucidate the structural make-up of lipid molecules. Conveniently, MS/MS spectra of most lipid classes, such as phospholipids, ceramides and sphingomyelins, yield signature peaks useful for identification of different lipid classes in one matrix[124].

Tandem MS experiment is commonly carried out via the mechanism of collision, known as collision-activated-decomposition (CAD) or collision-induced-dissociation (CID). The general principle of CID operates around the interaction between the ion beam and a stream of collision gas (usually applied perpendicular to the ion beam) in a collision cell[125]. The collision cell is usually a quadrupole, and placed between two mass analyzers as in the case of a triple-quadrupole mass spectrometer. In this kind of instrument, the first quadrupole (Q1) performs precursor ion selection, the second quadrupole is the CID cell, and the third quadrupole (Q3) analyzes all the fragments produced. Tandem MS with a triple-quadrupole mass spectrometer allows for quantification and is very useful in targeted lipidomics (Chapter 1.5.1 and Chapter 2). Due to the introduction of the collision gas, the pressure in the collision cell is significantly higher than the usual pressure inside a regular quadrupole[125].

In an orbitrap mass spectrometer, the orbitrap itself does not have the capability to perform fragmentation. Instead, in such instrument, either the curved trap (C-trap) responsible for ion trapping and injection acts as a collision cell, or an additional RF-only collision cell adjacent to the C-trap performs this task[126]. In both cases, nitrogen gas is used for collision and the method is considered as a higher-energy (high-energy C-trap dissociation, HCD) event than traditional CID. In the orbitrap instrument used in this thesis (Chapter 3), an RF-only octapole acting as a collision cell was attached at the end of the C-trap. Ions that are meant to undergo MS/MS are selected in the quadrupole, passed through the C-trap, and fragmented in HCD cell. The collection of fragment ions is then transferred back to the C-trap and get injected into the orbitrap for m/z detection[120].

The difference between CID in a quadrupole or linear-ion-trap (LIT) and HCD in an orbitrap is the potential used to accelerate the ion beam through the collision cell (collision voltage)[127]. Low-energy CID is usually performed at up to 100 or 200 eV, with the participation of heavier gases such as argon, xenon, krypton or nitrogen as the collision gas to ensure energy transfer

efficiency to ions upon collision. High-energy collision, on the other hand, utilizes helium (He) gas, which is not as effective as the other gases in transferring internal energy but it is sufficient for high-energy processes (up to a few kilovolts in collision energy). In addition, He does not produce excess dissociation reactions and hence is effective in focusing the product ions beam to the mass analyzer. HCD is sometime considered to be harsher[125] than traditional CID and thus has been found to be more compatible in orbitrap instruments.

iv. High-resolution and precise mass measurement

The resolving power of a mass spectrometer is understood as the ability of the instrument to separate two peaks on a mass spectrum that are proximal to each other[128]. Resolving power may be characterized by the distance between two peaks of equal magnitude at a specific fraction (5%, 10% or 50%, for example,) of their height. The resolving power for one single peak is commonly defined by the width of the peak, also at a specific fraction of the peak maximum height. Mass resolution, *R,* describes a mass spectrometer's resolving power, and $\Delta m_{50\%}$ is defined in mathematical terms as the ratio of the mass *m* of a single peak to its full width at 50% of the peak height (Equation 1.9). Accordingly, for two peaks, the resolving power is defined by Equation 1.10[129]. In both cases, the value for *z* is assumed to be 1, as we mainly use singly-charged ions in this thesis:

$$R\left(\frac{m_1}{z}\right) = \frac{m}{\Delta m_{50\%}} \qquad \text{(Equation 1.9)}$$

$$R\left(\frac{m_1}{z} \text{ and } \frac{m_2}{z}\right) = \frac{m_2}{m_2 - m_1} \qquad \text{(Equation 1.10)}$$

When two peaks m_1 *and* m_2 with the same magnitude are resolved, Equation 1.10 is simplified to Equation 1.11:

$$R\left(\frac{m_1}{z} \text{ and } \frac{m_2}{z}\right) = \frac{m_2}{\Delta m_{50\%}} \qquad \text{(Equation 1.11)}$$

This is known as the widely-accepted full-width at half-maximum peak height (FWHM) definition of mass spectrometry resolution[130]. Resolving power relies on the distance between two peaks m_1 and m_2; as this distance gets smaller, the resolving power becomes stronger and the resolution of the instrument is higher (i.e., two very close peaks can be quantifiably separated). Some sources defines mass resolving power as the peak width expressed as a function of mass[131], for example $\Delta m_{50\%}$. To put this into perspective, if signals between m/z 500.1 and m/z 501.1 are to be resolved, the mass spectrometer needs to have resolving power for $\Delta m_{50\%}$ of 1 atomic mass unit (amu), which means the resolution needs to be at least $\frac{m_2}{\Delta m_{50\%}} = \frac{501.1}{1} \approx 500$ to resolve these two peaks

Conversely, if one knows the resolving power of the instrument, the minimum distance between two peaks that allows them to be resolved may be calculated. For example, in this thesis, the orbitrap was operating at resolution of 70 000 in its full scan. Equation 1.11 defines the resolution by the ratio of $\frac{m_2}{\Delta m_{50\%}}$ for this instrument. The reciprocal of the resolution ratio, $\frac{\Delta m_{50\%}}{m_2}$ provides information regarding how far apart two peaks must be in order to be resolved; in other words, it tells us the resolving power of the instrument at that specific mass. Hence, $\frac{\Delta m_{50\%}}{m_2} = \frac{1}{70000}$. As an example, we will pick the peak at m/z 746.5996 to examine. The peak signal that could be resolved from this peak at resolution of 70 000 is:

$$\frac{\Delta m_{50\%}}{m_2} = \frac{\Delta m_{50\%}}{746.5996} \frac{1}{70000}$$

$$\therefore \Delta m_{50\%} = 0.0107$$

Thus, signals need be at least 0.0107 amu far apart from m/z 746.5996 to be resolved. Chapter 3 of this thesis demonstrates the power of high-resolution mass spectrometry when successfully resolving two different lipid species at m/z 746.5696 and m/z 746.5996 ($\Delta m = 0.03$ amu).

It is generally assumed that "low-resolution mass spectrometers" (LRMS) are instruments that are capable of producing ion signals with typical peak-width of 0.6 amu[130] (i.e. $\Delta m_{50\%} = 0.6$). Such broad peaks render these instruments incapable of separating isotopic peaks, especially at higher charge states. This means that one single peak will be present at a particular m/z corresponding to a charge state instead of multiple peaks representing isotopic contribution at that charge state. By the definition of resolution, R = $\frac{m}{\Delta m_{50\%}}$, low-resolution implies an R of less than 10 000, while high-resolution mass spectrometry (HRMS) involves instruments that can produce an R of 10 000 or more.

As high-resolution mass spectrometers can produce R ≥ 10 000, the separation of peaks must come from the ability to measure ion mass at high accuracy[132]. While LRMS gives unit resolution and can separate ions of m/z 731.5 from 731.0 for example, HRMS resolves peaks with similar nominal mass by measuring their exact mass and distinguishing them despite how small the mass difference is. The high accuracy does not only separate and differentiate one molecular ion from another, it also helps to reduce the uncertainty in identifying the detected ion. Mass accuracy and mass resolution are two distinct properties of a mass spectrometer; however they go hand-in-hand with one another. High-resolution produces very sharp molecular peaks on the mass spectrum, allowing separation of one ion from another. This directly leads to better mass accuracy[130]. Resolution of a mass spectrometer depends on how the mass analyzer filters and detects ions[129]. As explained above, the quadrupole applies DC and RF voltages onto the parallel rods that correspond to a specific set of m/z values to select and filter the ions that pass through it. The mass measurement of a quadrupole therefore relies on ion stability within the electric and magnetic field of the quadrupole rods. The orbitrap, on the other hand, does not depend on ion energy and stability[110]. Instead, it measures the axial oscillation frequency of the ion around an electrode, which linearly corresponds only to its m/z (Equation 1.8). The detection duration also directly

affects the resolving power of the orbitrap[133]. A typical experiment performed by the orbitrap may achieve up to about 60 000 resolving power at an m/z of 400 within 750 ms[126]. High-resolving-power mass spectrometers such as the orbitrap allow for accurate measurement and determination of elemental compositions of thousands of molecular ions at the same time. Lower-resolving-power mass spectrometers, such as the triple quadrupole, allow for targeted experiments with high sensitivity in which specific precursor and/or product ions are monitored and profiled.

1.3 PRACTICAL ASPECTS OF MS TO LIPID ANALYSIS

Combining the above technologies and methodologies in concert with innovative experimental design, a multiple-dimensional mass spectrometric approach is born, one which not only enriches the search for novel lipids, but also facilitates identification of lipids and allows for monitoring of changes in the lipidome across different biological states.

1.3.1 Targeted lipidomics

A triple-quadrupole (QqQ) coupled to HPLC-ESI and operating in targeted-lipidomic mode is an efficient way to maximize the sensitivity of chromatography and MS for the detection and quantification of one particular class of lipids[56]. After being separated by HPLC and introduced into the mass spectrometer, a sample containing a mixture of lipid species can be separated into each specific species based on pre-defined precursor-product ion parameters. There are several different scanning modes by the QqQ in this manner; the most common ones are precursor-ion scan (PIS), product-ion scan, and neutral-loss scan[127] (Figure 1.8). PIS is the most popular mode of scanning, and is usually combined with multiple-reaction monitoring (MRM) for lipid

Figure 1. 8. Common types of tandem mass spectrometry analysis by a triple-quadrupole mass spectrometer (QqQ).

(A) Product-ion scan, (B) Precursor-ion scan, (C) Neutral loss scan. In (A), a specific lipid species with known m/z is selected in Q1, fragmented in q (the second quadrupole) by collision-induced-dissociation, and all fragment ions are detected in Q3. (B) is the most popular mode of scanning, in which a lipid complex is introduced into the mass spectrometer and scanned for all masses in Q1. Each species is then fragmented in q and only one particular fragment with known m/z is selected for detection. Any species that produces this fragment is seen in Q3 are thus detected. In (C), again a mixture of lipids is introduced and fragmented and species are then detected when they form a fragment with a pre-defined offset (neutral-loss) from the original mass.

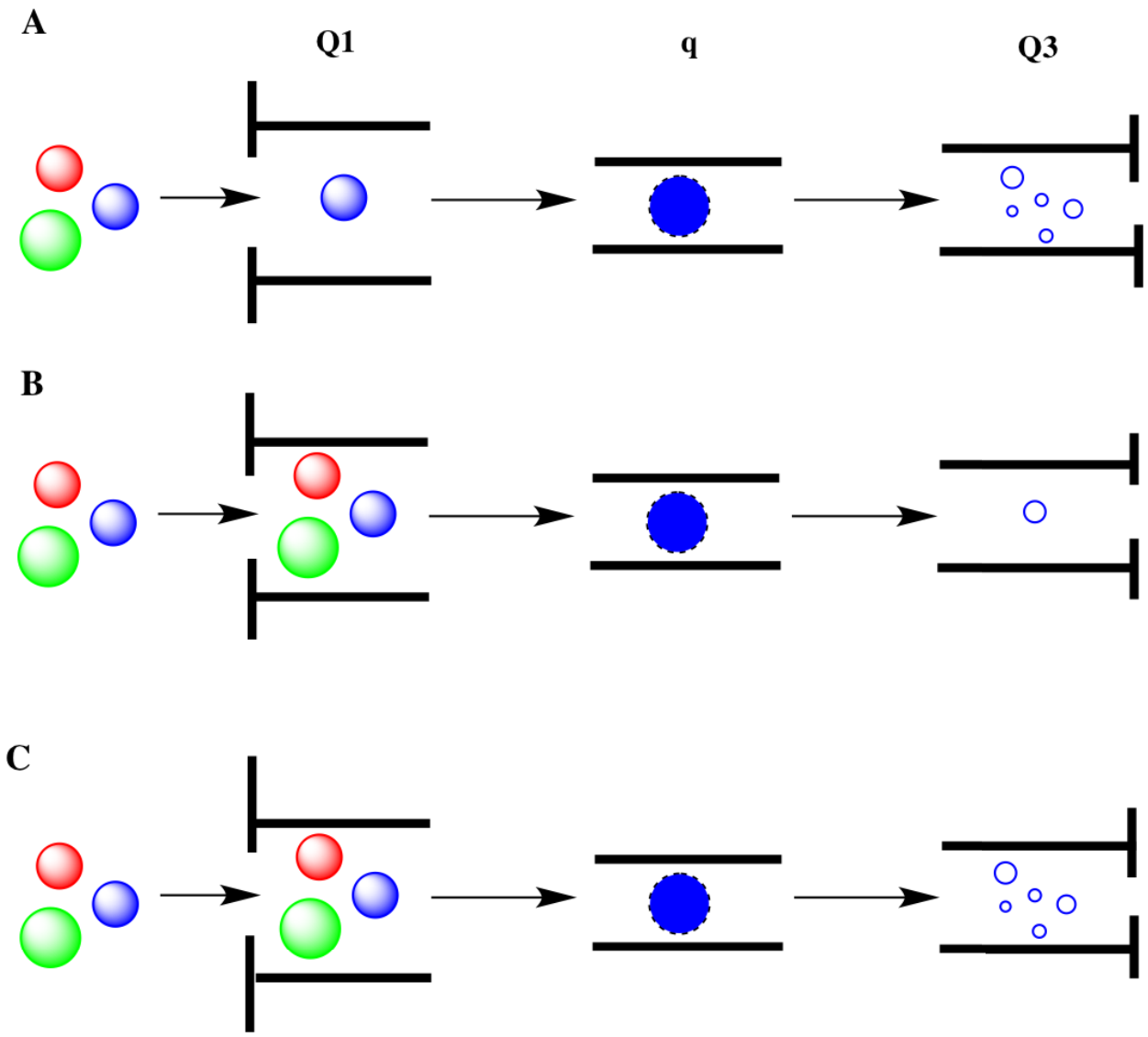
A
Q1
q
Q3
B
C

quantification. PIS first scans for all precursor ions that can produce a specific fragment ion, which is detected in Q3. The m/z of lipid species that produce the target fragment ion are known as transitions and are selected for MRM quantification[134]. In the MRM quantification method, the transition list obtained by PIS is used as the mass window for scanning in Q1. Fragmentation occurs in q2 and the signals of product ion(s) obtained from q2 are used for quantification[135]. MRM relies heavily on strong efficiency of both ionization and fragmentation; hence, optimization of LC, ESI, and collision methods is very important for a reproducible and sensitive MRM experiments. MRM quantification methods have been used extensively in lipidomic research to monitor changes in lipid composition in cells[136], plasma[137] and tissues[138-141] across various diseases and biological states.

1.3.2 Spatial distribution of lipid molecules (MALDI-Imaging mass spectrometry)

MALDI mass spectrometry was first introduced in 1987[53]. However, its application for imaging biological samples was not introduced until ten year later[142]. Figure 1.9 presents a schematic of the MALDI-imaging mass spectrometry (MALDI-IMS) method. At first, MALDI-IMS was mainly used to localize peptides and proteins in different tissues[143-145]. Subsequent developments were also limited to the field of proteomics, in which protein-based biomarkers and their expression were analyzed and imaged to study different diseased states[146-147]. The first imaging lipid analysis study was published in 2007, when Shimma et al[148] localized abnormal distribution of sphingomyelin SM(16:0) in colon cancer.

This section will describe both the principle and applications of the past 10 years of MALDI-IMS in lipidomics as well as important parameters in method development of this technique. The focus will be on the operation of MALDI-IMS with an AP-MALDI source coupled to an orbitrap mass analyzer. This section will also highlight current research and significant contributions in

Figure 1. 9. Schematic of the MALDI-Imaging process.

(A) A sample solution or tissue sample is coated in matrix (either in-solution or by dry method of sublimation). Desorption and ionization occur after sample is irradiated by a pulsed laser beam. Sample ions are then transferred into the mass spectrometer for analysis. (B) Mass spectrum displays detected sample ions and, after image processing, a molecular ion image of the sample is generated, as shown in (C).

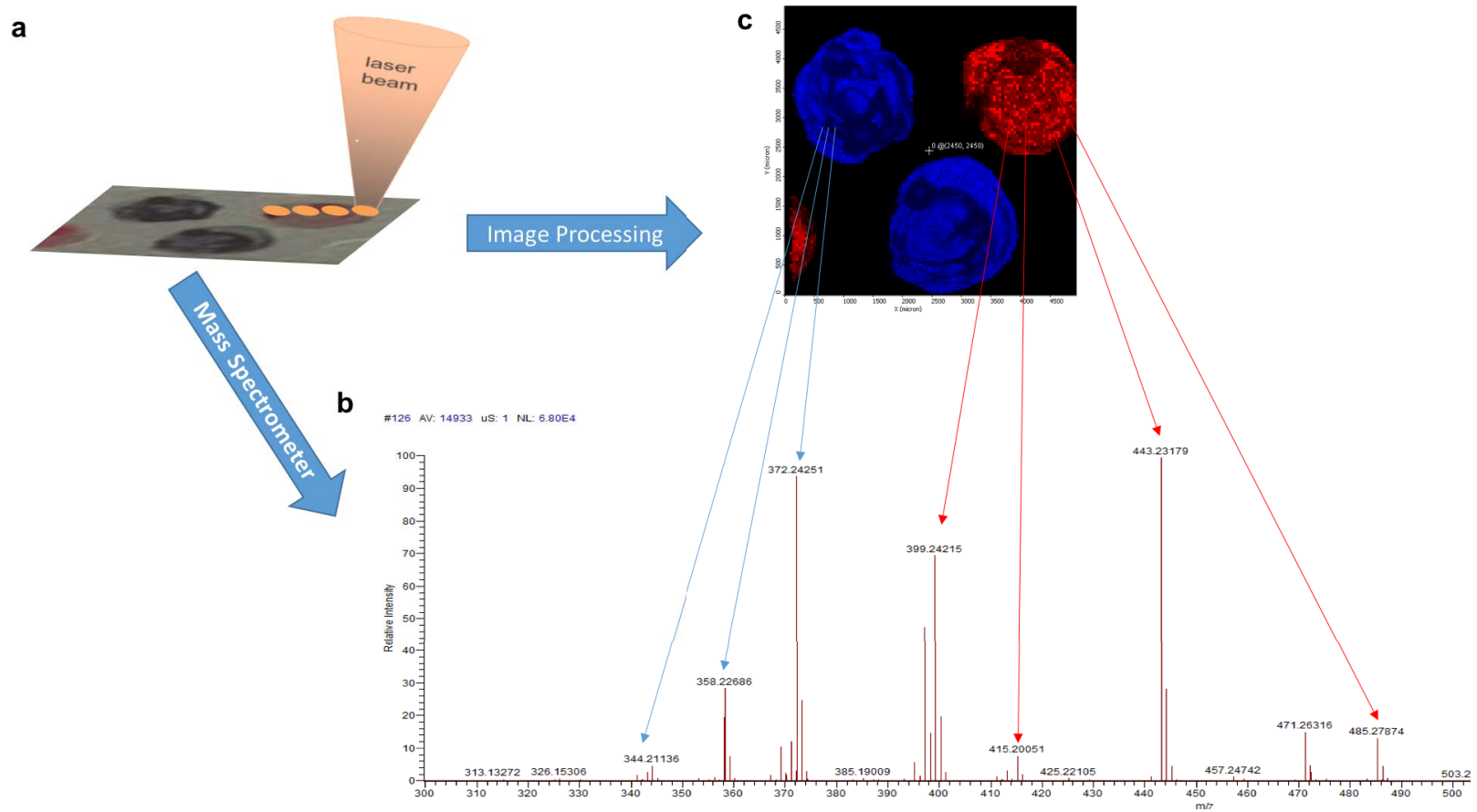
a
laser beam
Image Processing
Mass Spectrometer
c
b
#126 AV: 14933 uS: 1 NL: 6.80E4
Relative Intensity
m/z
313.13272
326.15306
344.21136
358.22686
372.24251
385.19009
399.24215
415.20051
425.22105
443.23179
457.24742
471.26316
485.27874
503.2

this area, while Chapter 3 of this thesis describes a proof-of-principle study of a newly developed method for lipidomic imaging. More specifically, the goal was to develop MALDI-imaging analysis of lipids on mouse brain tissue. The motivation for this aim was based on the powerful and useful application of imaging MS: the ability to combine molecular mass of analytes and their spatial distribution to generate label-free high-resolution biomolecular images.

i. Sample preparation for MALDI-IMS

As with any technique, the sample preparation step is extremely important to ensure tissue integrity, minimize any amounts of modification to endogenous biomolecules, and provide reliable and meaningful biological information. Until recently, flash-frozen tissues were used exclusively in MALDI-IMS[149]. Here, tissue is immediately "snap-frozen" either in liquid nitrogen or CO_2, and thus protected against chemical modifications by oxygen in the air as well as biomolecular delocalization[150]. Another option for preserving tissue is to fix it. Tissue fixation preserves biological structure and morphology, as well prevents enzymatic degradation of proteins. Specifically for MS analysis, flash-frozen tissue is preferred, as para-formaldehyde (formalin)—the most common reagent used in tissue fixation, notably in clinical samples—is known to affect ionization[151].

Although the ideal tissue choice is flash-frozen, it is not the most practical nor feasible option due to sample availability and difficulty with sample handling. Flash-frozen tissues are not always available, especially for clinical specimens. On the other hand, most laboratories and hospitals have tissues and specimens that have been fixed and stored. Fixed samples can be used for multiple histology and immunohistochemistry purposes and are also easy to store; therefore, they are more readily available than flash-frozen tissues. Another advantage of fixed tissue is sample handling; handling of non-fixed tissue is exceedingly difficult and can lead to loss of morphological resolution[152]. During tissue sectioning, both flash-frozen and fixed tissues are usually embedded

in an optimal cutting temperature compound (OCT), a polymer which freezes with the tissue at sectioning temperature (-20^{o}C) and adheres tissue to a cutting "chuck," thus enabling sectioning. However, reports have shown that addition of an OCT strongly suppresses other molecular signals and creates high background during mass spectrometric analysis[145, 149-150]. Several research groups are dedicated to the discovery and investigation of novel embedding materials that are MS compatible, such as cellulose[153], gelatin[154], and other polymers[155] as an alternative to OCT. Thus if fixed tissue is used in an experiment due to practicality and feasibility, extra caution needs to be exercised during tissue preparation to obtain optimal MS results. .

Within the realm of fixed tissues, there are several fixation options. The most popular is formalin-fixed tissue with (FFPE) or without (FF) paraffin-embedment. Formalin fixation involves immersion of tissues in a formalin solution such that amine-containing biomolecules are crosslinked together via formation of methylene bridges[151, 156-157]. In the case of FFPE treatment, the formalin-fixed tissues are dehydrated by alcohol to remove excess formalin and water, and embedded in molten paraffin. The tissue can then be used for sectioning and further analysis[156]. FFPE offers the best preservation for tissue morphology. Although FFPE-treated tissues are easier to handle and section compared to the flash-frozen tissues, there are technical issues associated with FF and FFPE samples. Because proteins and nucleic acids are crosslinked in formalin-fixed tissues, they are difficult to ionize. Some have argued that this crosslinked network prevents ionization and MS detection of other non-crosslinked molecules, such as lipids and carbohydrates[151]. However, recently, Pietrowska *et al* found that there is little difference between spectra collected from FF and flash-frozen tissues by MALDI-IMS for lipid imaging[158]. The case is somewhat different for FFPE, due to the presence of paraffin. Before proceeding to MS analysis, FFPE samples must go through a dewaxing process to remove paraffin[150]. After paraffin removal, samples could be used for protein and peptide analysis and imaging. However, the dewaxing step

involves the use of xylene and alcohol, which removes not only the paraffin wax (which are lipids), but also effectively depletes all endogenous lipids from the tissue. Hence FFPE and deparaffined-FFPE are not a viable choice for lipid imaging. Chapter 3 of this thesis demonstrates that FF tissues are compatible for lipid imaging, but that treatment of brain tissue with xylene efficiently strips the tissue of all lipid content.

ii. Matrix application

There are multiple ways to apply matrix onto tissue samples for MALDI-IMS analysis. All methodologies aim to spread matrix over a large area of the tissue (several millimeters squared), while also ensuring that the matrix layer is uniform in thickness, that it co-crystallizes with the analyte, and, finally, that the crystal size is within a reasonable range such that the spatial resolution of the image is appropriate to the analysis. Traditionally, the matrix is applied onto tissue using an automatic robotic sprayer with a specified spraying speed and flow rate, and it is placed at a set distance from the tissue to ensure uniformity[23, 159]. Alternatively, manual matrix application can also be done using a thin-layer-chromatography (TLC) sprayer or an artistic airbrush. These manual sprayer techniques are ideal for manipulating the spraying process for a specific experimental design. However, they require skillful and experienced handling, and commonly pose technical challenges to the operator[150].

Analyzing lipids using a spraying technique to apply the matrix also poses a problem. Spraying a matrix requires that the matrix be in solution form. Common solvents for matrix preparation are ethanol, methanol and acetonitrile, which are the very solvents used to dissolve and extract lipids. Thus, a legitimate concern is that the application of matrix solution in the "wet" spraying methods may dissolve the lipids and cause migration of lipid molecules on the surface of tissues[123, 160-161]. The introduction of solvent-free matrix application by Hankin[82], the sublimation method, has shown to be comparable to the spraying method in terms of uniformity, and exhibited superiority

over spraying methods in crystal size and enhanced spatial resolutions[87, 162-164]. Sublimation is a physical transition of substance from solid directly to gas phase, without going through the liquid phase. Certain substances possess vapor pressures, which allows the solid form to be vaporized upon heating[165]. After reaching gas phase, these substances can be converted back to the solid phase upon cooling. These sublimation events are incredibly useful for isolating a particular substance from other contaminants, as different substances have characteristic sublimation points. At atmospheric pressure, substances that can sublime often require very high temperatures to do so. The application of a vacuum during the sublimation process will lower this required temperature, as spaces between particles become larger and their intermolecular forces also decrease, shortening the amount of time required to carry out the sublimation process[166]. Sublimation performed at a low pressure of 50 mTorr is used in this thesis for the application of matrix to brain tissue for lipid analysis.

iii. Laser beam, energy and spot size

After matrix deposition, the MALDI plate containing the tissue sample is mounted for the application of laser irradiation. The laser source is positioned on the XY-stage of the MALDI source such that it applies the laser beam onto the MALDI plate indirectly via two lenses and a mirror. The size of the laser beam is controlled by means of the focusing distance from the lenses to the object. The size of the laser beam produces the spot size, which corresponds to the area each laser fire will burn on the sample. Hence, it is important to adjust the spot size according to the desired spatial resolution and step size of the experiment. Another parameter that is also important in the determination of the sample spot size and effectively influences the resolution of the analyte signal is the laser energy. Laser energy settings differ from instrument to instrument. In the AP-MALDI source that is used in this thesis (MassTech Inc.), the maximum energy produced is 8 μJ per laser pulse[167]. The appropriate amount of energy for an experiment is determined by the analyte

signal intensity that is produced. Higher energy corresponds to higher signal intensity; however, it may cause an area of ablation larger than the desired spatial resolution. As a result, the image generated based on this signal intensity could reveal incorrect distribution and position of the analytes.

The laser beam size, energy and sample spot size are especially important in imaging mass spectrometry. In such experiments, the laser beam rasters continuously across the tissue sample and the collected spatial information is used for the generation of an image. The IMS experiment performed in this thesis utilized laser energy in the range of 70-100% of the maximum energy, with adjusted elliptical laser spot size of 70 μm in the horizontal dimension. All experiments were done at a 50 μm spatial resolution. Hence, images were generated by the "oversampling" method[168], in which the distance between two laser spots (or two ablation events) is smaller than the laser spot size. This is another feature that was invented for the adoption of imaging by MALDI-MS: the ability for the XY-stage to move with raster increments that are less than the size of the laser beam. This feature allows for complete ablation and overcomes the limitation posed by laser beam size on resolution. Altogether, these different parameters of the laser source need to be taken into account when performing a MALDI-IMS experiment so that the resulting analyte ions that are introduced into the mass spectrometer can convey the correct message for true images.

iv. Coupling AP-MALDI to orbitrap: role of AGC

As mentioned above, the orbitrap is characteristic for trapping ions by electrostaticity instead of depending on trapping potential based on m/z[110]. This ability increases the instrument's space-charge capacity, leading to its greater sensitivity. However, the very same high space-charge operation also poses the risk for decreased mass accuracy due to accummulation of ion clouds within the trap. AGC is also incredibly useful in the case of an orbitrap coupled to a MALDI source, as its purpose fits perfectly to a non-continous and non-uniform ion source[121]. The nature

of ionization by MALDI source is by pulse, which is triggered by laser shots to produce packets of ions. In the past, MALDI was commonly coupled to a time-of-flight (TOF) mass analyzer because its operational principle requires all ions to fill the flying tube simultaneously[169], which can be achieved easily after one laser pulse. The orbitrap design is compatible with a pulsed source, as ions get injected inside in packets[170]. The presence of AGC makes this injection step more efficient and, at the same time, protects ion saturation to be introduced into the orbitrap. In MALDI-imaging, it is required that every unit (i.e. pixel) of the image is recorded as at least one mass spectrum so that ultimately, an image is generated based on the masses of the analytes. In order to achieve this, the rate of scanning by the mass analyzer needs to be constant. In the case of the orbitrap, the mass analyzer scanning rate relies on injection rate, which in turns depends on ion trapping by the C-trap.

MALDI ion generation depends on many factors including laser beam size, laser energy level, the type of matrix, and the amount of matrix applied (which affects ion supression). Unlike ESI, in which analytes are introduced into the mass spectrometer based on flow rate, MALDI may not be as constant in terms of analyte amount per unit of time or per ionization event; this is due to the use of laser shots to ionize analytes. For this reason, the AGC target in all MALDI imaging experiments needs to be set to lower than desired, from 6E4 to 5E5 ions. Another important parameter is the maximum ion injection time (maximum ion IT), which controls the amount of time allowed for ions to accumulate in the C-trap before being injected into the orbitrap. Scanning events are controlled by either AGC target or maximum ion IT, depending on which parameter is achieved first[120]. Hence, both parameters need to be adjusted to balance each other, taking into consideration the ion influx by MALDI. For example, if the AGC target is set too high, such as 6E6, the maximum ion IT will be inadequately set to 50 ms; this will generate very few ions. After 50 ms, whichever amount of ions being generated will be ejected into the obitrap. Scan rate is

highly dependent on maximum ion IT, reported as scan/second by the instrument. Extremely long scans are not ideal for imaging because the mass analyzer spends too long on the one scan before moving to another, which could result in empty pixels. In full MS scan, AGC and maximum ion IT parameters are not as important; however, these parameters are crucial when imaging is performed concurrently, especially when the imaging source is external to the mass analyzing portion of the MS.

Because the MALDI source is coupled externally to the orbitrap mass spectrometer, communication between the two is extremely critical and manual adjustment of settings is required. On the MALDI source, laser energy and laser beam size determine the ion levels, while movement speed of the plate-holder stage controls position for image generation. Stage speed needs to reflect the current scan rate, set by AGC target and maximum ion IT. All of these parameters require optimization in order to construct a good "bridge" between the AP-MALDI source and the mass spectrometer for reliable imaging experiments.

1.3.3 Role of high-resolution MS in imaging lipids

One of the biggest hurdles in lipidomics is the presence of isobars. Isobars are molecular ions that have the same nominal mass (nominal mass is defined as the integer representing the mass calculated from the most abundant, stable and naturally-occurring isotope of all atoms contributing to that molecule[171]) and thus are unable to be distinguished by low-resolution MS (< 50,000 resolution unit)[11, 172]. Isobars may have different fatty acid components, different types of linkages at the *sn-1* or *sn-2* position, or different double bond positions. For example, PC(16:0/18:1) and PC(20:1/14:0) are isobars with very different fatty acyl chains. Identification of isobars such as this pair is most effectively achieved by an extra level of differentiation additional to their *m/z* given by the mass analyzer; these additional levels of structural elucidation can be accomplished using pre-source chromatography or post-source ion-mobility, time-of-flight separation, or tandem

mass MS[70]. High-resolution MS (HR-MS) alone is not sufficient to separate PC(16:0/18:1) and PC(20:1/14:0) because these two isobars contain similar elemental composition. However, when two lipid species share the same nominal mass but possess completely different elemental compositions, HR-MS can separate the very slight difference in their monoisotopic mass (the exact mass based on the most abundant, stable and naturally-occurring isotope of all atoms in the molecule)[114, 123, 170]. For instance, PC(33:1) and CerP(t42:1) have the same nominal mass of m/z 746, but different monoisotopic masses of m/z 746.5696 and 746.5996 respectively (mass difference is 0.03 Da). A low-resolution mass spectrometer would likely report these values as m/z 746.5 and 746.6, respectively; this lacks accuracy. HR mass spectrometers are able to resolve these two peaks, and the increased mass accuracy in these instruments allows for the identification of each of these isobars. Furthermore, this ability becomes invaluable in MALDI-IMS, where localization information could be tremendously important for understanding disease pathophysiology. During imaging acquisition, several peaks could be present at the same nominal mass; these peaks may be lipid species, other endogenous non-lipid metabolites, or matrix-derived ions[123]. High-resolving power and good mass accuracy allows the correct localization of true lipid ion species. In cases where two completely different lipid species or classes have a very similar nominal mass, HR-MS and good mass accuracy could provide correct distributions of the corresponding molecular ions[150]. The inability to resolve mass peaks properly here could be problematic for lipidomic studies, especially if changes in a particular lipid species or class are ascribed to a disease by the incorrect identification of its presence/absence in tissues of interest. The orbitrap mass analyzer offers high-resolving power, good mass accuracy measurement and sensitivity, and is considerably less expensive compared to the less commonly used Fourier Transform-Ion Cyclotron Resolution (FT-ICR) mass spectrometer, which utilizes an expensive, large cryogenic magnet[173]. Hence, by combining MALDI-IMS and an orbitrap mass analyzer, the

information obtained from imaging experiment is maximized to ensure its reliability for lipidomics studies.

1.4 SCOPE OF THE THESIS

The advances of MS in recent years have revolutionized lipidomics by allowing different approaches to profile, analyze and visualize the membrane lipid compositions, and identify their roles in different biological states. As the field expands, the presence and functional roles of lipids in the cell are receiving more recognition. This thesis in particular focuses on applying two different MS-based lipidomic approaches to analyze lipids in murine brain tissue. The two mass spectrometry techniques used are ESI/MS and MALDI-IMS. The ESI/MS is coupled to LC for efficient separation of different lipid classes and species, after which MRM application is performed to quantify different lipid species within tissue extracts. The MALDI-MS was used to obtain localization information regarding different lipid species.

Specifically, I profile the post-mortem changes in GPC metabolite composition in the murine hippocampus (Chapter 2), while Chapter 3 provides a proof-of-principle project visualizing different lipid species across multiple lipid families. Hence, this thesis is divided into two parts, which aims to answer the following questions:

1) Are there significant changes in the hippocampal lipidome post-mortem? (Chapter Two: **The Death Study: A lipidomic assessment of post-mortem GPC membrane breakdown in murine hippocampus**)

2) What method can be developed to visualize the lipidome in neural tissues? (Chapter Three: **Simultaneous imaging of lipids in murine brain with atmospheric-pressure matrix-assisted laser desorption/ionization coupled to an Orbitrap mass spectrometer**)

CHAPTER 2 - THE DEATH STUDY: A LIPIDOMIC ASSESSMENT OF POST-MORTEM GPC MEMBRANE BREAKDOWN IN MURINE HIPPOCAMPUS

"In showing how a person died, an autopsy often indicates how that person lived." (Yann Martel)

2.1 OBJECTIVE OF THE STUDY

The present study sought to determine whether the GPC lipidome is affected by post-mortem delay in tissue collection.

2.2 AUTHOR CONTRIBUTIONS

Thao Nguyen, Andrew Syrett, and Steffany Bennett conceived and designed the experiments. Thao Nguyen and Andrew Syrett performed all animal manipulations, dissections, and lipid extractions. Thao Nguyen performed all ESI-LC-MS/MS analyses and wrote the paper under the supervision of Drs Hongbin Xu, Maxim Berezovski, and Steffany Bennett.

The Death Study: A lipidomic assessment of post-mortem GPC membrane metabolism in murine hippocampus

Thao T. Nguyen-Tran[1,2], Andrew Syrett[1], Hongbin Xu[1], Maxim Berezovski[2], Steffany A.L. Bennett[1,2]

[1]Neural Regeneration Laboratory, India Taylor Lipidomic Research Platform, Ottawa Institute of System Biology, Brain and Mind Research Institute, Department of Biochemistry, Microbiology, and Immunology, University of Ottawa, Ottawa, Ontario, Canada;

[2]Centre for Catalysis Research and Innovation, Department of Chemistry and Biomolecular Sciences, University of Ottawa, Ottawa, Ontario, Canada

2.3 ABSTRACT

Cerebral lipid abnormalities are commonly assessed post-mortem. Few studies, however, have examined the impact of post-mortem time on quantitative lipidomics. To address this issue, we used LC-ESI-MS to profile glycerophosphocholine metabolite and second messengers in the hippocampus at various time post-mortem in the commonly used mouse strain C57Bl/6 x 129/SV. We report that prolonged post-mortem interval (PMI; time elapsed from death till tissue collection) disrupt GPC metabolism and lead to significant fluctuations in GPC metabolites LPC, LPC(*O*), LPC(*P*) and second messenger PC(*O*) PAF levels. Our results show that clinical brain samples which cannot be collected and preserved immediately after death, may be combined for lipid profiling if they are flash-frozen after 6-12 hours post-mortem. Dramatic changes in GPC metabolites and second messengers occur during early PMI of up to 3-hour and are difficult to control for. Hence tissues collected within this time frame must be handled with care to avoid misinterpretations.

2.4 INTRODUCTION

Post-mortem tissue is required to study molecular changes in human brain associated with neurodegenerative and neuropsychiatric disease. Little, however, is known about how neural membrane composition is altered after death. The advances in LC-ESI-MS and MALDI-IMS described in Chapter One are enabling neural lipid compositions to be defined at the regional and cellular level in brain tissue. While immediately applicable to acute experimental studies, it is not clear how neural membrane metabolism will be affected by post-mortem delay requisite in clinical samples. Without this knowledge, researchers cannot appropriately match post-mortem delay intervals between study groups to ensure changes in lipid composition are, in fact, associated with disease.

The act of dying and the state of death result in dramatic metabolic changes in body tissues. For example, immediately prior to death, agonal anoxia, referring to as acute peri-mortem oxygen depletion as respiration becomes increasing impaired, has significant impact on RNA integrity[174]. Immediately after death, circulating oxygen level terminally deplete, causing the body to enter anoxia[175]. At the cellular level, oxygen deprivation triggers cellular acidification, increases production of reactive oxygen species, and elicits cell swelling (edema) as a result of intracellular accumulation of Na^+, inorganic phosphates, and metabolites. Once osmolarity is compromised, membrane integrity is compromised[176]. Few studies, however, have examined effect of non-enzymatic autolysis on neural lipid composition. Furthermore, previous studies suggest that under conditions of oxygen shortage, phospholipases are activated leading to an accelerated degradation of membrane phospholipids post-mortem[177-179]. As reviewed in Chapter One, GPCs are both enzymatically remodelled via the Land's cycle and non-enzymatically remodelled via oxidation. When neural membrane integrity is lost, such as in the case of death, GPCs in the membrane are expected to decrease dramatically as PLA_2 activity increases as has been shown *ex-vivo* in anoxic

cardiac tissue[179] and *in vivo* post-mortem in muscle tissue[176]. These studies predict that LPC, LPC(O), and LPC(P) concentrations will increase post-mortem. As these lipid subclasses are also inflammatory signalling molecules, changes in abundance due to death could be interpreted as a disease-associated inflammatory state if PMI is not considered.

Here, I assessed post-mortem changes in GPC metabolism in the murine hippocampus. In the present study, the overall GPC metabolite and second-messenger profile including LPCs, LPC(O)s or *lyso*-PAFs, PC(O)s limited to species with acetyl *sn-2* chains remodelled from LPC(O) are also known and will be referred to as PAFs, and LPC(*P*)s were profiled in murine hippocampi at 0, 1, 3, 6, 12 hours post-mortem. To date, no other study has utilized the same methodology for a similar purpose. Furthermore, the results of this study may raise concerns in past, present, and future studies involving sacrificed mice tissues regarding sample integrity due to drastic changes in the tissues' lipidome following death.

2.5 MATERIALS & METHODS

2.5.1. Animals

Six-month-old male N3 and N4 C57BL/6 x 129/SV mice were sacrificed by lethal injection with 0.15 mL euthanyl (#1EUS001, Bimeda-MTC Animal Health Ins., ON, Canada at concentration of 65 mg/ml), followed by decapitation. This mixed hybrid strain and number of back-crosses to a C57BL/6 lineage represents a commonly used genetic background in transgenic mouse models of human disease[180]. Hippocampi were dissected immediately, resulting in a 0.4-0.5 h (25-30 min) PMI. To approximate human PMI, mice were maintained for 1, 3, 6, or 12 hours after injection at room temperature before removal of hippocampi. All tissues were weighed, tissue wet weight recorded, and flash-frozen by immersion in liquid nitrogen. Tissues were stored in -80^{o}C until extraction. All of these steps were carried out according to the strict ethical regulations

and guidelines for animal experimentation of the Canadian Council on Animal Care and were approved by the University of Ottawa Animal Care Committee.

2.5.2. Phospholipid Extraction

Hippocampi were extracted using our modified Bligh and Dyer method[12]. Exogenous standards PC(13:0/0:0) (187.5 ng, #855476, Avanti Polar Lipids, Alabaster, Alabama) and PC(12:0/13:0) (500 ng, #LM-1300, Avanti Polar Lipids), PS(12:0/13:0) (200 ng Avanti Polar Lipids, LM-1100), and PE(12:0/13:0) (500 ng Avanti Polar Lipids, LM-1000) were added at time of extraction in 4 mL of acidified methanol (2% v/v acetic acid in methanol) (#351271-212 and #A412P-4 respectively, Fisher Scientific, Ottawa, Ontario). Subsequently, 3.2 mL of 0.1 M sodium acetate (#SAA304, Bioshop, Burlington, Ontario) and 3.8 mL of chloroform (#C298-4, Fisher Chemical, Fair Lawn, New Jersey) were added into the homogenate to generate aqueous-organic phase partition. The lipid-containing organic layer was collected, and back extraction was repeated three times by adding 2 mL of chloroform onto the aqueous phase. Finally, the collected chloroform phases were dried under nitrogen gas. Dried lipids were dissolved in 300 μL of 100% MS-grade ethanol (#P016EAAN, Commercial Alcohols) and stored in amber vials (BioLynx C779100AW) under nitrogen gas, at -80^{o}C.

2.5.3. LC-ESI-MS/MS

LC-ESI-MS/MS was performed on an Agilent 1100 system (Agilent Technologies, Santa Clara, California) coupled to a QTRAP5500 mass spectrometry (AB Sciex, Concord, Ontario). Chromatography column was made from capillary (Polymicro Technologies, Phoenix, AZ, USA) composed of fused silica with inner diameter of 250.6 μm were cut to a length of 15 cm. Frit was made on one end of the capillary by dipping the cut capillary into a solution composed of 3:1 Kasil 1624 potassium silicate (PQ Corporation, Malvern, PA, USA) and formamide (OmniPur, Millipore Sigma, 4610-OP, Etobicoke, ON, Canada). Fritted capillaries were placed in an oven,

heated at 100°C for 24 hours. Afterwards, they were cut to 12 cm and packed with 10 cm of ReproSil-Pur C_{18} size 3 μm stationary phase in acetone using a nitrogen pressure injection cell.

In the LC procedure, a gradient elution was used with a mobile phase A (solvent A) (0.1% formic acid (Sigma-Aldrich, 56302, St. Louis, Missouri) and 10 mM ammonium acetate (NH_4AC) EMD Millipore, 2145-OP, Etobicoke, Ontario) in MS-grade water (J.T. Baker, Avantor, 9831-03 Center Valley, Pennsylvania)) and mobile phase B (solvent B) (0.1% formic acid, 10mM NH_4AC in 5:2 acetonitrile (ACN, J.T. Baker, Avantor, 9839-03) to isopropanol (IPA, Fisher Scientific, A416-4). A solution containing the following was loaded onto an Agilent 96-well sampling plate: 5 μL of the extracted lipid sample, 2.5 μL of Splash™ standards (0.5 ng/μL of each LPC(18:1-d7/0:0) (#791643, Avanti Polar Lipids), LPE(18:1-d7/0:0) (#791644, Avanti Polar Lipids), PC(15:0/18:1-d7) (#791637, Avanti Polar Lipids), PE(15:0/18:1-d7) (#791638, Avanti Polar Lipids), PC (P-16:0/0:0) (#852464, Avanti Polar Lipids)), 2.5 μL of deuterated lipid standards (2.5 ng of d4 PC(O-16:0/0:0 (*lyso*-PAF C-16-d_4, #360906, Cayman Chemical Company, Ann Arbor, Michigan), 1.25 ng of d4 PC(O-16:0/2:0) (PAF C-16-d4, #360900, Cayman Chemical Company, Ann Arbor, Michigan), 2.5 ng of d4 PC(O-18:0/0:0) (*lyso*-PAF C-18-d4, #10010228, Cayman Chemical Company, Ann Arbor, Michigan), 1.25 ng of d4 PC(O-18:0/2:0) (PAF-C18-d4, #10010229, Cayman Chemical Company, Ann Arbor, Michigan), 13.5 μL of solvent A. The sample plate was then covered and placed in the auto-sampler that was set at 4°C. Injection volume from the plate was 3 μL. Each run containing the separating and mass analyzing steps of lipids was 60 minutes in length, and the mobile phase's gradient was as followed: 30% solvent B from 0 to 5 minutes, 100% solvent B from 5 to 45 minutes and 30% from 46 to 60 minutes. After each lipid sample was a blank run, composed of only solvent A using the same gradient protocol as with the lipid sample.

After separation, analytes entered the mass spectrometer via electrospray ionization (spray voltage at 4.5 kV and curtain gas was at 20 V), which was operating in positive ion mode and scanning of mass range at m/z 450-650 (GPC range). The ionized analytes were sent through the three quadrupoles where the GPC species were detected by multiple reaction monitoring (MRM). The $[M+H]^+$ precursor ions were selected in the first quadrupole (Q1), collided with nitrogen gas in the second quadrupole (Q2) with a collision energy of 47 eV, and the product ions were detected in the third quadrupole (Q3) at m/z 184.1 – the diagnostic fragment of PC and sphingomyelin. Because sphingomyelins also fragment with a diagnostic m/z 184.1 ion, Dr Hongbin Xu, in our laboratory, used differential ion mobility as an orthogonal separation to LC to confirm that none of the species detected in this study were sphingomyelins. Differential ion mobility separates molecules at the interface between the source and orifice based on the difference in their structures[181]. The confirmatory data of separating GPC from SM are not presented in this thesis as the analysis was not done by TN.

GPC quantification was performed on Multiquant (MQ) software (version 3.0.2, AB Sciex). All programmed mass transitions containing the product ion of m/z 184.1 were analyzed and their peak areas were integrated. Spectra were aligned using RT-STAR (v1.0), an in-house algorithm that standardizes retention times to align lipid species across lipidome. Molecular identities were assigned using VaLID v3.0[182] and the LIPID MAPS Structural Database[183]. Raw peak areas were corrected for extraction efficiency and instrument response by normalization to the internal standard PC(12:0/13:0), added at time of extraction. Lipid abundances were expressed as pmol equivalent of PC(12:0/13:0) per mg of tissue wet weight ($pmol/mg_{tissue}$) or as $\log_2$ fold change of these abundances relative to control.

2.5.4. Statistical Analysis

Multivariate partial least square discriminant analysis (PLS-DA) was performed using MetaboAnalyst 3.0[184-188]. Average linkage hierarchical clustering using city-block similarity metrics (autoscaled pmol equivalents per mg tissue wet weight) were performed using Cluster 3.0 software[189], visualized using Java TreeView v1.1.6 software[190]. GPC abundances were compared using univariate one-way analysis of variance (ANOVA) with alpha set to 0.05. We then controlled for multiple comparisons by setting the false detection rate (FDR) to Q=0.05 according to the method of Benjamin, Kreiger, and Yekutieli[191]. We controlled for between-group multiple comparisons for GPC differences that met these criteria using *post-hoc* Tukey's tests with familye-wise corrected alpha set to p=0.05. All values are presented as mean ± SEM (n = 3-5 animals per group).

2.6 RESULTS

2.6.1. There were 46 GPC metabolite and second messenger species detected in the hippocampus, 16 of which showed significant changes in their composition to overall GPC content.

A total of 46 GPC metabolites belonging to four GPC sub-classes were identified: 17 LPCs, 21 PC(*O*), 5 LPC(*O*)s, 3 LPC(*P*) (Figure 2.1). All PC(*O*) that were identified and profiled contain an acetyl group at the *sn-2* position, making them 1-alkyl-2-acetyl-*sn*-glycero-3-phosphocholine, or PAF. Composition (mol%) was calculated for each sample. We compared control (tissue dissected and flash-frozen within 0.4 h of lethal injection) to tissue harvested after a 12-hour PMI.

Figure 2. 1. GPC metabolite composition is different in murine hippocampal dissected and flash-frozen at time of death compared to tissue harvested at 12-hour post-mortem.

Mol% distribution of the 46 GPC metabolites and second messengers detected in murine hippocampus, where mol% of 17 LPC species showed in A), of 5 LPC(P) species showed in B), of 21 PAF species showed in C) and of 3 LPC(P) species showed in D). Statistically significant assessed by multiple Student's t-test followed by FDR with Q=0.05 are indicated. * indicates $p < 0.05$; ** indicates $p < 0.01$ and *** indicates $p < 0.0001$.

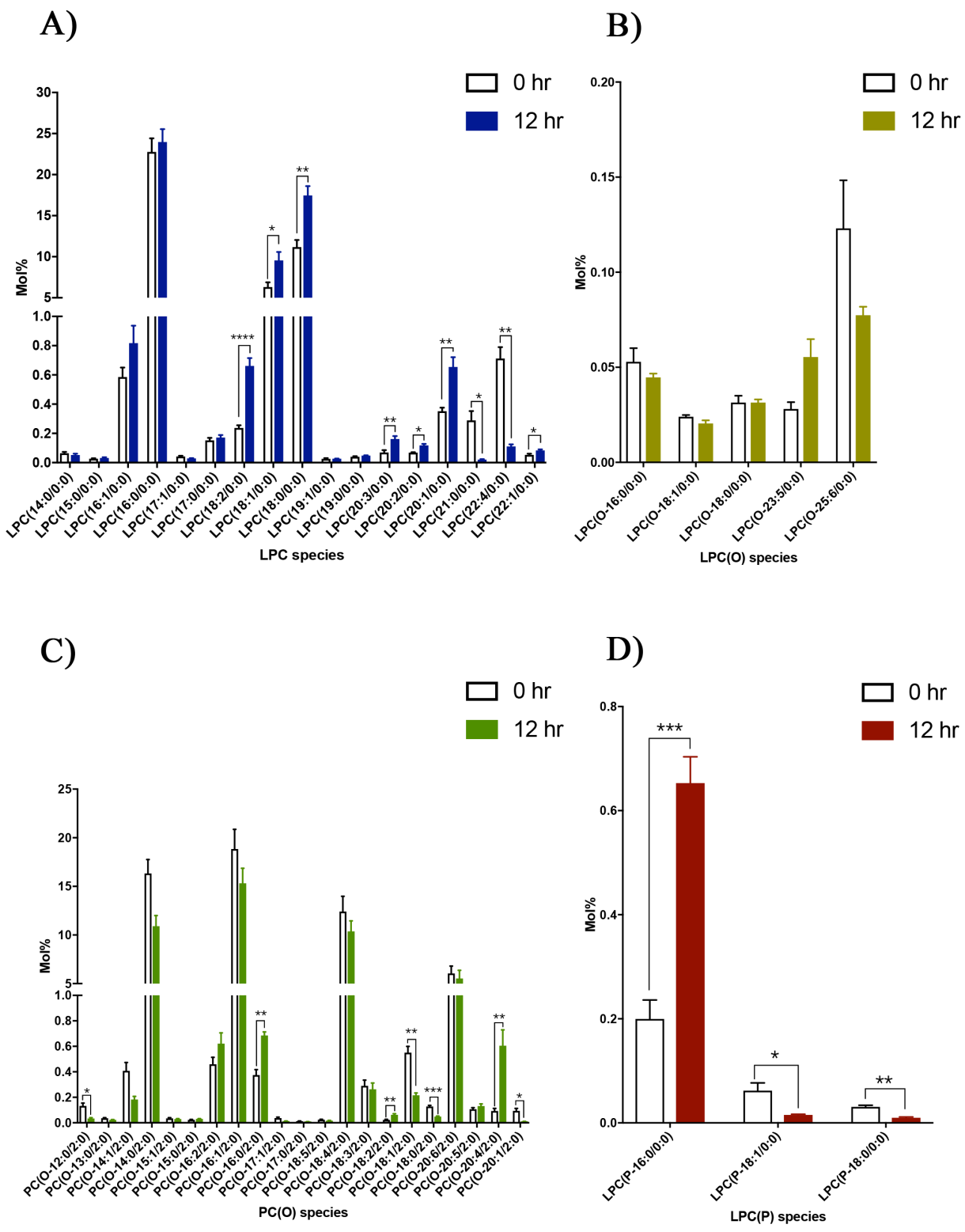
A)
0 hr
12 hr
Mol%
LPC species
LPC(14:0/0:0)
LPC(15:0/0:0)
LPC(16:1/0:0)
LPC(16:0/0:0)
LPC(17:1/0:0)
LPC(17:0/0:0)
LPC(18:2/0:0)
LPC(18:1/0:0)
LPC(18:0/0:0)
LPC(19:1/0:0)
LPC(19:0/0:0)
LPC(20:3/0:0)
LPC(20:2/0:0)
LPC(20:1/0:0)
LPC(21:0/0:0)
LPC(22:4/0:0)
LPC(22:1/0:0)
B)
0 hr
12 hr
Mol%
LPC(O) species
LPC(O-16:0/0:0)
LPC(O-18:1/0:0)
LPC(O-18:0/0:0)
LPC(O-23:5/0:0)
LPC(O-25:6/0:0)
C)
0 hr
12 hr
Mol%
PC(O) species
D)
0 hr
12 hr
Mol%
LPC(P) species
LPC(P-16:0/0:0)
LPC(P-18:1/0:0)
LPC(P-18:0/0:0)

A significant increase in lipid abundance of the majority of LPC species (7 out of 17 species) was observed with post-mortem delay (figure 2.1A). Decreases in the mol% composition of 2 LPC species were also detected (Figure 2.1A). No statistically significant change was seen in mol% composition of LPC(*O*) (Figure 2.1B). Alterations, both increases and decreases, were evident in the downstream 7 PAF metabolite species within 12 h of death (Figure 2.1C). Meanwhile, out of 3 detected LPC(*P*) species, only mol% of LPC(*P*-16:0/0:0) increased significantly whereas LPC(*P*-18:1/0:0) and LPC(*P*-18:0/0:0) decreased significantly. These data clearly demonstrated that GPC metabolite and second messenger composition was affected by post-mortem delay.

2.6.2. GPC metabolite and second messenger compositional change in different PMI

We examined kinetics in more detail comparing the overall changes of all four detected GPC metabolites and second messenger sub-families over time (Figure 2.2). At 0-hour (control group), 21 species of PAF made up the majority of the detected GPC metabolite and second messenger species, 56.5 %. The 17 species of LPC made up 42.9 % of the total detected GPC content; LPC(*O*) makes up of 0.26 % and LPC(*P*) contributed 0.29 %. These compositions changed over post-mortem times. A rapid enrichment in LPC metabolites and decrease in PAF second messengers were observed within the first post-mortem hour, followed by gradual decrease in the LPC content and increase in the PAF content up to 6-hour post-mortem. By 12-hour post-mortem, hippocampal LPC content increased by 11% while PAF content decreased by similar amount. The LPC(*O*) content in the hippocampus appeared to have no change at this time point while LPC(*P*) showed a significant change of about 3-fold compared to the control (Figure 2.2).

Figure 2. 2. GPC composition fluctuates with post-mortem time interval.

Subclass composition (mol%) and molecular identities are presented. The composition of GPC metabolite and second messengers is presented by the mol% of the four-detected lipid sub-families. LPC and PC(O) PAF contribute to the majority of GPC composition and the fluctuation in their abundance is observed overtime. Notably, although only contributing a small portion to the total detected GPC content, LPC(P) mol% increased almost 3-folds by 12-hour post-mortem compared to the control (0-hour).

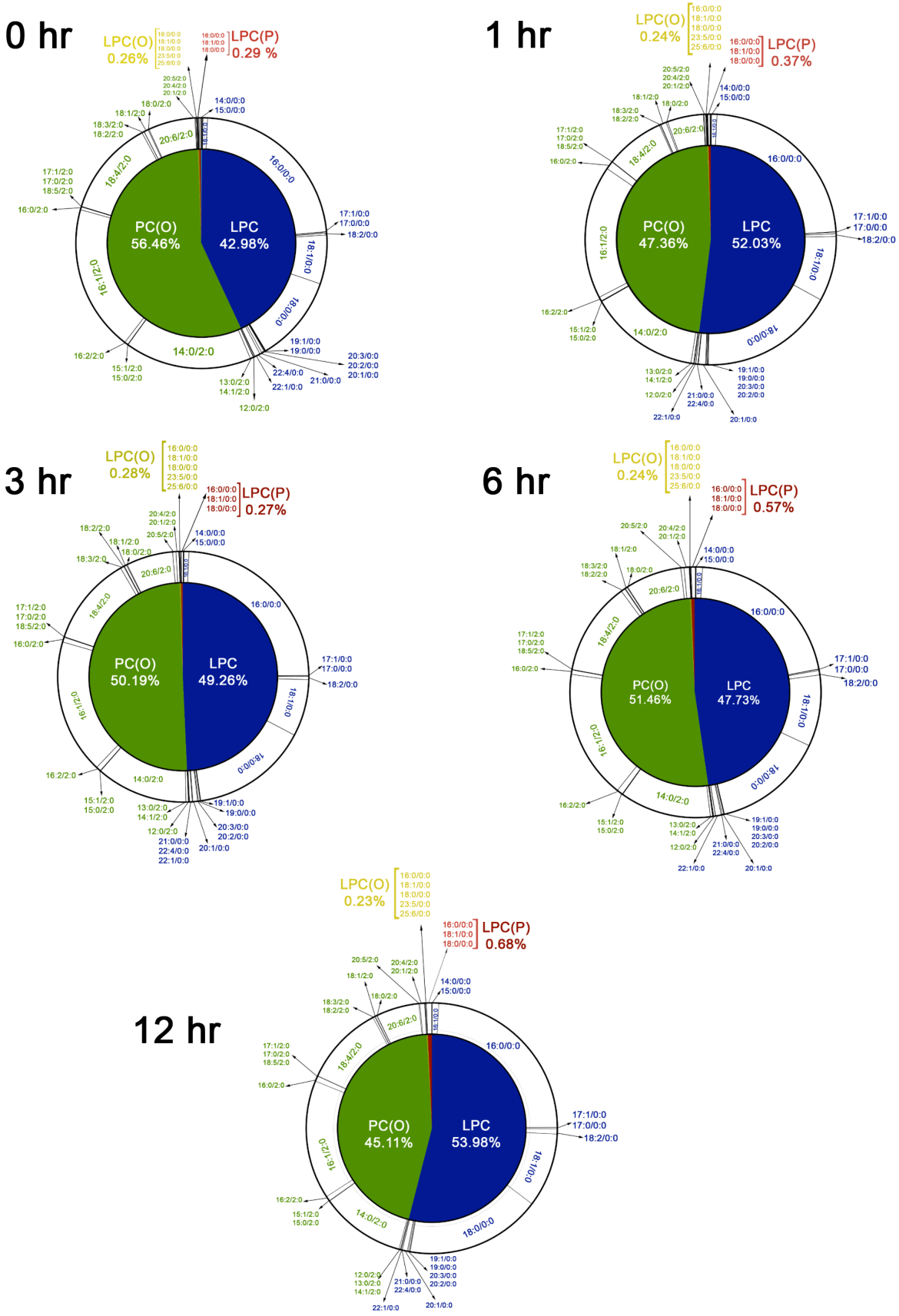
0 hr
LPC(O)
0.26%
16:0/0:0
18:1/0:0
18:0/0:0
23:5/0:0
25:6/0:0
LPC(P)
0.29 %
16:0/0:0
18:1/0:0
18:0/0:0
PC(O)
56.46%
LPC
42.98%
1 hr
LPC(O)
0.24%
LPC(P)
0.37%
PC(O)
47.36%
LPC
52.03%
3 hr
LPC(O)
0.28%
LPC(P)
0.27%
PC(O)
50.19%
LPC
49.26%
6 hr
LPC(O)
0.24%
LPC(P)
0.57%
PC(O)
51.46%
LPC
47.73%
12 hr
LPC(O)
0.23%
LPC(P)
0.68%
PC(O)
45.11%
LPC
53.98%
16:0/0:0
18:1/0:0
18:0/0:0
20:5/2:0
20:4/2:0
20:1/2:0
14:0/0:0
15:0/0:0
18:0/2:0
18:1/2:0
18:3/2:0
18:2/2:0
20:6/2:0
18:4/2:0
17:1/2:0
17:0/2:0
18:5/2:0
16:0/2:0
16:1/2:0
16:2/2:0
15:1/2:0
15:0/2:0
14:0/2:0
13:0/2:0
14:1/2:0
12:0/2:0
21:0/0:0
22:4/0:0
22:1/0:0
19:1/0:0
19:0/0:0
20:3/0:0
20:2/0:0
20:1/0:0
18:0/0:0
18:1/0:0
17:1/0:0
17:0/0:0
18:2/0:0

2.6.3. Compared to the control, 24 GPC metabolite and second messenger species were found to fluctuate significantly during the progression of post-mortem delay

To identify the species-specific changes that altered total GPC composition in the hippocampus at 1, 3, 6, 12-hour post-mortem, changes in abundance at the molecular level were assessed using univariate one-way ANOVA and compared to the control at 0-hour post-mortem by Dunnett's post-hoc (Figure 2.3). Twenty-four GPC metabolite and second messenger species whose abundances showed statistical significance ($p < 0.05$) over post-mortem time were identified and assessed using partial least square-discriminant analysis (PLS-DA) to identify metabolic patterns. PLS-DA is used to identify latent variables (i.e., the principal components) that discriminate between conditions in high-dimensional data. Using the first two components, shown in Figure 2.4A, the two-dimensional score plots of PLS-DA revealed that the statistically significant GPC species in the control group were clearly separated from those at 1-hour post-mortem, and from those at 3, 6, 12-hour post-mortem. Notably, GPC species at 1-hour post-mortem were clearly separated from the rest of PMIs, whereas 3, 6, and 12-hour post-mortem were not. This suggests a component of GPC metabolism disruption that was unique to 1-hour PMI. Figure 2.4B revealed the top 20 GPC metabolite and second messenger species whose variable importance plot (VIP) values were higher than 0.6. These are the ones whose contribute the most to the entire PLS-DA model by separating different PMIs.

2.6.4. The GPC lipidome is altered dramatically within the first hour post-mortem and more gradually three to twelve hours post-mortem

Hierarchical cluster analysis was performed on all GPC species and each sub-family was clustered separately. Figure 2.5 displays a heat-map showing each GPC family clustered based on similar changes in lipid abundance at each PMI compared to the control. It was revealed that there

Figure 2. 3. Post-mortem delay affected individual GPC second messenger and metabolite species in the hippocampus.

All GPC species belonging to LPC, PAF, LPC(O) and LPC(P) sub-families shown in A), B), C) and D) respectively. The pmol per mg tissue wet weight for each lipid species was analyzed using one-way ANOVA (p-value < 0.05), an FDR (Q = 0.05) and a Dunnett's post-hoc where every species at each post-mortem interval was compared to the control group (0-hour). Data are represented as mean ± SEM. * indicates $p < 0.05$; ** indicates $p < 0.01$ and *** indicates $p < 0.0001$.

A)

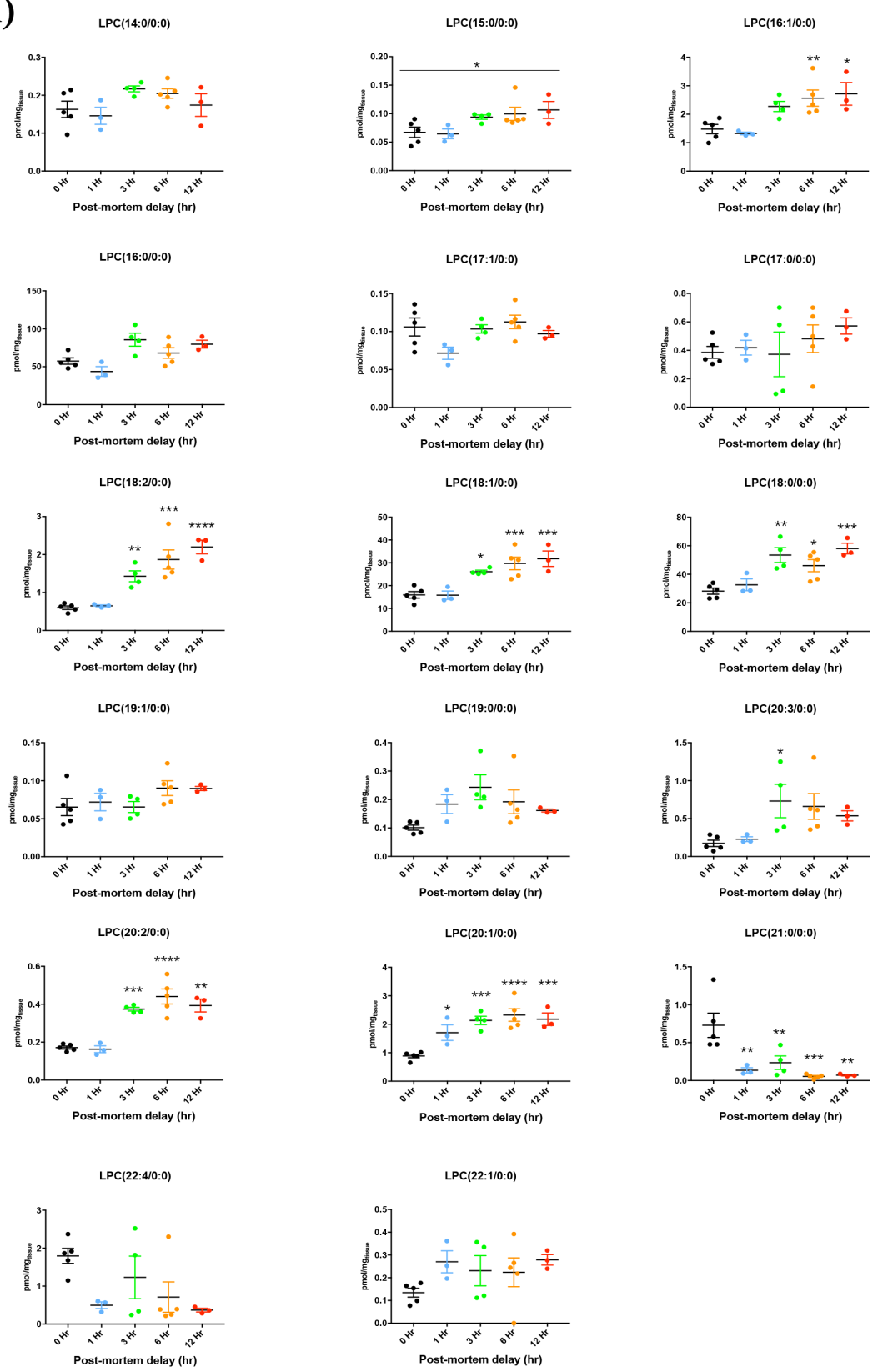
LPC(14:0/0:0)
LPC(15:0/0:0)
LPC(16:1/0:0)
LPC(16:0/0:0)
LPC(17:1/0:0)
LPC(17:0/0:0)
LPC(18:2/0:0)
LPC(18:1/0:0)
LPC(18:0/0:0)
LPC(19:1/0:0)
LPC(19:0/0:0)
LPC(20:3/0:0)
LPC(20:2/0:0)
LPC(20:1/0:0)
LPC(21:0/0:0)
LPC(22:4/0:0)
LPC(22:1/0:0)
pmol/mg tissue
0 Hr
1 Hr
3 Hr
6 Hr
12 Hr
Post-mortem delay (hr)

B)

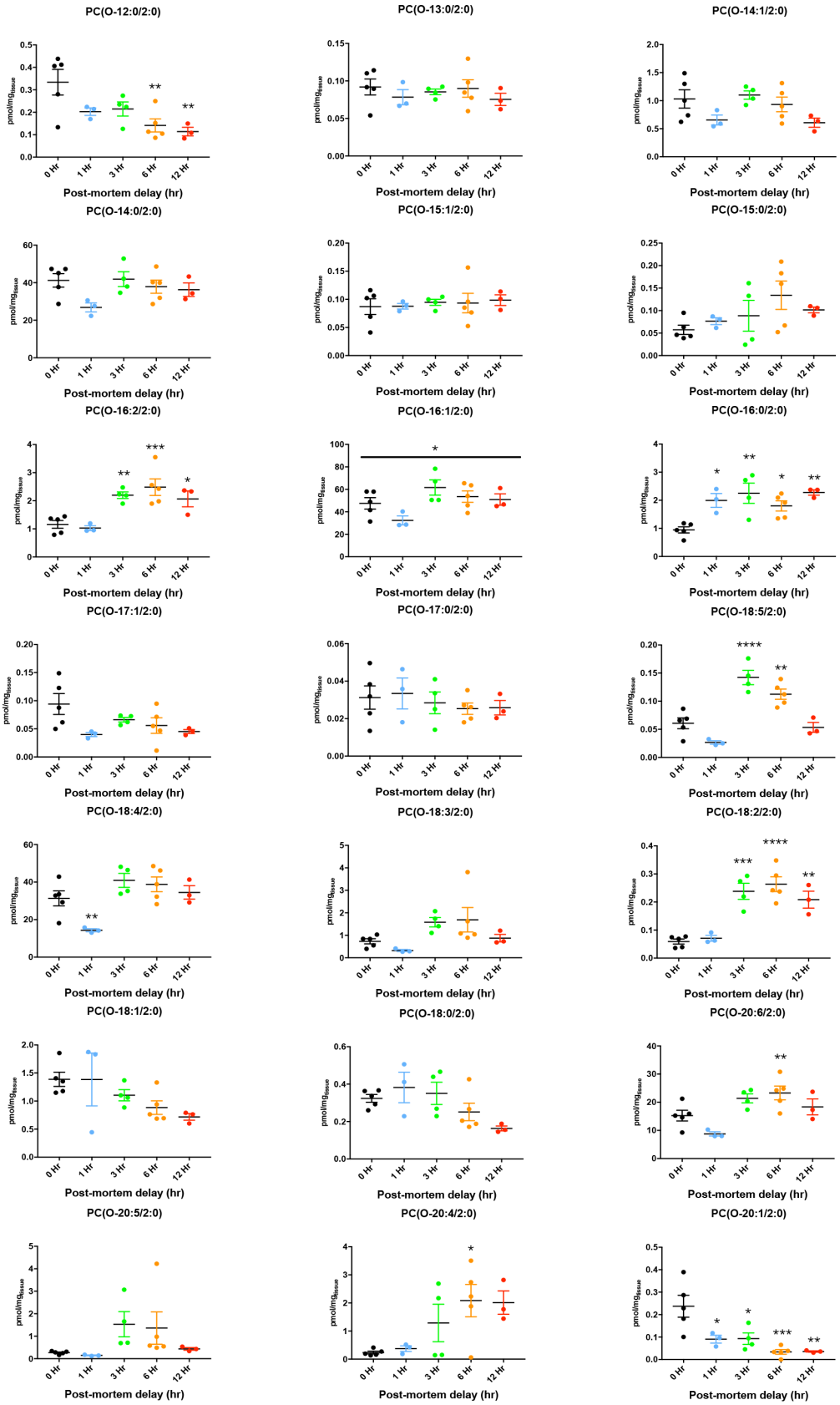
PC(O-12:0/2:0)
PC(O-13:0/2:0)
PC(O-14:1/2:0)
PC(O-14:0/2:0)
PC(O-15:1/2:0)
PC(O-15:0/2:0)
PC(O-16:2/2:0)
PC(O-16:1/2:0)
PC(O-16:0/2:0)
PC(O-17:1/2:0)
PC(O-17:0/2:0)
PC(O-18:5/2:0)
PC(O-18:4/2:0)
PC(O-18:3/2:0)
PC(O-18:2/2:0)
PC(O-18:1/2:0)
PC(O-18:0/2:0)
PC(O-20:6/2:0)
PC(O-20:5/2:0)
PC(O-20:4/2:0)
PC(O-20:1/2:0)
pmol/mg tissue
0 Hr
1 Hr
3 Hr
6 Hr
12 Hr
Post-mortem delay (hr)

C)

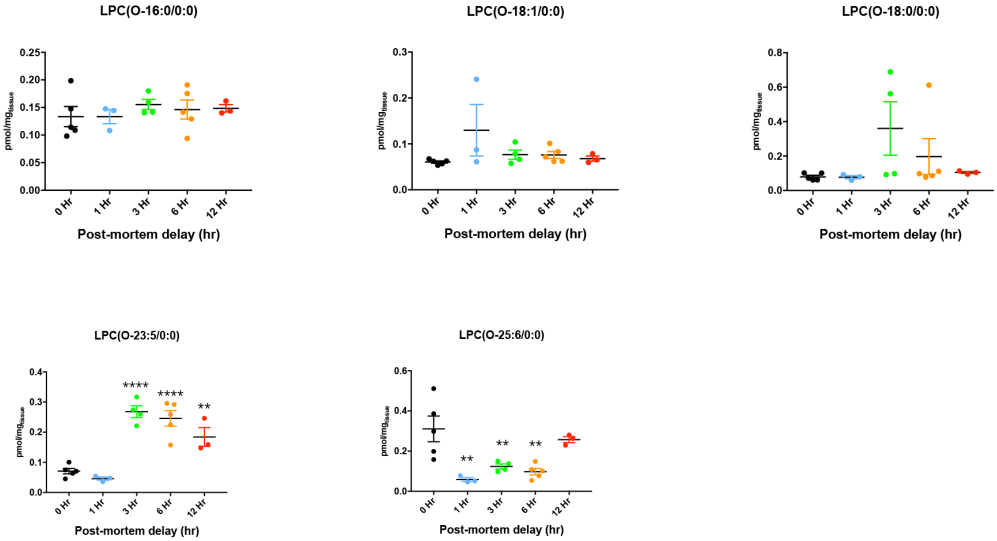
LPC(O-16:0/0:0)
LPC(O-18:1/0:0)
LPC(O-18:0/0:0)
LPC(O-23:5/0:0)
LPC(O-25:6/0:0)
pmol/mg tissue
0 Hr
1 Hr
3 Hr
6 Hr
12 Hr
Post-mortem delay (hr)

D)

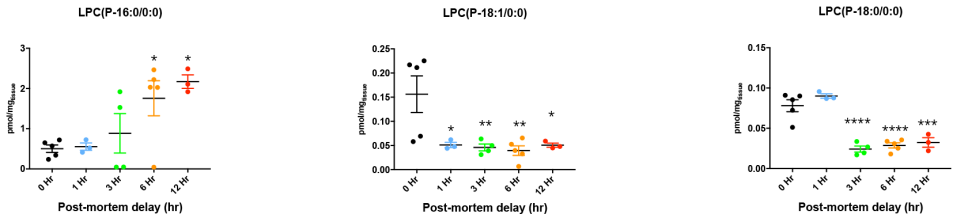
LPC(P-16:0/0:0)
LPC(P-18:1/0:0)
LPC(P-18:0/0:0)
pmol/mg tissue
0 Hr
1 Hr
3 Hr
6 Hr
12 Hr
Post-mortem delay (hr)

Figure 2. 4. PLS-DA score plot of GPC metabolites and second messengers detected in hippocampal tissues at 0, 1, 3, 6, and 12-hour post-mortem.

A) PLS-DA analysis of 25 statistically significant GPC metabolite and second messenger species ($p < 0.05$) at different post-mortem interval clearly showed separations of all time groups from the control. **B)** Significantly changed abundances of top 15 GPC metabolite and second messenger species with the VIP value of > 0.6 which contributed to the distinct segregation of 1-hour and 3, 6, 12-hour post-mortem (as a group) from the control (0-hour post-mortem).

A)

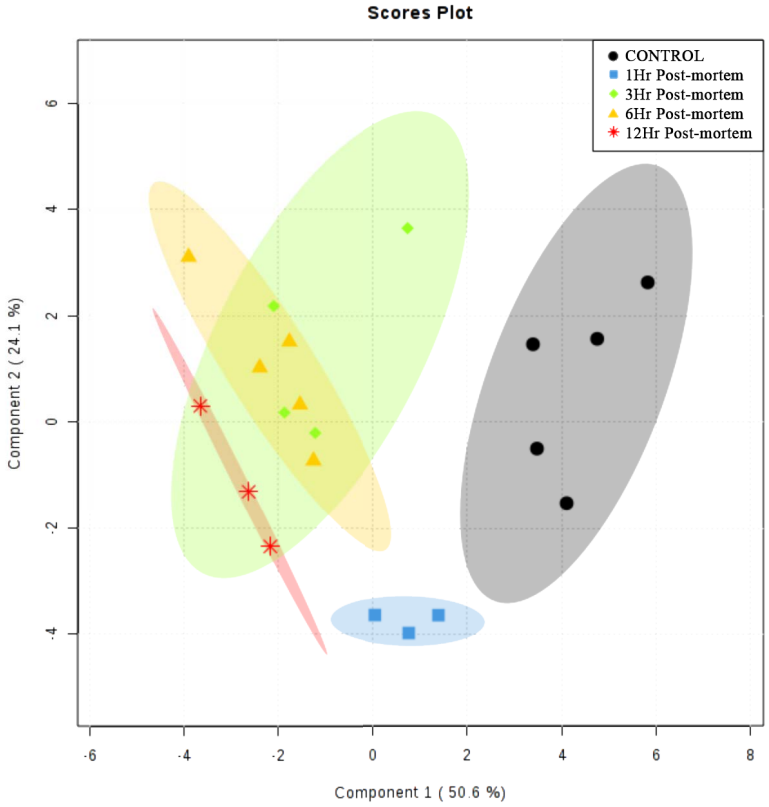
Scores Plot
CONTROL
1Hr Post-mortem
3Hr Post-mortem
6Hr Post-mortem
12Hr Post-mortem
Component 2 (24.1 %)
Component 1 (50.6 %)

B)

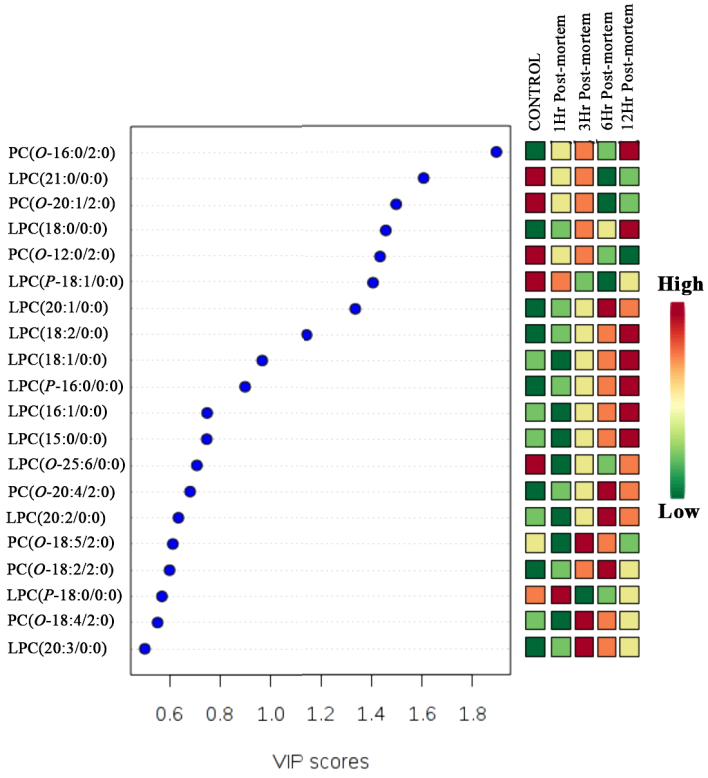
CONTROL
1Hr Post-mortem
3Hr Post-mortem
6Hr Post-mortem
12Hr Post-mortem
PC(O-16:0/2:0)
LPC(21:0/0:0)
PC(O-20:1/2:0)
LPC(18:0/0:0)
PC(O-12:0/2:0)
LPC(P-18:1/0:0)
LPC(20:1/0:0)
LPC(18:2/0:0)
LPC(18:1/0:0)
LPC(P-16:0/0:0)
LPC(16:1/0:0)
LPC(15:0/0:0)
LPC(O-25:6/0:0)
PC(O-20:4/2:0)
LPC(20:2/0:0)
PC(O-18:5/2:0)
PC(O-18:2/2:0)
LPC(P-18:0/0:0)
PC(O-18:4/2:0)
LPC(20:3/0:0)
High
Low
VIP scores

Figure 2. 5. Post-mortem delay disrupts GPC metabolism in the hippocampus.

All 46 species that were detected and profiled are displayed using hierarchical clustering with city-block distance metrics and average linkage. Data are represented as the log_2fold-change values compared to the control at 0-hour post-mortem, calculated based on the geometric mean at each post-mortem time group. GPC species are listed on the y-axis and post-mortem delay intervals are on the upper x-axis. The increase and decrease features are color-coded in each row by yellow and blue, respectively, compared to the control. Black indicates no change compared to the control.

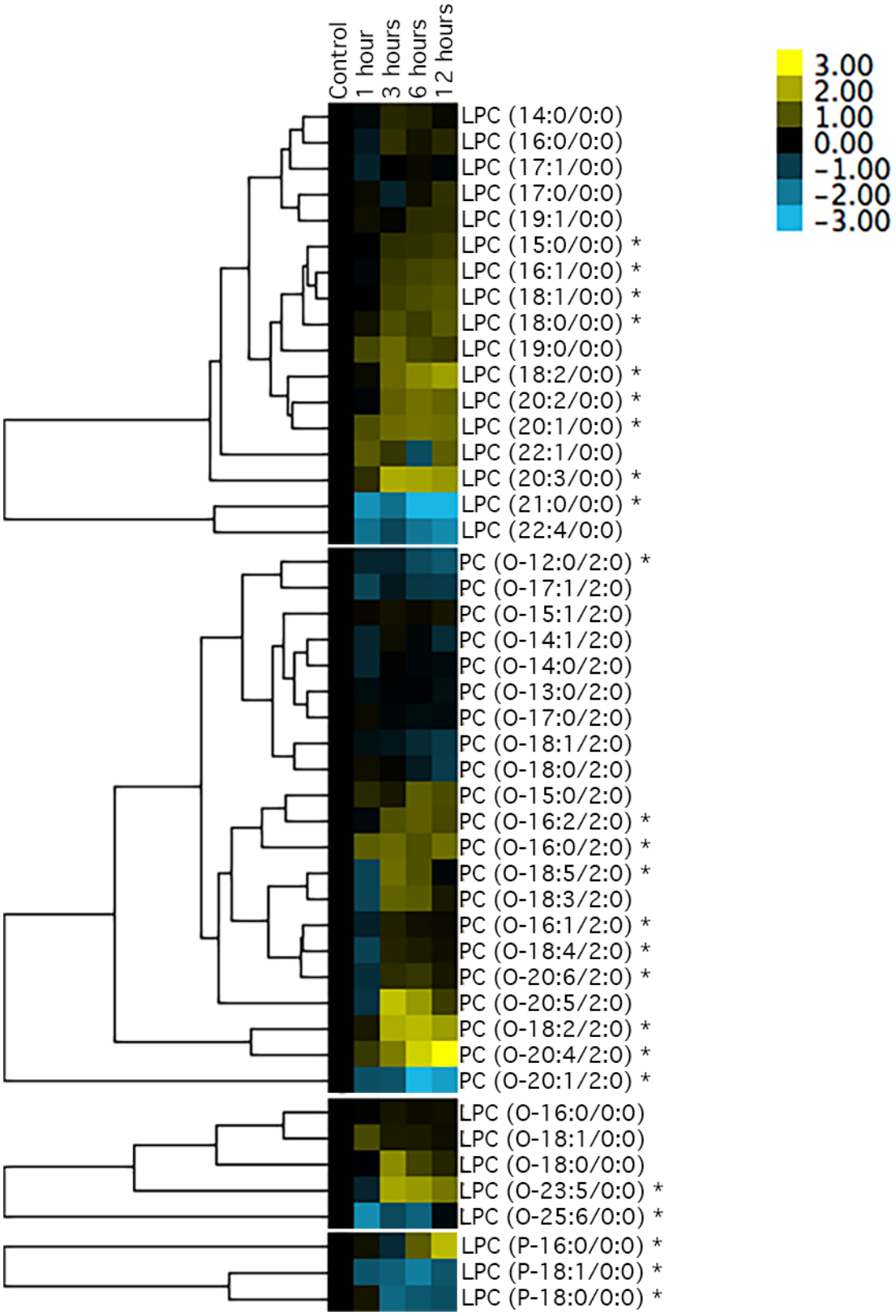
Control
1 hour
3 hours
6 hours
12 hours
3.00
2.00
1.00
0.00
-1.00
-2.00
-3.00
LPC (14:0/0:0)
LPC (16:0/0:0)
LPC (17:1/0:0)
LPC (17:0/0:0)
LPC (19:1/0:0)
LPC (15:0/0:0) *
LPC (16:1/0:0) *
LPC (18:1/0:0) *
LPC (18:0/0:0) *
LPC (19:0/0:0)
LPC (18:2/0:0) *
LPC (20:2/0:0) *
LPC (20:1/0:0) *
LPC (22:1/0:0)
LPC (20:3/0:0) *
LPC (21:0/0:0) *
LPC (22:4/0:0)
PC (O-12:0/2:0) *
PC (O-17:1/2:0)
PC (O-15:1/2:0)
PC (O-14:1/2:0)
PC (O-14:0/2:0)
PC (O-13:0/2:0)
PC (O-17:0/2:0)
PC (O-18:1/2:0)
PC (O-18:0/2:0)
PC (O-15:0/2:0)
PC (O-16:2/2:0) *
PC (O-16:0/2:0) *
PC (O-18:5/2:0) *
PC (O-18:3/2:0)
PC (O-16:1/2:0) *
PC (O-18:4/2:0) *
PC (O-20:6/2:0) *
PC (O-20:5/2:0)
PC (O-18:2/2:0) *
PC (O-20:4/2:0) *
PC (O-20:1/2:0) *
LPC (O-16:0/0:0)
LPC (O-18:1/0:0)
LPC (O-18:0/0:0)
LPC (O-23:5/0:0) *
LPC (O-25:6/0:0) *
LPC (P-16:0/0:0) *
LPC (P-18:1/0:0) *
LPC (P-18:0/0:0) *

is an overall increase in LPC species and LPC(*O*) in post-mortem delays, with exceptions of LPC(21:0/0:0), LPC(22:4/0:0) and LPC(*O*-25:6/0:0) whose abundances showed gradual decreases overtime. PC(*O*) PAF and LPC(*P*) species showed a species-specific fluctuation pattern in lipid abundance. (PC(*O*-16:0/2:0) with a saturated fatty acyl chain at the *sn*-1 position showed significant increase at 1 hour post-mortem while those with a PUFA at the *sn*-1 displayed a slower increase and only showed significance at later post-mortem time between 3 and 6 hours (PC(*O*-16:2/2:0), PC(*O*-18:5/2:0), PC(*O*-18:2/2:0), PC(*O*-20:6/2:0), PC(*O*-20:4/2:0). Two *lyso*-plasmalogen species, LPC(*P*-18:1/0:0) and LPC(*P*-18:0/0:0) showed a decrease in abundances at 1 and 3 hours post-mortem, after which they remained unchanged till the end of the experiment. Some decreases in specific LPC, LPC(*O*) and PC(*O*) PAF metabolites were observed as early as 1 hour post-mortem, followed by incremental changes in abundance at 3-12 hours post-mortem. These hierarchical clustering analyses suggest that not only does post-mortem delay disrupts GPC metabolism by resulting in significant changes in lipid abundances, the disruption is not linear and fluctuates at different PMI.

2.7 DISCUSSION

In this study, we showed for the first time that the composition of bioactive GPC membrane metabolites in the hippocampus is affected by post-mortem delay in tissue collection. A significant ($p < 0.05$) decrease in five GPC species (LPC(21:0/0:0, PC(*O*-18:4/2:0), PC(*O*-20:1/2:0), LPC(*O*-25:6/0:0), LPC(*P*-18:1/0:0)) defines the first hour post-mortem disruption. These species were also accountable for the differentiation of 1 hour post-mortem from the control, and from the rest of PMI groups. We found that post-mortem disruption in LPC and LPC(*O*) *lyso*-PAF metabolism brought about a dramatic increase in the majority of LPC metabolites between 1 and 3 hours post-mortem. In PAF metabolism, it was revealed that dramatic increases between 0 hour and 1 hour, and between 0 hour and later post-mortem time groups occurred in a species-specific manner,

namely, chain-length-specific. Specifically, a significant increase of about 2-fold at 1 hour compared to the control group only occurred to PC(*O*-16:0/2:0). Meanwhile, the PUFA-containing PAF species PC(*O*-16:2/2:0), PC(*O*-18:5/2:0), PC(*O*-18:2/2:0) and PC(*O*-20:4/2:0), PC(*O*-20:6/2:0) increased significantly at 3hours post-mortem and at 6 hours post-mortem, respectively. A more gradual incremental increase in all significantly-changing metabolites was detected from 6-12 hours post-mortem, suggesting that it will be beneficial to combine clinical samples flash-frozen within a 6-12 hours post-mortem delay to avoid post-mortem artifacts.

The majority of studies profiling metabolites from brain tissues are done posthumously. It is therefore critical to understand and recognize underlying signatures of biochemical degradative processes in order to differentiate between artifacts due to post-mortem changes and true pathological alterations. In this study, sodium pentobarbital, more commonly known as Euthanyl, was used in an overdose manner to euthanize mice. Intraperitoneal (IP) injection of Euthanyl at a toxic dose caused the animal to enter unconsciousness within two minutes, cease to perform proper respiration after six minutes, lose heartbeat in about eight minutes causing disruption in blood circulation ("medically death") and reach the state of "clinically death" at approximately 10 minutes[192]. Our protocol started the decapitation process for brain tissue collection after 15 minutes when all signs of life had been confirmed to be absent. Hence, all animals were confirmed to die due to respiratory failure, a consequence of Euthanyl[193]. As this is the primary cause of death, findings in this study do not only reflect the changes occurring over PMI but are also associated to the consequences of a depressed respiratory system. It has been noted previously in literature that during the two minutes elapsed between medical and clinical death, the animal may go through an agonal period in which its heart fibrillates and there are involuntary signs of gasping for air[192]. This two-minute agonal period may contribute to the GPC profiling in post-mortem tissues.

I showed uniquely that the early post-mortem time (up to 1 hour post-mortem) depletes the brain of the bioactive PAFs, PC(*O*-18:4/0:0) and PC(*O*-20:1/0:0). These data suggest a disruption in the remodelling pathway (Land's cycle) of forming PAF from its immediate *lyso*-PAF precursor (LPC(*O*)) via the acetylation activity of LPCAT[194]. Subsequently, my data indicated that metabolic breakdown products of structural phospholipids (LPC, LPC(*P*)) dramatically increase 3 hours post-mortem and the elevated levels remain relatively stable up to 12 hours post-mortem. These data are consistent with previous results indicating that hypoxia and anoxia result in activation and over-release of PLA_2[195-197]. PLA_2 is responsible for the hydrolysis of *sn*-2 fatty acyl chains from GPCs[198]. In neural membranes, PLA_2 acts in concert with LPCAT to control the GPC composition of the lipid membrane and ensure proper release of PUFA, such as arachidonic acid and docohexaenoic acid. PLA_2 carries out the deacylation of GPC at the *sn*-2 position, where PUFA usually occupies[10, 199-200], while LPCAT performs the re-acylation by incorporating any free fatty acid available to regenerate GPC[201]. LPCAT is also able to reacetylate a *lyso*-GPC species; when the GPC has an ether linkage at the *sn*-1 (i.e. *lyso*-PAF or LPC(O)), the reacetylation by LPCAT forms PAFs. Impairment of LPCAT likely occurs early as indicated by a reduction in re-acetylated PAFs from LPC(O) in the first hour post-mortem. Previous studies have shown that anoxia stalls ATP production and thereby decreases LPCAT activity[201-202], given that regulation of deacylation/reacylation in neural membranes is sensitive to changes in ATP/ADP ratio.

While specific PAF species PC(*O*-18:4/2:0) and PC(*O*-20:1/2:0) were impaired at 1-hour post-mortem and mainly contributed to the overall reduction in PAF mol% of total GPC composition, 35% of PAF species showed significant increases in abundance between 3 and 12 hours post-mortem. Interestingly, all of these PAF species were PUFA-containing species. Only one PAF species, PC(*O*-16:0/2:0) was found to increase within the first hour post-mortem. The increase of PC(*O*-16:0/2:0) was not accompanied by a significant change of its immediate *lyso*-PAF precursor,

LPC(*O*-16:0/0:0), suggesting that LPCAT acetylation likely did not play a role in this observation. This, again, confirms the impairment of LPCAT as observed above. The marked increase in PUFA-containing PAF at later PMI is intriguing as cessation of blood flow and oxygen to the brain (i.e. hypoxic/anoxic condition) is not suitable for enhanced activity of fatty-acid desaturases[203]. In addition, PUFA-containing species possess very high oxidative potential due to the double bonds, which have low C-H bond energy, in the hydrocarbon chain[204]. This usually leads to a reduction of PUFA-containing species as a consequence of phospholipid oxidation, which is not observed here. One possible cause is the impaired catabolism of PAF by PAF-AH. The production of PAF may have been overstimulated during the agonal period as a pro-inflammatory response to the cessation of blood flow and oxygen to the brain. This would lead to a rise in PAF production, however, PAF-AH may still have been active and metabolized PAF during the first hour post-mortem. Up to 3 hours post-mortem, the hydrolysis activity of PAF-AH finally got impaired due to post-mortem conditions, leaving accumulating PAF species at later PMI. This explanation will also account for species whose abundances remained unchanged, or decreased during the first hour post-mortem, and then changed dramatically by two- to three-fold increase at 3 hours post-mortem (PC(*O*-16:2/2:0), PC(*O*-18:5/2:0), PC(*O*-18:2/2:0), PC(*O*-20:6/2:0)). Further enzymatic assays would be useful in confirming this speculation. Overall, the results of PAF profiling in this study highlight the fact that care must be taken in interpreting levels of these GPC second messengers in post-mortem human tissue given these unpredictable fluctuations.

Plasmalogens, or 1-*O*-(1Z-alkenyl), belong to a family of phospholipids that contains a vinyl ether bond linkage at the *sn*-1 position[205]. The major role of plasmalogens in the lipid plasma membrane is to maintain its structure and other physical properties[200]. In this study, we profiled the metabolite of plasmalogen PC (PC(P)), namely *lyso*-plasmalogen, LPC(P). We identified three LPC(P) species, LPC(*P*-16:0), (*P*-18:0), and (*P*-18:1), within the profiled mass range. These are

the most common fatty alcohols found at the *sn*-1 position of plasmalogens[206-207]. It was observed that total LPC(P) abundance increased significantly in the post-mortem hippocampal tissue and this is due to the dramatic rise in the concentration of LPC(*P*-16:0). Similar to LPC, *lyso*-plasmalogens are also the product of phospholipases including PLA_2[208], and the exponential increase of LPC(*P*-16:0) may be explained by the PLA_2 over-stimulation in post-mortem tissues. The decrease in the other two *lyso*-plasmalogen species is likely due to plasmalogen's high oxidative potential. The vinyl ether linkage on the fatty alcohol at the *sn*-1 position is very prone to oxidation by free radicals and reactive oxygen species (ROS)[209-210]. Free radicals and ROS are ubiquitous in the body, including the brain. In fact, they are part of normal physiological processes[211]. Free radicals are generated and consumed in multiple different biochemical pathways. In the brain, they could come from excitatory amino acids and neurotransmitters[212]. Due to the constant exposure to oxidative species, the body and the brain require defense mechanisms such as readily available antioxidants and ROS scavengers to eliminate the harmful oxidative reactions. Plasmalogens have been proposed to be ROS scavengers due to their preference for vinyl ether over other linkages found in GPCs[209]. Death likely leads to an excess production of ROS due to disruptions in all biochemical processes[213-214], resulting in oxidative reactions with the identified LPC(*P*). Although plasmalogen-PCs and the metabolite *lyso*-plasmalogen PCs are not very abundant in the brain (versus plasmalogen PEs), the dramatic rise in LPC(*P*-16:0/0:0) by three-fold and the depression of LPC(*P*-18:1/0:0) and LPC(*P*-18:0/0:0) occurring early in post-mortem times strongly suggest that different plasmalogen species may be more vulnerable to disruption by post-mortem delay than others.

The fluctuation in different components of GPC content in mouse hippocampus at different post-mortem time suggested that disruption of the lipidome metabolism exists and is complicated by a broad range of post-mortem biological changes. The species-specific decreasing pattern found

in PAF and LPC(*P*) abundance suggests that these species may play a role in the lipidome that has not been identified before. This role may be vital, since their abundances dropped as life cessation occurred. Further investigation in these species will reveal information that is helpful to further the understanding of the lipidome.

2.8 FUTURE DIRECTION

This study has showed that death is a process and results to a cascade of cellular events which are reflected in the lipidome at different PMI. There are still ambiguities about the underlying mechanisms leading to different patterns observed in the GPC metabolite and second messengers. Future work should focus on expanding the profiled mass range to also cover the diacyl-, alkyl-acyl, alkenyl-acyl GPC (plasmalogen-PC), which usually exist in the plasma lipid membrane[10]. Linking these changes to those that were found in GPC metabolite and second messengers in this study will complete the picture of how the overall GPC metabolism is disturbed after death. Studies looking into post-mortem enzymatic activities of important enzymes in membrane lipid metabolism such as PLA_2, LPCAT, PAF-AH and desaturases will confirm their roles in the degrading neural membrane. Furthermore, collecting total GPC contents in other part of the brain such as the temporal-posterior-entorhinal cortex will allow a fair comparison and detection of region-specific metabolic processes. A collection of oxidative fragments and products will support the hypothesis that degradation of LPC(*P*) or PC(*P*) species is due to oxidation processes. In addition to the GPC contents, glycerophosphoethanolamine (GPE), glycerophosphoserine (GPS) and glycerophosphoinositol (GPI) are also important phospholipids in the brain. GPE is the second most abundant phospholipids in brain cells and modulate the assembly of cellular plasma membrane[215]. Meanwhile, GPS is enriched in the intracellular leaflet of the neural plasma membrane[215-216] and GPI is more abundant in neural than any other tissues[217-218]. All of these glycerophospholipids, combining with GPC are important membrane constituents and take part in

essential metabolic regulation. In order to obtain a better understanding of and to draw a complete the picture of membrane breakdown in post-mortem state, future profiling of these other glycerophospholipid families and the long-chain lipid species must be performed.

2.9 CONCLUSION

The profiling of GPC metabolites and second messengers in this study has generated two speculations: GPC metabolism is significantly disrupted by post-mortem delay in the hippocampus and this disruption results in fluctuating GPC metabolite abundances at different PMI in a species-specific manner. The compositional changes in total GPC and the levels of the majority of LPC and PAF species changed within the first hour post-mortem. There were species-specific patterns in the fluctuation of PAF and *lyso*-plasmalogen PC levels, which may be due to agonal factors. Generally, the hippocampal GPC metabolite lipidome appears to be most stable during 3-6 hours post-mortem, suggesting that tissues collected at this PMI may be collected together for reliable profiling. Finally, it is important to note that the altered GPC metabolite profiles found here are consistent with the reports from previous studies on the changing levels of LPCs, PAFs, and *lyso*-plasmalogen PCs in neurodegenerative subjects. This emphasizes the importance of strictly monitoring the post-mortem delay in future research, by ensuring the time period between death and autopsy is consistent amongst all subjects and tissues to avoid post-mortem artifacts that will interfere with studying the lipidome.

CHAPTER 3 - SIMULTANEOUS IMAGING OF LIPIDS IN MURINE BRAIN USING AP-MALDI IMS COUPLED TO AN ORBITRAP MS

3.1 OBJECTIVE OF THE STUDY

As shown in Chapter 2, the hippocampal GPC lipidome changes in post-mortem. These changes were hypothesized to be due, in part, to anoxia. This hypothesis also suggested that post-mortem changes may be regionally specific depending upon the timing of anoxia in differentially vascularly perfused brain tissue. Rather than profile all regions by LC-ESI MS, I sought to develop IMS methodology capable of locating and visualizing post-mortem and disease specific changes in multiple lipid classes *in situ.*

3.2 AUTHOR CONTRIBUTIONS

Thao Nguyen, Steffany Bennett, and Maxim Berezovski conceived and designed the experiments. Mark Akins was responsible for the perfusions and sectioning of brains. We gratefully acknowledge the expertise of David Lamelin from Dr. Jean-Claude Beique's lab (uOttawa) who provided us with the hydrogel monomer solution for the CLARITY procedure, as well as the optimized protocol for this technique. Thao Nguyen performed all of the methodology development and analyses and wrote the paper under the supervision of Drs Hongbin Xu, Maxim Berezovski, and Steffany Bennett.

Simultaneous imaging of lipids in murine brain using AP-MALDI IMS coupled to an Orbitrap MS

Thao T. Nguyen-Tran[1,2,3], Mark Akins[1], Hongbin Xu[1], Steffany.A.L. Bennett[1,2,] Maxim Berezovski[2,3]

[1]Neural Regeneration Laboratory, India Taylor Lipidomic Research Platform, Ottawa Institute of System Biology, Brain and Mind Research Institute, Department of Biochemistry, Microbiology, and Immunology, University of Ottawa, Ottawa, Ontario, Canada

[2]Centre for Catalysis Research and Innovation, Department of Chemistry and Biomolecular Sciences, University of Ottawa, Ottawa, Ontario, Canada

[3]John L. Holmes Mass Spectrometry Facility, Department of Chemistry and Biomolecular Sciences, University of Ottawa, Ottawa, Ontario, Canada

3.3 ABSTRACT

Post-mortem changes of the glycerophosphocholine (GPC) lipidome in mouse hippocampus were reported in Chapter 2. Mapping these changes in comparison to other regions within the brain *in situ* will reveal essential information about localization and metabolism of lipids in the brain after death critical for any and all post-mortem analysis of human brain. Here, a novel mass spectrometry approach was optimized and utilized establishing a new reliable, method for assessing the distribution of lipids in brain tissues. I focused on developing a matrix-assisted laser desorption/ionization (MALDI) MS methods to map distribution of PCs, ceramides, and

sphingomyelins *in situ* exploiting high resolution/high mass accuracy analysis to identify species at the molecular level.

3.4 INTRODUCTION

MALDI-imaging mass spectrometry (MALDI-IMS) is a valuable analytical tool for mapping the distribution of biomolecules in tissues. As reviewed in Chapter 1, this technique, especially when performed at atmospheric pressure, is useful for lipid analysis. In Chapter 2, the hippocampal GPC lipidome was scrutinized in post-mortem tissues using the "gold-standard" of quantitative mass spectrometry, LC/ESI-MS/MS. This involved extraction of lipids from brain tissues and thus destruction of tissue architecture. To further document the kinetics of lipidome changes attributed to post-mortem delay and assess whether different brain regions exhibit different temporal changes, a rapid method of profiling multiple lipid species is required. MALDI-IMS is the only method that is able to generate high-resolution molecular images of tissues and molecular mass analysis of target molecules simultaneously[70, 219]. Thus, MALDI-IMS enables the analysis of distributional changes of lipid species via MS/MS, in order to reveal fluctuations in the lipidome due to different biochemical states. Here, I sought to develop such a method that could be applied to post-mortem assessment and disease-specific interrogation of lipidomic changes in brain tissue.

The conventional set-up of MALDI-IMS includes a vacuum MALDI source coupled to a TOF mass analyzer. The traditional TOF mass analyzer, as described in Chapter 1, is limited by vacuum-related complication such as in-source decay, and inability to perform fragmentation post analysis in the time-of-flight tube. These limitations challenge the identification of lipids and lipid metabolites[172]. In shotgun lipidomic analyses, reliable lipid identification requires good peak separation, low-ppm (< 1 ppm) mass accuracy measurement, and interpretable MS/MS data from selected precursor ion to distinguish between species from different families with similar m/z[220]. The introduction of high-resolution (maximum 140,000 resolving power at m/z 200) mass

spectrometers, such as the Orbitrap, provides a powerful approach to visualizing lipids in tissue sections, especially when it is coupled to AP-MALDI to perform IMS. With highly accurate mass measurement, MALDI-IMS on an Orbitrap instrument, in combination with the higher-energy collisional dissociation (HCD) collision cell for MS/MS, would theoretically allow for a more precise detection of lipid distribution and characterization of structures.

In MALDI-MSI experiments, identification of a target compound (or a class of compounds) based on mass accuracy can be verified by the comparison of images from tissues from which the target compounds have been depleted (for example, tissue from a null-mutant animal in the case of proteins). Such genetic controls are not available for lipids. However, new tissue delipidation processes developed for deep-tissue fluorescent imaging commonly employ different tissue washing protocols which solubilize most of the lipid contents in order to reduce light scattering and enhance tissue transparency[221-223]. A new protocol known as CLARITY has emerged as an efficient method to clear tissues chemically by dissolving lipid membranes without disrupting the structural framework provided by proteins[157, 224]. This method relies on hydrogel infusion to provide a support for the tissue structure, after which lipid contents are cleared by immersing the hydrogel containing the tissue in an ionic/hydrophilic solvent. CLARITY has been used in whole brain imaging, to visualize neuronal circuits in the spinal cord[225], whole embyro[226], as well as other organ imaging[227].

Here, I sought to exploit this and other standard tissue delipidation protocols to develop a new methodology, combining AP-MALDI and high resolution/accurate mass measurement, that would unambiguously profile, identify, and localize GPCs, ceramides, and sphingomyelins *in situ* in formalin-fixed (FF) brain tissue. It had been shown previously that FF tissue samples revealed similar mass spectrometry peak profiles to those that were freshly frozen[158, 228]. Hence, FF brain tissues are suitable for lipid imaging by MALDI-MS. In addition to utilizing MS/MS for the

identification of lipid species, two chemical clearing methods, CLARITY and the traditional approach that uses a xylene/Citrasolv clearing agent, were also employed to validate the lipid identity of the species found by mass spectral data. This study represents the first lipid-IMS work unambiguously confirmed by delipidation methods. Furthermore, CLARITY has used for high-resolution microscopy processing. Thus, this study represents the first time, MALDI-IMS has been combined with CLARITY to produce lipid-specific image analysis in FF brain tissue.

3.5 MATERIALS & METHODS

3.5.1. Animals

For this study, a 4-month-old wild-type mouse with an N4 C57BL/6J x 129/SV genetic background was lethally anesthetized with 65 mg/ml euthanyl (#1EUS001, Bimeda-MTC Animal Health Ins., ON, Canada) and perfused transcardially with 10 mM phosphate buffered saline (PBS; 10 mM phosphate at pH 7.2, 154 mM NaCl, followed by 4% (v/v) paraformaldehyde (PFA, #F1635, Sigma-Aldrich, ON, Canada) in 10 mM PBS.

3.5.2. Tissue sectioning

Following euthanization, the intact brain was removed and post-fixed for 24 hrs in the same perfusion media described above. It was subsequently cryoprotected in 20% sucrose (20% (w/v) sucrose, #SUC507.5, BioShop, ON, Canada; 0.001% (w/v) sodium azide (NaN_3, #S2002, Sigma-Aldrich, ON, Canada), in 10 mM PBS. Serial 20 μm coronal cryosections were cut in a 1 to 10 series from bregma -1.10 to -3.10 mm at -20^{o}C on a Leica Microsystems CM 1900 cryostat (Wetzlar, Germany). Sections were stored in 10 mM phosphate buffer (PB) with 0.1% NaN_3 at 4^{o}C until delipidation or preparation for MALDI-Imaging.

3.5.3. Lipid Clearing

i. CLARITY

Brain sections were incubated individually in the hydrogel monomer solution (1% acrylamide, 0.0125% bisacrylamide, 4% PFA, 0.25% VA-044 initiator (w/v) in 1X PBS) (#161-0140, #161-0142, Bio-Rad, ON, Canada; VA-044 from Wako, Richmond, VA, USA) in a 24-well plate for 65 hours at 4^{o}C. The gel was polymerized at 37^{o}C for 5 hours. The brain slices were then removed from the hydrogel monomer solution and transferred to another 24-well plate prefilled with 200 mM NaOH-boric buffer pH 8.5 (NaOH #B10252 BDH Inc., Toronto, ON, Canada; Boric Acid #A74, Fisher, Fair Lawn, New Jersey, USA) containing 8% SDS (sodium dodecyl sulfate, #15525-017, Invitrogen, Carlsbad, CA, USA) for 20 hours. After washing, in order to remove residual paraformaldehyde and hydrogel monomers, the brain slices were passively cleared by incubating in 100 mM Tris-Boric Buffer pH 8.5 (Tris-base #T-1503, Sigma-Aldrich, ON, Canada) containing 8% SDS at 40^{o}C for 171 hours (~7 days). Over the 7 days, the buffer was replaced with fresh portions daily. After clearing, the brain slices were washed in 10 mM PB containing 0.2% (v/v) Triton-X100 (#T8787, Sigma-Aldrich, ON, Canada) for 24 hours at 37^{o}C to remove SDS. The brain slices were then stored in 10 mM PB containing 0.1% sodium azide w/v (without Triton-X100).

ii. CITRISOLV (Xylene substitute)

Mouse brain slices were first washed in double-distilled water (ddH_2O) for 2 minutes. They were then dehydrated by incubating in a gradually increasing concentration of ethanol (10%, 25%, 45%, 60%, 75%, 95%, 100%) (#P016EAAN, GreenField Ethanol, ON, Canada). The slices were incubated in each of the first five concentrations for 3 minutes and in 95% and 100% for 5 minutes. They were then placed in CitriSolv solution (#22-143975, Fisher Scientific, USA) for 171 hrs (~7 days) before being stored in 10 mM PB containing 0.1% sodium azide w/v until further analysis.

3.5.4. Matrix sublimation

The sublimation apparatus was purchased from Chemglass Life Sciences (Sublimation apparatus, # CG-3038, Vineland, NJ, USA). The apparatus contained 2 pieces, as shown in Figure 3.1A. The inner piece was a flat round-bottom condenser with a diameter of 75 mm and fitted with a 44 mm x 44 mm MALDI stainless-steel plate (ABI Opti-TOF 192, AB SCIEX, Framingham, MA, USA). The MALDI plate with brain slices mounted was affixed on the underside of the condenser using double-sided tape and regular tape (# 7000126636, #700136846, 3M-Scotch, St. Paul, MN, USA), as seen in Figure 3.1B. Depending on the kind of tissue used – frozen (stored at -20^{o}C) or cold (stored at 4^{o}C) – a mixture of ethanol (#BP28184, Fisher Scientific, ON, Canada) and dry-ice or of water and ice was used as a coolant, respectively. The coolant was added to the inside of the inner condenser (Figure 3.1C).

Matrix compound 2,5-dihydroxybenzoic acid (DHB, # 85707, Sigma-Aldrich, ON, Canada) was used for all MALDI experiments. Approximately 50 mg of 2,5-DHB was weighed out and added to the bottom of the outer flask. The two pieces of the sublimation apparatus were then assembled together with a rubber O-ring for sealing. The entire apparatus was then brought to vacuum condition, to approximately 50 mTorr pressure.

A trapping set-up was done by using a 2 m long tube (0.5 inches inner diameter), coiled into 2 circles to trap any vapors created during sublimation by the vacuum flow. Since this sublimation procedure was a dry method, contamination by volatile reagents was not of concern. After connecting the system, the pump (Fischer technical high vacuum pump, LV-3, Fischer Technical Company, Roselle, IL, USA) was started and the entire system was allowed to equilibrate under

Figure 3. 1. Schematic set-up of sublimation apparatus and matrix application process on MALDI plate.

(A) The sublimation apparatus glassware consisted of two-pieces: the inner condenser and the outer flask. Both were connected and sealed by a rubber O-ring. **(B)** The MALDI-plate was affixed onto the outside of the bottom of the inner condenser by tape. **(C)** Assembly of the apparatus once ready for sublimation with matrix power and coolant liquid (EtOH & dry ice or ice-water bath) added.

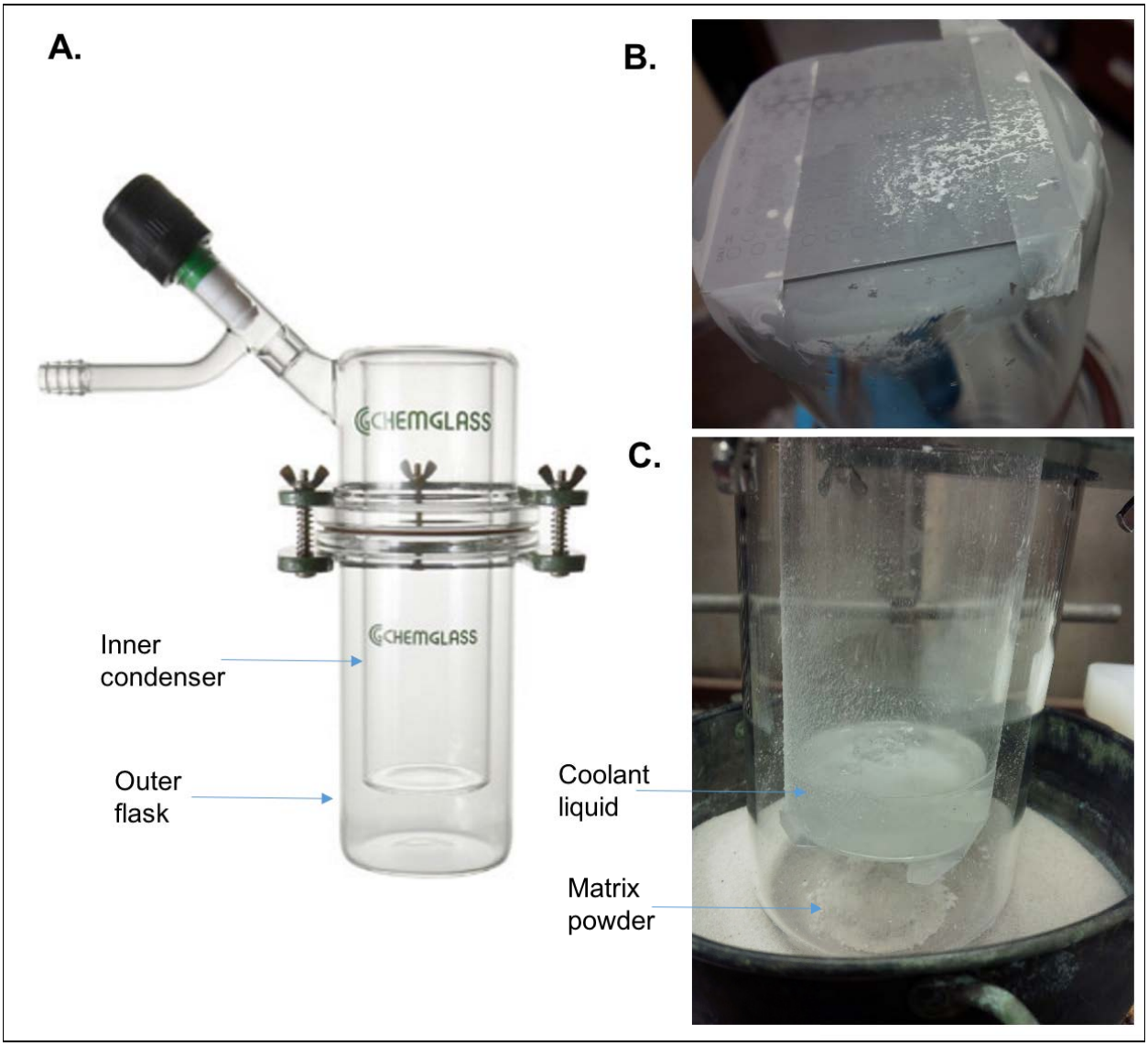
A.
B.
C.
CHEMGLASS
CHEMGLASS
Inner condenser
Outer flask
Coolant liquid
Matrix powder

vacuum for about 15 minutes. Meanwhile, a sand bath was heated up to 100^{o}C. When temperature reached this point, sublimation was initiated by placing the bottom of the sublimation apparatus in contact with the sand bath, and allowing it to heat up to 120^{o}C. This took approximately 5 minutes, after which matrix could be seen collected around the walls of the outer flask, as high as where the inner condenser is. Sublimation was then stopped, first by removing the system from heat and coolant, allowing it to return to room temperature, for 2-3 minutes. Next, the vacuum pump was shut off, and the system slowly returned to atmospheric pressure. Finally, the apparatus was dissembled and the MALDI plate was removed. The plate was then placed in a small and closed chamber with desiccators to dry and to avoid water vapors in the air until ready to be analyzed by mass spectrometry. Figure 3.2 presents the complete setup of the apparatus.

3.5.5. Matrix coating thickness measurement

The MALDI plate was weighed before and after matrix deposition (without tissue) to determine the actual amount of matrix deposited onto plate. The plate coated with matrix-only was then used to assess coating thickness by 3D z-stack measurement using an Olympus confocal microscope (BX-60, Olympus America Inc., Center Valley, PA). DHB matrix was excited at 405 nm, while the MALDI plate's stainless steel area was excited at 488 nm. Using both lasers simultaneously, the depth of the matrix layer could be determined by taking z-stack images from the surface of the matrix layer to the surface of the plate (where matrix layer emission was no longer observed).

3.5.6. MS and data analysis

MALDI-IMS analysis of lipids were performed on an AP-MALDI source (MassTech Inc., Columbia, Maryland, USA) coupled to a hybrid quadrupole - Orbitrap mass spectrometer, Thermo

Figure 3. 2. Complete set-up of sublimation apparatus.

The sublimation glassware contained two condensers which were tight-sealed and brought down to a vacuum by being connected to vacuum pump. The connecting hose acted as a cold-trap to collect impurities during the sublimation process. The hotplate was equipped with a sand bath to provide an even heating interface around the bottom glass condenser of the sublimation glassware, where matrix solids had been placed.

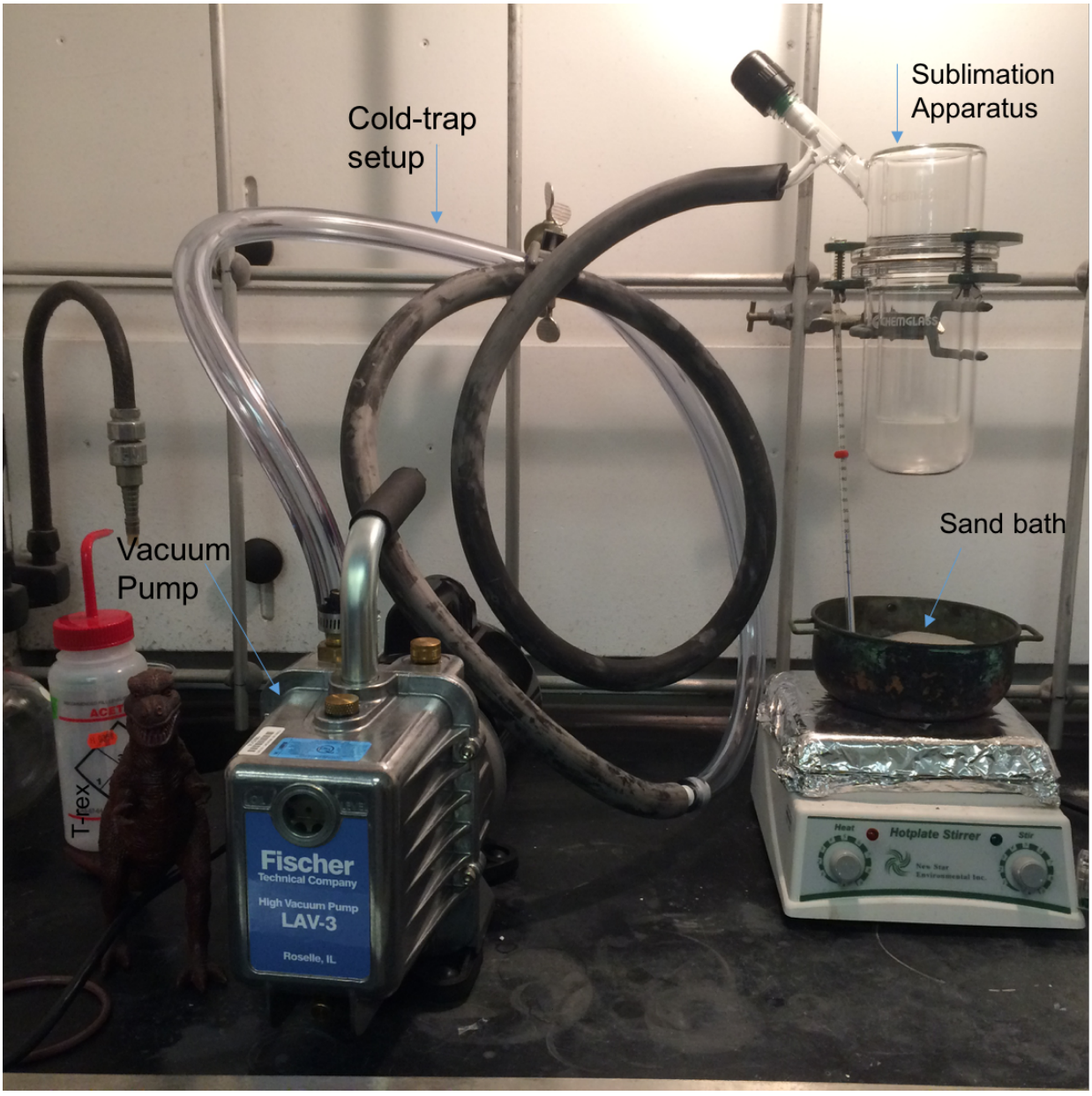
Cold-trap
setup
Sublimation
Apparatus
Vacuum
Pump
Sand bath
Fischer
Technical Company
High Vacuum Pump
LAV-3
Roselle, IL
Hotplate Stirrer
Heat
Stir
T-rex

Scientific™ Q Exactive™ Plus (Thermo Fisher Scientific, San Jose, USA). The XY stage (MALDI plate holder) was installed at a distance of 1.75 mm from the inlet leading into the mass spectrometer. The all-solid-state Nd:YAG laser operated at 355 nm, at 8 μJ per pulse with repetition rate of 10 kHz. The AP-MALDI source was set to create position information in constant-speed raster motion (CSR) mode, a feature of the Target software (version 7.1, MassTech Inc.) accompanying the source. This mode allows the x,y-stage to move in a pre-defined direction and speed while the laser constantly fires. The laser only stops during transition between rastered lines. With this mode, a pixel is defined by the number of resulting spectra from the defined mm per each minute (ie. speed of stage). The speed of the stage was calculated based on the scan rate to ensure each pixel contained at least a spectrum. The laser beam size was adjustable and was set at 70 x 100 μm (x by y elliptical dimension) for all experiments. Spatial resolution was at 50 μm for all recorded images.

The Q Exactive Orbitrap instrument operated in the positive ion reflectron mode for all lipid analysis, in the mass range of m/z 100-1100 at mass resolution of R = 70,000 at m/z 200. The parameters set for the interface between the MALDI source and the capillary leading into the mass spectrometer were as followed: "spray" (or plate) voltage: 2.00 kV; capillary temperature: 350^{o}C, S-lens RF level: 100.0; all of sheath gas, aux gas and sweep gas were off. At first, all mass spectra were acquired in full scan mode for image generation. Afterward, a region within the brain was selected for lipid species detection by data-dependent MS/MS (ddMS^2). MALDI mode at this point switched from rastering mode to spiral mode for efficient collection of ions for fragmentation experiment in the HCD cell. This method involves first a full-MS scan at same mass resolution as in the imaging experiment; with AGC target of 1 x 10^5 ions and maximum injection time (IT) of 300 ms. The ddMS^2 scan that follows was acquired at mass resolution of R = 17,500 at m/z 200

and scan range of 200-1100. Isolation window was set at 4.0 m/z and AGC target was set to 5 x 10^4 with maximum IT was at 200 ms. Normalized collision energy was set at 47 eV.

Lipid identification required four steps: 1) determine the ions that were found to be present in brain (and not in the matrix only area); 2) examine the fragmentation pattern and check for presence of product ions m/z 184, 263.4 or both diagnostic of glycerophosphocholines, ceramides, or sphingomyelin's respectively[136, 229]; 3) search for lipid identity using the exact mass of "found" species in the LIPID MAPS library (www.lipidmaps.org/tools/index.html) and VALID database (www.neurolipidomics.ca/valid.html) with mass accuracy of +/- 5ppm and 4) compare the presence of identified ions in non-delipidated slices (Intact) and in delipidated slices (CLARITY-Delipidated and Citrisolv-Delipidated brain slices). Target lipids in this study were identified to be $[M + H]^+$, $[M + Na]^+$. Species that were common in all brain slices but did not have recognizable fragment patterns or have their mass matched by LIPID MAPS and VALID database were excluded as non-lipid species.

3.6 RESULTS

As a proof-of-principle study, the work presented here investigated 1) the potential of sublimation as an effective matrix application for MALDI-IMS of lipids, and 2) the ability of the developed protocol to detect and identify lipids in brain tissue.

3.6.1. Sublimation of DHB matrix yields pure, uniform layer of microcrystals coating tissue sample.

The DHB matrix layer generated by sublimation was visually observed as a smooth and uniform coating on top of the MALDI plate (control) or the tissue. Control examples of this are shown in Figure 3.3A and 3.3B, where DHB matrix was applied onto a MALDI plate and observed using both charged-coupled device (CCD) camera installed in the MALDI source (Figure 3.3A) and by confocal microscopy (Figure 3.3B). It was found that optimal DHB matrix coating was

achieved using 8.5 mg of matrix compound, resulting in approximately 0.7 mg/cm^2 of coating. This gave rise to an average thickness of 8.4 ± 0.5 μm (n = 4) (Figure 3.4). In pilot experiments, 21.1 mg of matrix yielded a coating of 1.8 mg/cm^2 with a thickness of approximately 30 μm that was a very thick yet fragile matrix.

Measurement of the matrix crystal size was done by capturing an image of the matrix surface through a 40x objective and magnifying digitally to view individual crystals. Each crystal observed was then selected for size measurement (Figure 3.5). Under optimized conditions for sublimation (5 min of heating at 50 mTorr), the DHB matrix crystal sizes ranged from 1.6 μm to 3.0 μm in width, with an average area of 4.0 ± 1.4 μm^2. As crystal sizes were significantly smaller than the laser spot size (90 x 45 μm), they were considered sufficient for these imaging experiments in which spatial resolution was 50 x 50 μm. Hence, although the crystal sizes varied, their size differences were insignificant relatively to the lateral distribution that was examined. The optimal coating of DHB matrix (8.4 - 9.0 μm) was found to be thick enough to induce ionization of lipid molecules on the tissue surface, yet thin enough to not suppress signals from non-matrix ions.

3.6.2. Comparison of profiling spectra between Intact and CLARITY- or Citrisolv-delipidated brain slices in the m/z 100-350 mass range of matrix and small metabolite ions

Representative mass spectra of intact, CLARITY- and Citrisolv-delipidated brain slices at mass range m/z 100-350, in which matrix ions dominate are shown in Figure 3.6. These spectra were generated by averaging the same number of mass spectra across one same rastered region from each slice for comparison. In Figure 3.6, these spectra present the low mass range m/z 100-350, presumably dominated by matrix ions, detected by MALDI-IMS in positive ion mode as

Figure 3. 3. Optical and confocal microscopy images of sublimed DHB matrix on MALDI stainless steel plate.

(A) Optical image of matrix coating on MALDI plate, imaged using a CCD camera attached to the MALDI source. **(B)** Confocal microscopic image of the same sublimated matrix.

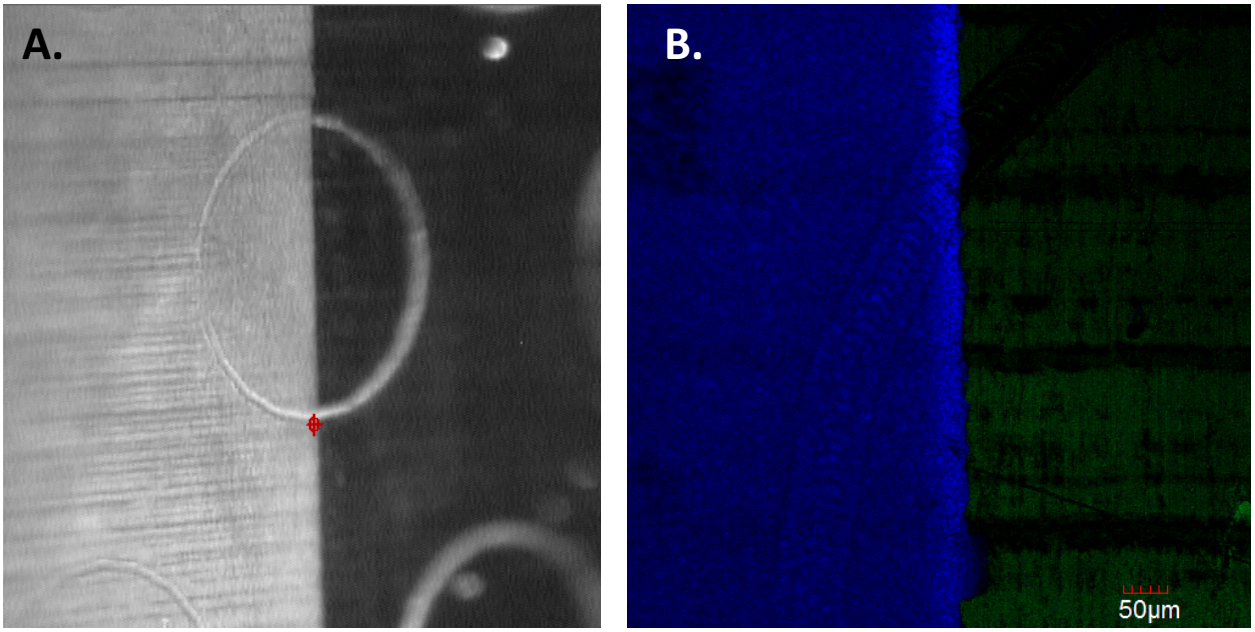
A.
B.
50µm

Figure 3. 4. Thickness measurement of the sublimed matrix coating on the MALDI stainless steel plate.

Matrix thickness was measured from randomly selected crystals. Crystals indicated by numbers were measured as follows: **(1)** length of 8.3 μm, **(2)** length of 9.3 μm, **(3)** length of 8.1 μm, **(4)** length of 8.2 μm. **(5)** indicates the interface between matrix and the MALDI plate where tape was applied.

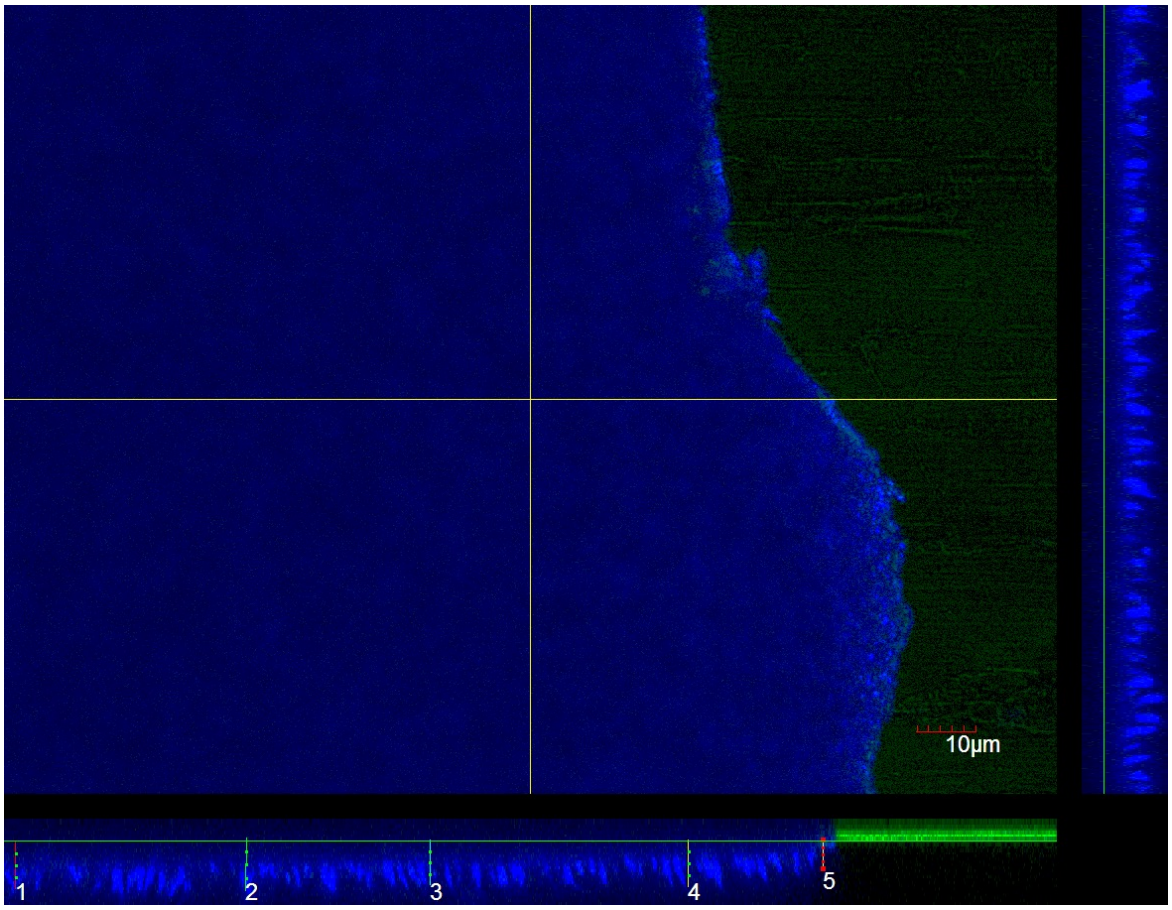
10µm
1
2
3
4
5

Figure 3. 5. Matrix crystal size measurement by confocal microscopy.

Confocal microscopic image of sublimated DHB matrix and measurement of crystal size: **(1)** size of 2.1 x 1.6 μm, **(2)** size of 2.0 x 1.4 μm, **(3)** size of 1.7 x 1.7 μm, **(4)** size of 3.0 x 2.0 μm and **(5)** size of 2.8 x 1.7 μm. Scale bar, 2 μm.

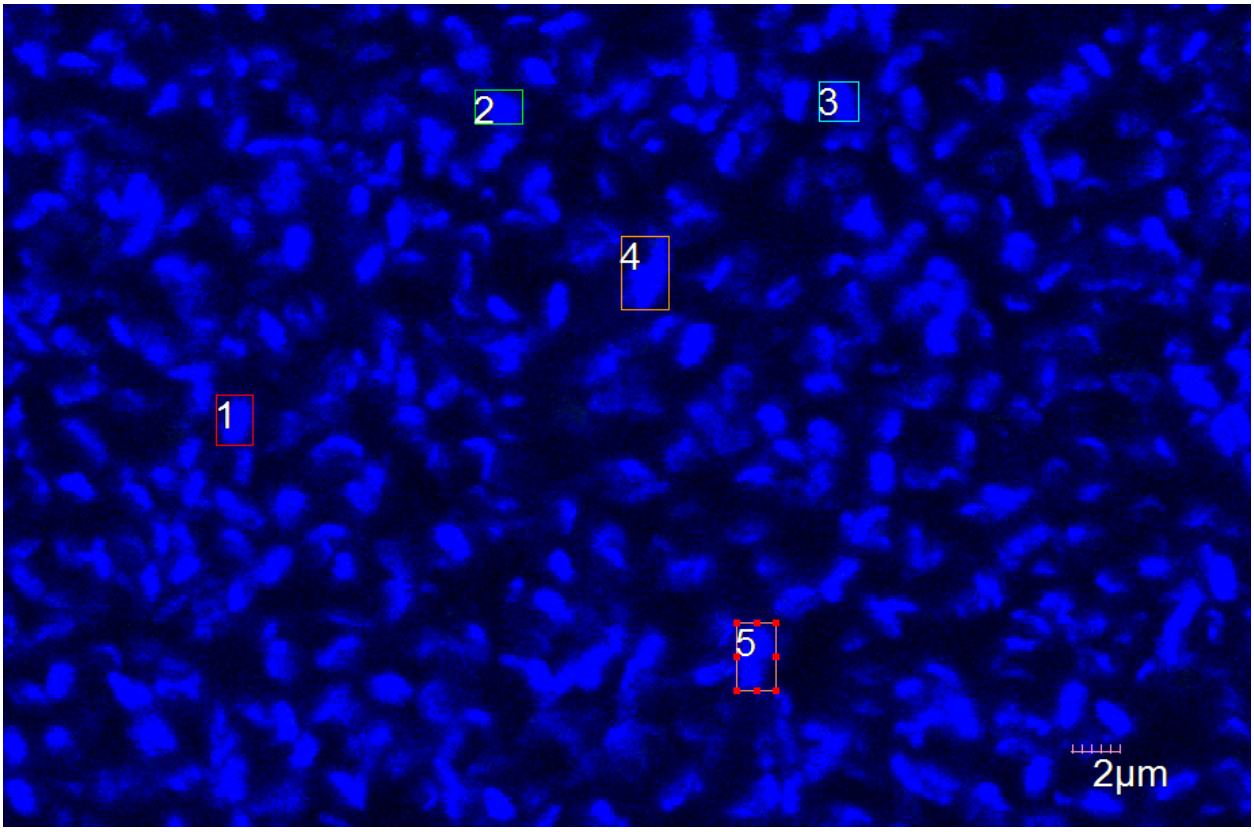
2
3
4
1
5
2μm

Figure 3. 6. MALDI-MS mass spectra of dorsal hippocampus in the positive ion mode of Intact, Citrisolv- and CLARITY-delipidated sections within mass range of m/z 100-350.

Analytes were notably enriched within the mass range m/z 350-900. Data for each hippocampus and condition represented the average of 1840 spectra collected from the selected region, by AP-MALDI, using ImageQuest imaging software. Shaded area indicated the signature of 2,5-DHB matrix ions.

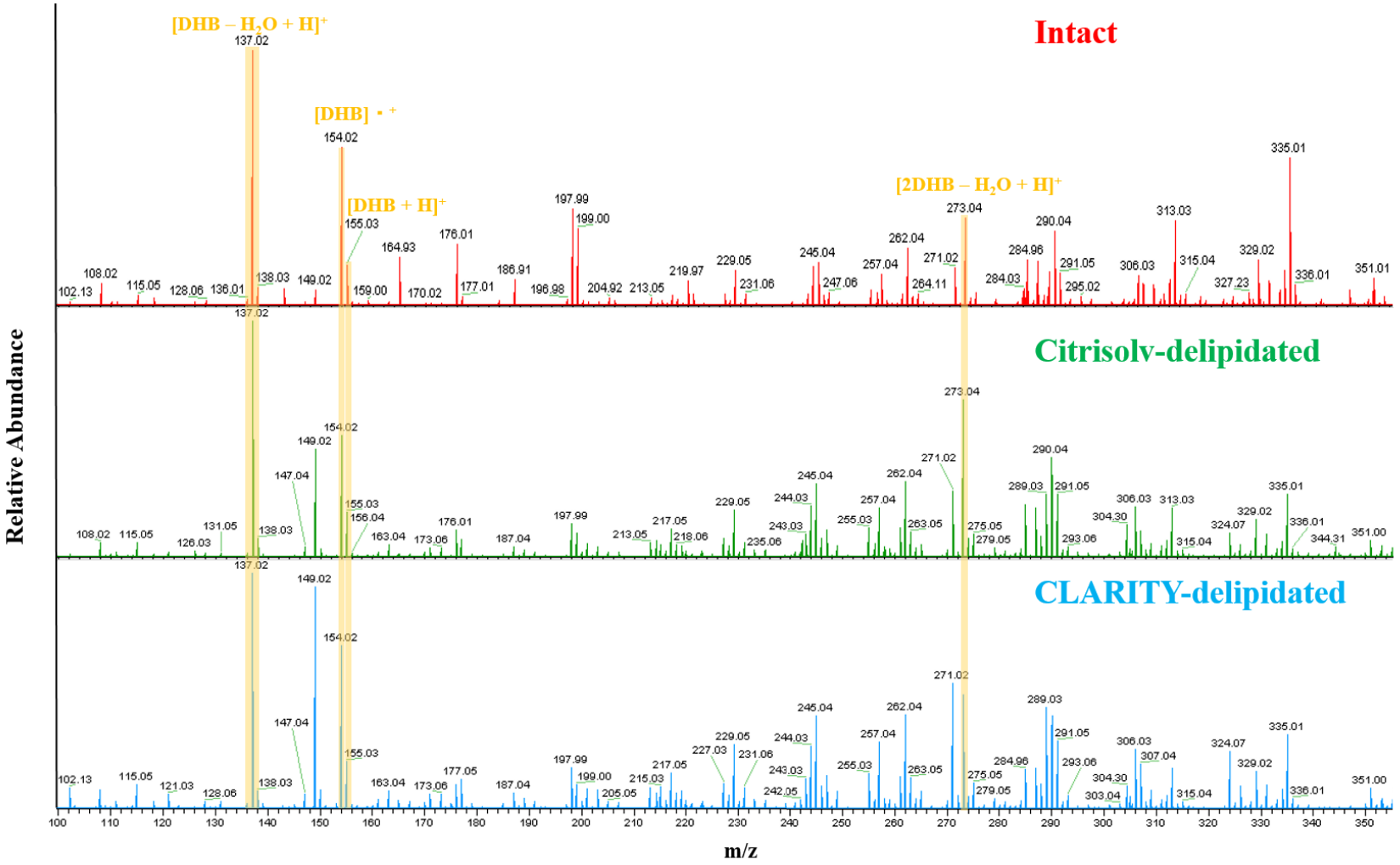
[DHB – H2O + H]+
[DHB] ▪ +
[DHB + H]+
[2DHB – H2O + H]+
Intact
Citrisolv-delipidated
CLARITY-delipidated
Relative Abundance
m/z

protonated ions or clusters of ions. The ion profiles of three samples in this mass range resemble each other strongly with similar abundance of matrix ions. Matrix ions were distinguished from tissue biomolecules by comparing the spectra with those from outside of the brain region. They were identified based on their exact m/z, corresponding to the 2,5-DHB matrix standard mass spectrum from MassBank[230] or in literature[231]. Within this mass range, all three samples display strong signals of 2,5-DHB matrix species, including m/z 136.0143 of $[DHB - H_2O]^+$, 137.0215 of $[DHB – H_2O + H]^+$, m/z 154.0240 of the radical $[DHB]^{\cdot+}$, m/z 155.0318 of the protonated $[DHB + H]^+$, m/z 173.0574 of $[DHB + H_2O + H_2]^+$, m/z 177.0134 of $[DHB + Na]^+$, m/z 273.0356 of the dimer $[2DHB – H_2O + H]^+$, m/z 290. 0385 of $[2DHB - H_2O]^+$, and m/z 291.0464 of $[2DHB - H_2O + H]^+$.

Within this same region, the nucleobase-derived metabolite, adenine, at m/z 136.0606 ± 1.5 ppm was also found at detectable amounts in all intact, Citrisolv-delipidated and CLARITY-delipidated sections as expected, since this molecule is not affected by the delipidation process (Figure 3.7A). This ion was identified by comparing its accurate mass to that reported in previous literature[232] and the Human Metabolome Database (HMDB)[233-235]. Another peak was detected nearby, at m/z 136.0143, and was identified as a derivative of DHB matrix. This ion appeared in all rastered areas, including regions outside of the brain section (Figure 3.7B). Figure 3.7C displays the mass range, m/z 136.0-136.1, in which high-resolution mass spectrometry (HRMS) was performed using the Orbitrap instrument to resolve the signal derived from the matrix (m/z 136.0143) and adenine (m/z 136.0606). This demonstrates the powerful ability of the Orbitrap mass analyzer to resolve species with proximal masses.

Figure 3. 7. MALDI-IMS distinguished adenine at m/z 136.0606 and DHB-matrix-derived-ion at m/z 136.0143 in Intact, Citrisolv- and CLARITY-delipidated brain slices.

MALDI-IMS distinguished two-closely matched ions, **A)** adenine at m/z 136.0606 as detected in Intact, Citrisolv-delipidated and CLARITY-delipidated slices. **B)** the 2,5-DHB-matrix-derived ion at m/z 136.0143 as detected in Intact, Citrisolv-delipidated and CLARITY-delipidated slices. **C)** showed the isolated spectral window in mass range m/z 136.0-136.1, resolved by HRMS Orbitrap mass spectrometer. Scale bar represents a heat map of ion counts.

A) Adenine: m/z 136.06058 ± 5 ppm

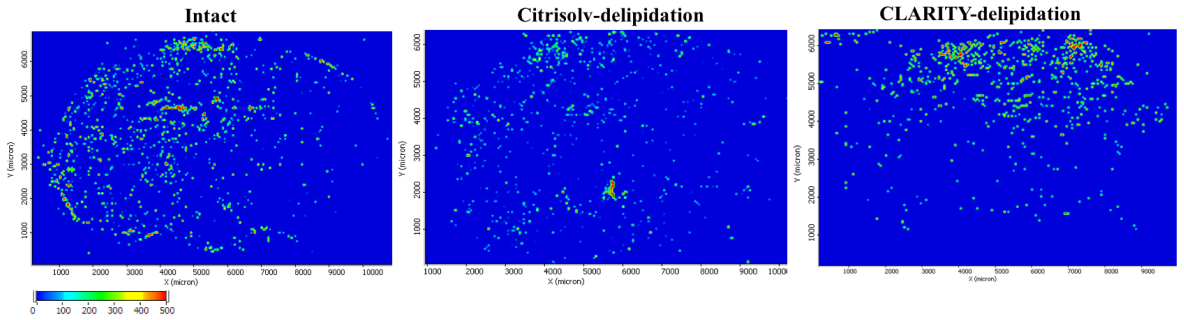

B) Matrix ion: m/z 136.01428 ± 5 ppm

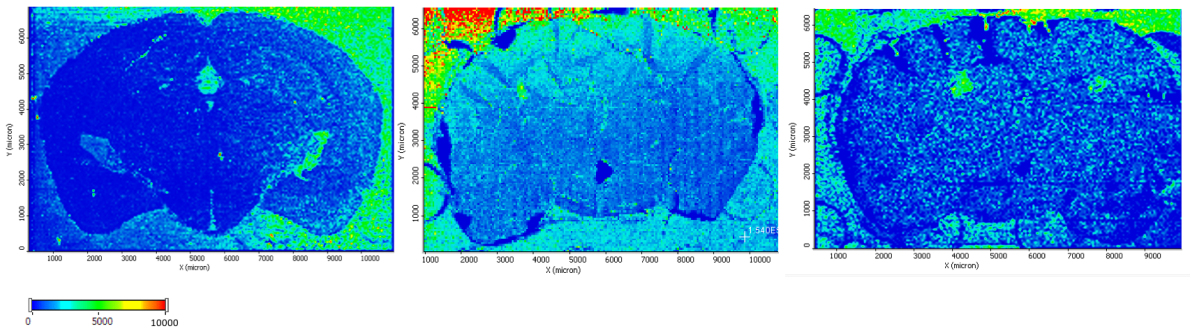

C) m/z 136.0 – 136.1 range resolved by HRMS

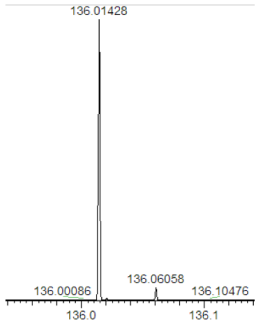

3.6.3. CLARITY-delipidation introduces hydrogel network into the MS spectra

Comparing the mass spectra of the three brain sections in the mass range m/z 400-900, the CLARITY-delipidated sections displayed *de novo* ions not detected in intact or Citrosolv-delipidated sections. These peaks were separated by increments of exactly 44 m/z (Figure 3.8). This observation reflects repeating units of ions indicative of concatenations of the structure, in other words, the presence of polymers[29]. Alternatively, a m/z difference of 44 between peaks is also commonly seen in mass spectra that is contaminated with polyethylene glycol (PEG) sources including triton-X present in the CLARITY delipidation buffer[236].

3.6.4. MALDI-IMS reveals 101 molecular ions absent from Citrisolv- and CLARITY-delipidated sections and thus bona fide lipid species

MALDI-IMS revealed different spectral profiles within the mass range of m/z 350-900 in intact brain sections compared to Citrisolv- and CLARITY-delipidated sections. By comparing the spectra and mass images obtained from the delipidated hippocampi (Citrisolv- and CLARITY-treated) to that of intact sections, it was possible to distinguish unambiguously lipid from non-lipid metabolites with the same m/z. We defined this level of validation as validation level 1. Signal intensity of every m/z in each of the brain sections was examined and compared to determine its presence or absence following both delipidiation protocols.

Within the mass range of m/z 350-900, cholesterol ions are found between m/z 350 to 400, while structural phospholipids and sphingolipids are usually found between m/z 700 and 850[123, 237]. Lipids found in intact brain section, validated by their absence in delipidated sections from the same animal, were then identified by querying their accurate mass given in both the LIPID MAPS[15] and VALID[238] databases. We defined this level of validation as validation level 2. Finally, a subset of species was subjected to tandem mass spectrometry (MALDI-MS/MS) characterization

Figure 3. 8. Mass spectrum and representative MALDI image of CLARITY-delipidated brain slice at m/z 600.48.

This ion was only found inside the brain, and in tissue slice treated CLARITY only. Ion intensity (count) on image was indicated by the corresponding scale bar.

A)

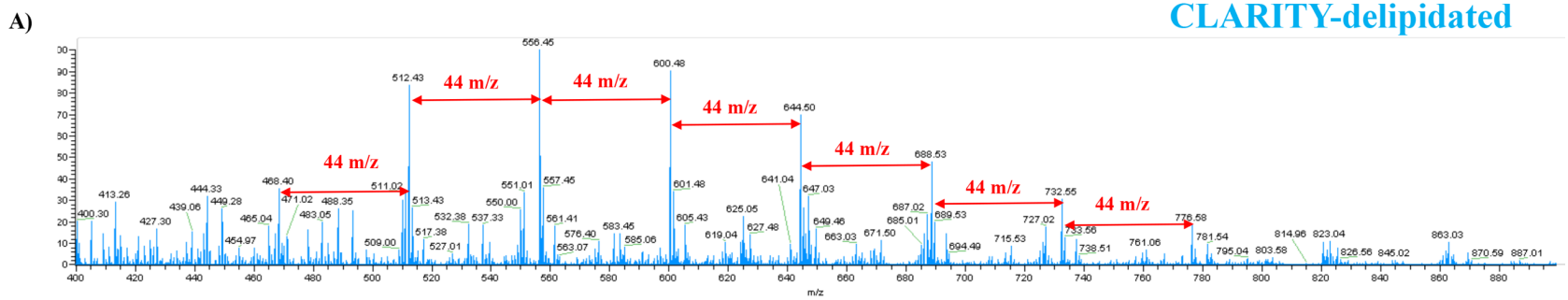
CLARITY-delipidated
44 m/z
44 m/z
44 m/z
44 m/z
44 m/z
44 m/z
m/z

B)

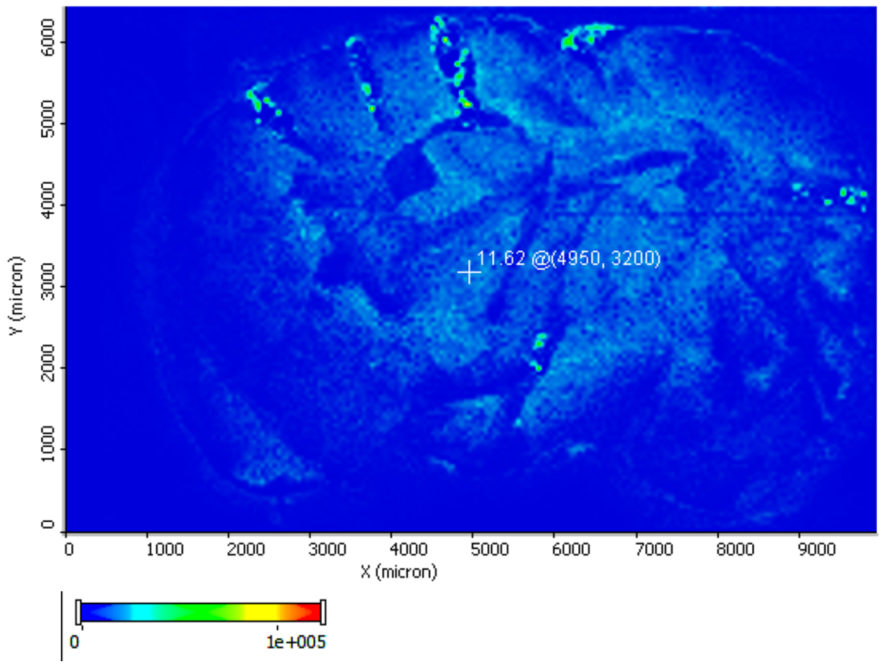
11.62 @(4950, 3200)
Y (micron)
X (micron)
0
1e+005

(validation level 3) to verify unambiguously the lipid identities predicted by high resolution mass accuracies (validation level 2) and established to be generated from bona fide lipids following delipidiation (validation level 1).

MALDI-IMS confirmed that the dehydrated form of cholesterol $[M - H_2O + H]^+$ at m/z 369.3485 was predominant across all regions in the brain (Figure 3.9A). Indeed, the signal at m/z 369.3485 is the base peak in all averaged spectra of intact brain sections. MS/MS experiment on this ion yielded a similar pattern to that found in literature[239], in which a cholesterol standard was used for fragmentation (Figure 3.9C). The deprotonated and positively-charged form of cholesterol $[M + H]^+$ at m/z 385.3433 was also found, although in much less abundance. Both are completely absent in the delipidated sections (Figure 3.9B). Hence, cholesterol was fully identified and validated (level 3).

Similarly, lipid ions found in the mass range m/z 400-900 underwent MS/MS experiment to validate their identities. In positive ion mode, characteristic product ions can be used to identify the lipid family of the parent ions. For example, GPCs and sphingomyelin fragmentation give rise to the same product ion at m/z 184.07, representing the phosphocholine head-group, while the common fragment of ceramides with a d18:1 sphingosine backbone is found at m/z 264.26. Protonated or sodiated forms of lipid ions can be determined by appearance of m/z 124.99 or 146.98 product ions, respectively, which corresponds to cyclic O,O'-dimethylenephosphate fragment with one H^+ or one Na^+ attached[124, 237]. Using this approach, it was possible to distinguish ions with very similar nominal masses. Examples of MS/MS experiment are depicted in Figure 3.10. By combining exact mass search and tandem mass spectrometry, 101 lipid molecular ions were found by comparing intact sections to the delipidated sections (level 1 validation, Table 3.1). Ten of these ions could not be validated further, while the rest were matched to 194 lipid species

Figure 3. 9. MALDI-IMS found cholesterol predominated in the Intact brain section but not in delipidated brain sections.

A) MALDI images of dehydrated cholesterol ion [Cholesterol - H_2O + H]$^+$ at m/z 369.3467 found only in Intact brain section and not in delipidated sections. Scale bar represents the ion counts as found and displayed in each image. **B)** Spectral data show cholesterol ions were found at m/z 369.35 and 385.34 in Intact section but not in the delipidated ones. **C)** MS/MS experiment of m/z 369.35 reveals similar patterns to that done by Paglia *et al* on cholesterol standard (Reprinted from Paglia et al, 2010 with permission from the Royal Society of Chemistry).

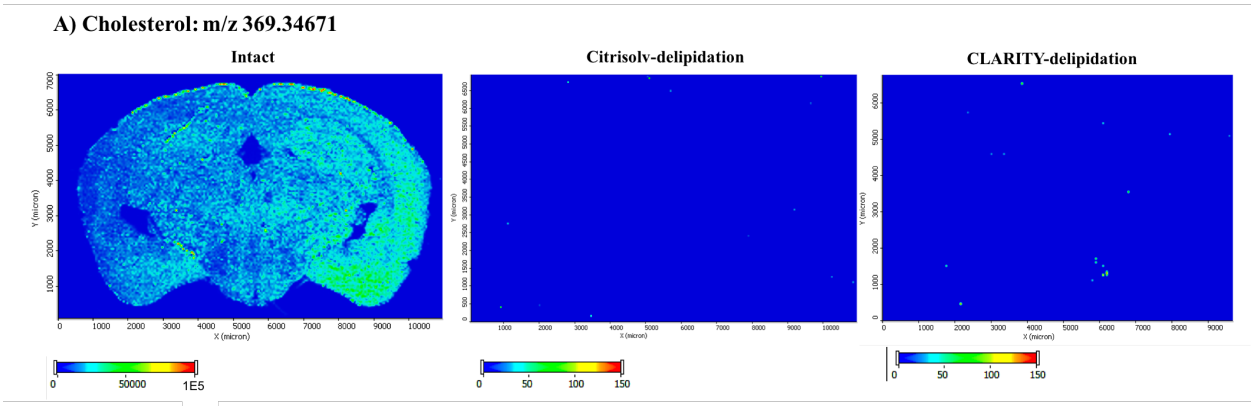
A) Cholesterol: m/z 369.34671
Intact
Citrisolv-delipidation
CLARITY-delipidation
X (micron)
Y (micron)
0
50000
1E5
50
100
150

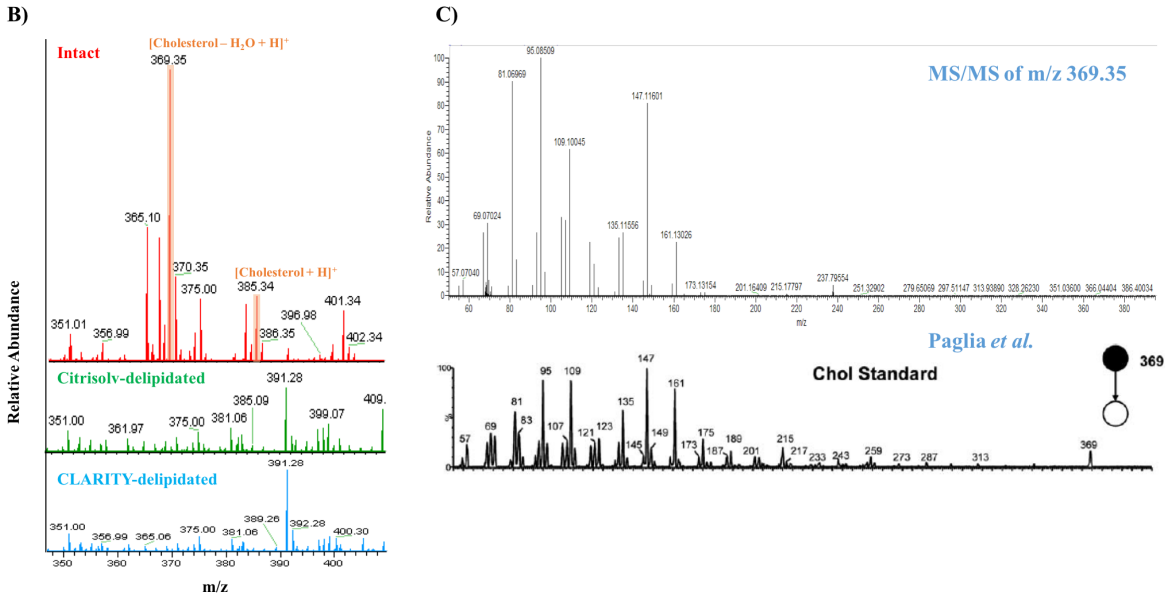
B)
C)
Intact
[Cholesterol – H2O + H]+
[Cholesterol + H]+
Citrisolv-delipidated
CLARITY-delipidated
Relative Abundance
m/z
MS/MS of m/z 369.35
Paglia et al.
Chol Standard

Figure 3. 10. MS/MS spectra of ceramide and phosphocholine-containing lipids (GPC or sphingomyelin).

MS/MS spectrum of three ions belong to different lipid classes from PB-brain slice. The product ion revealed the lipid class of each ion. A) MS/MS spectrum resulted to the only product ion at m/z 264.26, characteristic fragment of ceramide. B) MS/MS spectrum gave rise to most abundant fragment at m/z 184.07, the signature phosphocholine group of PCs or sphingomyelin. The presence of ion 124.99 was assigned to the protonated form of the cyclic O,O'-dimethylenephosphate fragment, indicating that the parent ion at m/z 734.56 was a protonated ion. C) MS/MS spectrum of m/z 810.59 yielded both m/z 184.07 and 264.26. This could be due to the co-presence of both a phospholipid and a ceramide with very close nominal mass to each other. The presence of both m/z 124.99 and m/z 146.98 (cyclic O,O'-dimethylenephosphate fragment) meant the fragmentation involved ions in both protonated and sodiated form.

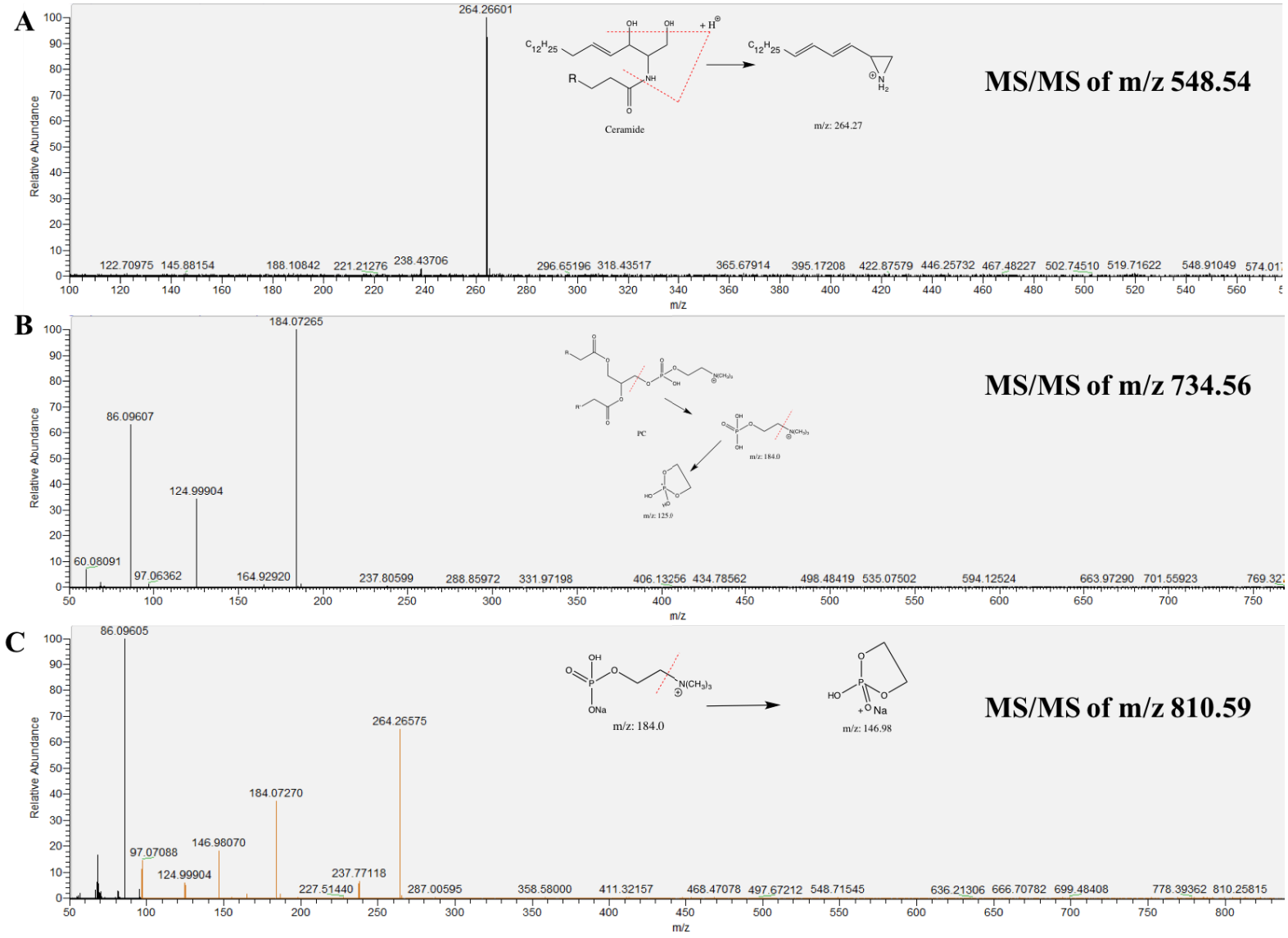
A
MS/MS of m/z 548.54
Ceramide
m/z: 264.27
B
MS/MS of m/z 734.56
PC
m/z: 184.0
m/z: 125.0
C
MS/MS of m/z 810.59
m/z: 184.0
m/z: 146.98
Relative Abundance
m/z

in the GPC, GPE, GPS, GPI, GPA, ceramides (Cers) and Cer subclasses, ceramide-1-phosphates (CerPs), phosphoinositol-ceramides (PI-Cers), lactosylceramides (LacCers), monohexosylceramides, combined glucosyl- and galactosyl-ceramides (HexCers), sulfatides (SHexCers), and sphingomyelins (SMs) based on accurate mass measurement (level 2 validation). Within these lipid ions, 53 underwent MS/MS for full validation (level 3 validation). Their characteristic product ions allowed their identities to be revealed and matched to 97 lipid species. This highlights the strength of combining MALDI-IMS and MS/MS in identifying and distinguishing isobars — lipid species with identical m/z and exact mass. Glycerophospholipid identities were also divided into the sub-classes based on the fatty acid-glycerol linkages at the *sn*-1 and *sn*-2 positions as defined in Chapter 1. In total, using MALDI-IMS and MS/MS, we found 74 GPC species (51 level 3 species and 23 level 2 species), 21 GPE species (level 2), 24 GPS species (level 2), 5 GPA species (level 2), 4 GPI species (level 2), 51 ceramide species (35 level 3 species and 16 level 2 species), 12 sphingomyelin species (10 level 3 species and 2 level 2 species) and 3 cholesterol species (1 level 3 species and 2 level 2 species).

All of the lipids found in intact brain sections with their corresponding validation levels are listed in Table 3.1. Representative images of GPCs, ceramides, sphingomyelins generated by MALDI-IMS are shown in Figure 3.11A, with a merged image of the distinctively localization of Cer(d33:0), SM(d36:1), and SM(d42:2) in Figure 3.11B.

3.7 DISCUSSION

We report here a new protocol to detect and visualize glycerophospholipids and sphingolipids in formalin-fixed mouse brain sections using MALDI-IMS. As proof of principle, we were able to identify 194 lipid species, including GPA, GPC, GPE, GPI, GPS, ceramides, and sphingomyelins

Figure 3. 11. Representative MALDI images of GPCs, ceramides, and sphingomyelin species found in PB brain section at bregma -2.00 mm.

(A) Representative MALDI images of GPCs, ceramides and sphingomyelin species found in PB brain section (bregma -2.00 mm). Scale bar represents the ion counts as found and displayed in each image (B) Merged image of Cer(d33:0) - Blue , SM(d36:1) – Red and SM(d42:2) – Green. Ion intensity (count) on image was indicated by the corresponding scale bar.

A

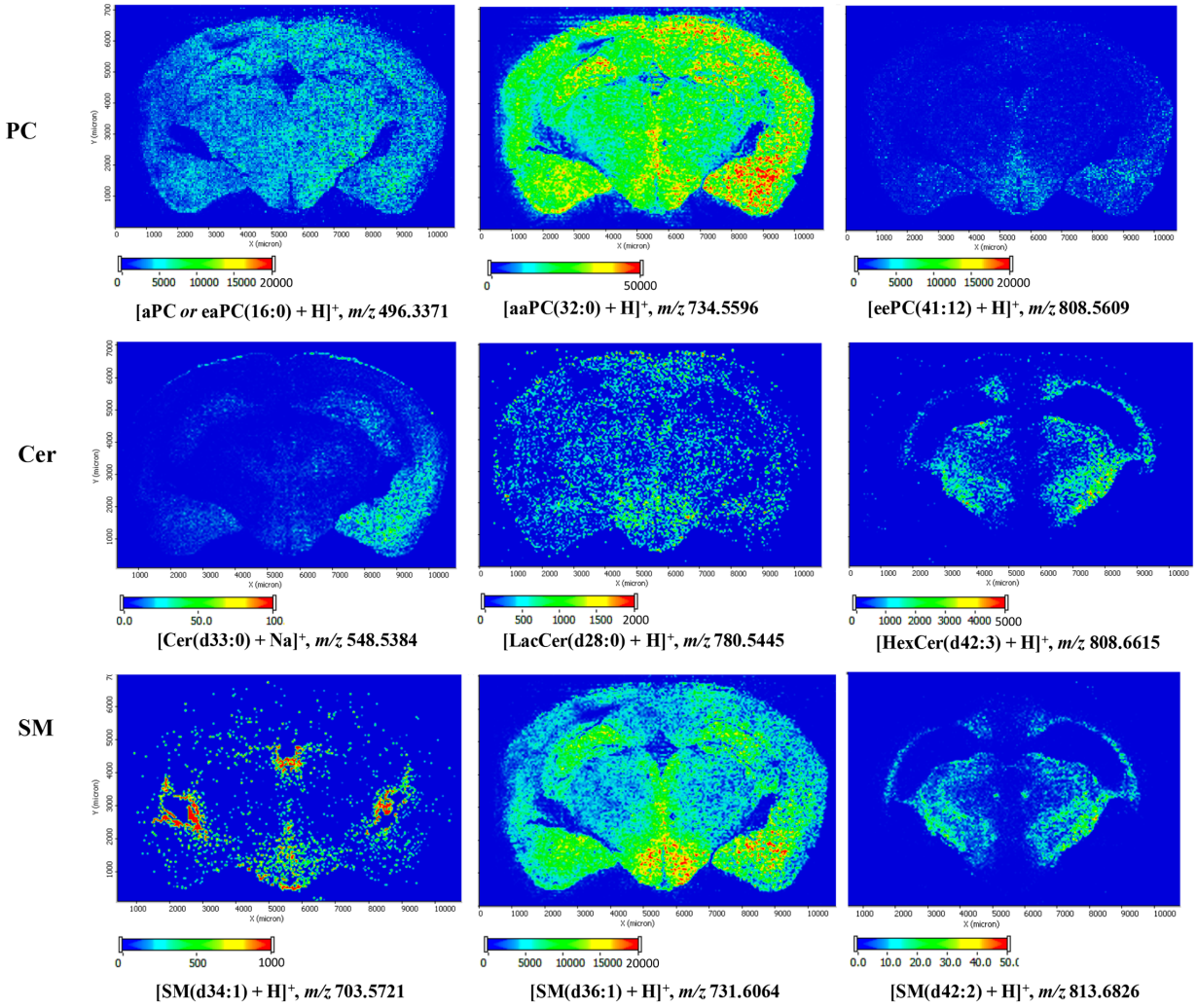
PC
Cer
SM
[aPC *or* eaPC(16:0) + H]+, *m/z* 496.3371
[aaPC(32:0) + H]+, *m/z* 734.5596
[eePC(41:12) + H]+, *m/z* 808.5609
[Cer(d33:0) + Na]+, *m/z* 548.5384
[LacCer(d28:0) + H]+, *m/z* 780.5445
[HexCer(d42:3) + H]+, *m/z* 808.6615
[SM(d34:1) + H]+, *m/z* 703.5721
[SM(d36:1) + H]+, *m/z* 731.6064
[SM(d42:2) + H]+, *m/z* 813.6826
Y (micron)
X (micron)

B

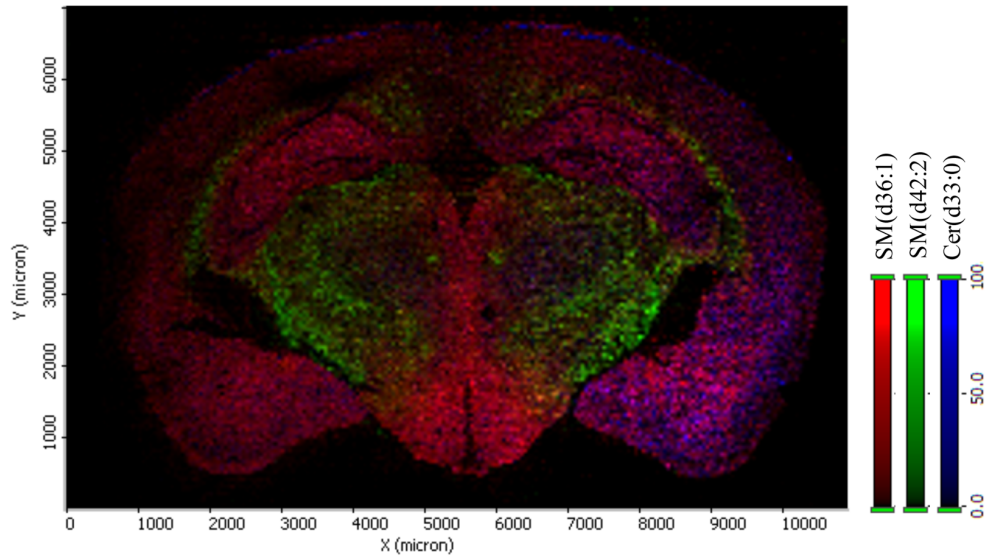
SM(d36:1)
SM(d42:2)
Cer(d33:0)
Y (micron)
X (micron)

in positive ion mode and validate their identities using exact mass measurements and MS/MS experiments.

3.7.1. Sublimation is an effective way to apply matrix on tissue for lipid imaging by MALDI.

Our method demonstrates the viability of sublimation as a mean to infuse matrix into brain tissue for lipid imaging while retaining morphology and tissue structure. The differences in matrix deposition methodologies was discussed extensively in Chapter 1. Here, we applied a novel sublimation method and verified this as a simple, cost-efficient, and effective way to introduce a uniform coat of 2,3-DHB matrix to brain sections. Optical and confocal microscopic quantification confirmed an even and finely dispersed surface of 2,3-DHB matrix after sublimation, consistent with previous reports of that random Brownian motion of gaseous molecules when transitioning from solid to vapor phase can be exploited to produce uniform matrices compatible with AP-MALDI IMS[82]. The visualization and measurement of matrix crystal size and its thickness allowed us to establish the amount of matrix required and the exact condition for reproducible sublimation. We determined that the optimized amount of 2,3-DHB matrix solids (~ 8 mg) produced a reproducible thickness (~ 8 μm) across experiments. Furthermore, we confirmed that this protocol produced crystal sizes significantly smaller than the laser spot size (90 x 45 μm), and thus sufficient for the imaging at a spatial resolution of 50 μm. It is essential that matrix crystal sizes are the same as or smaller than the laser diameter else matrix becomes the is limiting factor during laser rastering. Matrix crystals that are too large ablate pixel resolution at single laser spots, leading to a decrease in lateral resolution. Taken together, our data confirm that optimized sublimation is effective in matrix deposition and allow the generation of high-quality molecular images of lipid species.

TABLE 3.1 Cholesterol, glycerophosphocholines (GPC), glycerophosphoserine (GPS), ceramides (Cer) and sphingomyelins (SM) identified by MALDI-IMS directly from Intact mouse brain tissue. Lipid ions were identified ( ) by comparing Intact and delipidated slices. They were subsequently validated by exact mass search on LIPID MAPS database (partial-validated) and/or MALDI-MS/MS fragmentation (fully-validated).

m/z[a]	Identity[b]	Ion	delta m/z[c]	MS/MS[d]	Validation level[e]	Literature or Database
136.0606	Adenine	$[M + H]^+$	0.0061	-	■	(19), (20), (21), (22)
136.0143	DHB matrix ion	$[M - H_2O]^+$	0.0008	-	■	(18)
137.0215	DHB matrix ion	$[M - H_2O + H]^+$	-0.0012	-	■	(17), (18)
154.0240	DHB matrix ion	$[M]^{\cdot +}$	0.0054	-	■	(17), (18)
155.0318	DHB matrix ion	$[M + H]^+$	0.0077	-	■	(17), (18)
173.0574	DHB matrix ion	$[M + H_2O + H]^+$	0.0151	-	■	(18)
177.0134	DHB matrix ion	$[M + Na]^+$	-0.0004	-	■	(18)
273.0356	DHB matrix ion	$[2(M - H_2O) + H]^+$	-0.0004	-	■	(17)
290.0385	DHB matrix ion	$[2M-H_2O]^+$	0.0055	-	■	(18)
291.0464	DHB matrix ion	$[2M - H_2O + H]^+$	0.0054	-	■	(18)
369.3485	Cholesterol	$[M - OH]^+$	-0.00356	57.07, 69.07, 81.07, 95.08, 109.10, 131.12, 147.11, 161.13	■	(23), (35), (36), (37), (38)
385.3433	Cholesterol	$[M - H]^+$	-0.0036	-	■	(35), (36), (37), (38)
401.3360	Cholesterol (oxidative)	$[MO - H]^+$	-0.0057	-	■	(38), Hamilton (1998)
417.3341	-	-	-	-	■	
462.3407	GalSo(d18:1)	$[M + H]^+$	-0.0019	264.26, 282.92	■	(26); (28)
475.3542	-	-	-	282.92	■	
491.3490	-	-	-	-	■	
496.3371	LPC(16:0), PC(*O*-16:0)	$[M + H]^+$	-0.0032	184.07, 124.99	■	(26)
	PC(*O*-16:4); LPC(*O*-16:4); LPC(*P*-16:3)	$[M + Na]^+$	0.0567	146.97, 184.07	■	(26)
501.3336	-	-	-	-	■	
503.3492	-	-	-	-	■	
505.3608	*Lyso*SM(t18:0)	$[M + Na]^+$	0.02305	184.07, 146.98	■	(25)
515.3128	LPA(24:4); PA(*O*-24:4); PA(*P*-24:4)	$[M + H]^+$	-0.00042	-	■	(25), (26)
517.3286	LPA(24:3); PA(*O*-24:3); PA(*P*-24:3)	$[M + H]^+$	-0.0003	-	■	(25), (26)
	*Lyso*SM(d20:0)	$[M + Na]^+$	-0.0455	146.98, 184.07	■	(25)
519.3442	LPA(24:2); PA(*O*-24:2); PA(*P*-24:2)	$[M + H]^+$	-0.00027	146.98	■	(25), (26)
520.3461	LPC(18:2); PC(*O*-18:2), PC(*P*-18:1)	$[M + H]^+$	0.00577	184.07	■	(25)
521.3601	LPA(24:1); PA(*O*-24:1); PA(*P*-24:0)	$[M + H]^+$	-0.00011	-	■	(25), (26)

TABLE 3.1 (cont.)

522.3644	LPC(18:1); PC(*O*-18:1); PC(*P*-18:0)	$[M + H]^+$	0.00854	184	■	(25)
524.3646	PC(*O*-18:0); LPC(18:0)	$[M + H]^+$	-0.00703	-	■	(25)
	PE(*O*-21:0); LPE(21:0)	$[M + H]^+$	-0.00703	-	■	(25)
	CerP(t26:0)	$[M + H]^+$	-0.00653	-	■	(25)
536.3396	PC(18:1)	$[M + H]^+$	0.0044	-	■	(26)
	PE(21:1)	$[M + H]^+$	0.0044	-	■	(26)
	LPS(*O*-20:2); PS(*O*-20:2); LPS(*P*-20:1)	$[M + H]^+$	0.0044	-	■	(26)
537.3499	PA(24:0)	$[M + H]^+$	-0.0052	-	■	(25), (26)
538.3540	PC(18:0)	$[M + H]^+$	0.0031	-	■	(26)
	PE(21:0)	$[M + H]^+$	0.0031	-	■	(26)
	LPS(*O*-20:1); PS(*O*-20:1); PS(*P*-20:0)	$[M + H]^+$	0.0031	-	■	(25), (26)
546.3485	CerP(d29:2)	$[M + H]^+$	-0.04329	264.26	■	(25)
548.5385	Cer(d33:0)	$[M + Na]^+$	0.03732	124.99, 146.89, 264.26, 282.83	■	(25)
561.3469	-	-	-	-		
566.5460	Cer(d36:1)	$[M + H]^+$	-0.0047	264.26	■	(25)
620.5923	Cer(d40:2)	$[M + H]^+$	-0.0053	264.26, 282.28	■	
632.3478	PS(25:3)	$[M + H]^+$	-0.00846	-	■	(25), (26)
	PS(23:0)	$[M + Na]^+$	-0.00616	-	■	(25), (26)
648.6231	Cer(d42:2)	$[M + H]^+$	-0.0058	264.26	■	(25)
650.4300	LPS(27:1); PS(*O*-27:1); PS(*P*-27:0)	$[M + H]^+$	-0.00971	-	■	(25), (26)
670.3362	PC(29:11)	$[M + H]^+$	-0.01466	184	■	(25), (26)
	PC(27:8)	$[M + Na]^+$	-0.01226	184	■	(25), (26)
672.4155	PC(*O*-30:10); PC(*P*-30:9)	$[M + H]^+$	0.01259	184.07	■	(26)
	PC(*O*-28:7); PC(*P*-28:6)	$[M + Na]^+$	0.01499	146.98, 184.07	■	(26)
	PC(*O*-29:7)	$[M + Na]^+$	-0.02141	146.98, 184.07	■	(26)
678.4617	LPS(29:1); PS(*P*-29:0); PS(*O*-29:1)	$[M + H]^+$	-0.00927	-	■	(25), (26)
688.3524	PS(*O*-31:10); PS(*P*-31:9)	$[M + H]^+$	-0.00904	-	■	(26)
	PS(*O*-29:7); PS(*P*-29:6)	$[M + Na]^+$	-0.00674	-	■	(26)
700.4423	PC(*O*-32:10); PC(*P*-32:9)	$[M + H]^+$	0.00806	184.07	■	(26)
703.5721	SM(d34:1)	$[M + H]^+$	-0.0028	184.07	■	(25)
720.5474	PC(31:0)	$[M + H]^+$	-0.00688	124.94, 184.07	■	(25), (26)
725.5508	SM(d34:1)	$[M + Na]^+$	-0.00603	-	■	
	PE-Cer(d37:1)	$[M + Na]^+$	-0.00603	-	■	
731.6064	SM(d36:1)	$[M + H]^+$	0.0002	184.07, 124.99	■	(25)

TABLE 3.1 (cont.)

732.5488	PC(32:1)	$[M + H]^+$	-0.0055	-	■	(25), (26)
	PE(35:1)	$[M + H]^+$	-0.0055	-	■	(25), (26)
	PS(*O*-34:2)	$[M + H]^+$	-0.0055	-	■	(26)
734.5596	PC(32:0)	$[M + H]^+$	-0.0099	184.07, 124.99	■	(25), (26)
746.5696	PC(33:1)	$[M + H]^+$	-0.0004	-	■	(25), (26)
	PE(36:1)	$[M + H]^+$	-0.0004	-	■	(25), (26)
	PS(*O*-35:2)	$[M + H]^+$	-0.0004	-	■	(26)
746.5996	PC(*O*-34:1); PC(*P*-34:0)	$[M + H]^+$	-0.0067	-	■	(25), (26)
	PE(*O*-37:1); PE(*P*-37:0)	$[M + H]^+$	-0.0067	-	■	(25), (26)
	CerP(t42:1)	$[M + H]^+$	-0.0062	-	■	(25)
750.5799	PC(*O*-36:6)	$[M + H]^+$	-0.0002	-	■	(26)
	PE(*O*-39:6)	$[M + H]^+$	-0.0002	-	■	(26)
	PC(*O*-34:3)	$[M + Na]^+$	0.0021	-	■	(26)
	PE(*O*-37:3)	$[M + Na]^+$	0.0021	-	■	(26)
	CerP(d42:2)	$[M + Na]^+$	0.0027	-	■	(25)
	HexCer(d36:1)	$[M + Na]^+$	-0.0055	-	■	(25)
753.5817	SM(d36:1)	$[M + Na]^+$	-0.00638	146.98, 184.07	■	(25)
754.5389	PC(34:4)	$[M + H]^+$	0.0002	184.07	■	(25), (26)
756.5410	PC(*O*-37:10)	$[M + H]^+$	0.00775	-	■	(26)
	PE(*O*-40:10)	$[M + H]^+$	0.00775	-	■	(26)
	PC(*O*-35:7)	$[M + Na]^+$	0.01015	-	■	(26)
	PC(32:0)	$[M + Na]^+$	-0.01105	-	■	(25), (26)
758.5521	PC(*O*-37:9)	$[M + H]^+$	0.00332	-	■	(26)
	PE(*O*-40:9)	$[M + H]^+$	0.00332	-	■	(26)
	PC(*O*-35:6)	$[M + Na]^+$	0.00562	-	■	(26)
	PE(*O*-38:6)	$[M + Na]^+$	0.00562	-	■	(26)
759.6362	PE-Cer(d41:1)	$[M + H]^+$	-0.0013	-	■	(25)
	SM(d38:1)	$[M + H]^+$	-0.0013	-	■	(25)
760.5851	PC(34:1)	$[M + H]^+$	-0.0005	184, 124.99	■	(25), (26)
762.5914	PC(34:0)	$[M + H]^+$	-0.00989	184.07, 124.99	■	(25), (26)
766.5743	PC(*O*-36:5); PC(*P*-36:4)	$[M + H]^+$	-0.00019	184.07	■	(25), (26)
769.5486	SM(t36:1)	$[M + Na]^+$	-0.03439	184	■	(25)

TABLE 3.1 (cont.)

774.5497	PC(*O*-37:8); PC(*P*-37:7)	$[M + H]^+$	0.006	-		(26)
	PE(*O*-40:8); PE(*P*-40:7)	$[M + H]^+$	0.006	-		(26)
	PC(*O*-35:5); PC(*P*-35:4)	$[M + Na]^+$	0.0083	-		(26)
	PE(*O*-38:5); PE(*P*-38:4)	$[M + Na]^+$	0.0083	-		(25), (26)
774.6357	PC(*O*-36:1); PC(*P*-36:0)	$[M + H]^+$	-0.0019	-		(25), (26)
	PE(*O*-39:1); PE(*P*-39:0)	$[M + H]^+$	-0.0019	-		(25), (26)
	CerP(t44:1)	$[M + H]^+$	-0.0014	-		(25)
780.5445	LacCer(d28:0)	$[M + H]^+$	-0.00228	-		(25)
	PI-Cer(d34:1)	$[M + H]^+$	0.00592	-		
	PC(36:5)	$[M + H]^+$	-0.00978	-		(25), (26)
	PE(39:5)	$[M + H]^+$	-0.00978	-		
	PS(*O*-38:6)	$[M + H]^+$	-0.00978	-		(26)
	PC(34:2)	$[M + Na]^+$	-0.00748	-		(25), (26)
	PE(37:1)	$[M + Na]^+$	-0.00748	-		(25), (26)
	PS(*O*-36:3)	$[M + Na]^+$	-0.00748	-		(26)
782.5566	PC(*O*-39:11)	$[M + H]^+$	0.0078	124.99, 184.07		(26)
	PI-Cer(d34:0)	$[M + H]^+$	0.0024	264.26		(25)
	SHexCer(d34:0)	$[M + H]^+$	0.0119	264.26		(25)
	PC(*O*-37:8)	$[M + Na]^+$	0.0101	146.97, 184.07		(26)
	PC(34:1)	$[M + Na]^+$	-0.011	146.97, 184.07		(26)
782.6385	CerP(d46:3)	$[M + H]^+$	-0.0037	264.26		(25)
784.5681	PC(*O*-39:10)	$[M + H]^+$	0.00362	184.07		(26)
	PC(*O*-37:7)	$[M + Na]^+$	0.00602	146.98, 184.07		(26)
	PC(34:0)	$[M + Na]^+$	-0.01518	146.98, 184.07		
786.5893	PC(*O*-39:9)	$[M + H]^+$	0.0092	124.99, 184		(26)
787.6632	SM(d40:1)	$[M + H]^+$	-0.00565	184.07		(25)
	PE-Cer(d43:1)	$[M + H]^+$	-0.00565	-		
788.6060	PC(*O*-39:8)	$[M + H]^+$	0.01016	124.99, 184		(26)
	PC(36:1)	$[M + H]^+$	-0.01044	124.99, 184		(25), (26)
790.6191	PC(*O*-39:7)	$[M + H]^+$	0.00773	124.99, 184.07		(26)
792.6668	PC(*O*-37:3)	$[M + Na]^+$	0.04209	146.98, 184.07		(26)
796.6595	HexCer(d41:2)	$[M + H]^+$	-0.0066	264.3		(25)
800.6542	PC(*O*-38:2); PC(*P*-38:1)	$[M + H]^+$	0.0009	184.07		(25), (26)
	CerP(d47:1)	$[M + H]^+$	-0.0350	264.26		(25)
	HexCer(d41:0)	$[M + H]^+$	-0.0432	264.26		(25)

TABLE 3.1 (cont.)

802.6663	PC(*O*-38:1); PC(*P*-38:0)	$[M + H]^+$	-0.0026	-	■	(25), (26)
	PE(*O*-41:1); PE(*P*-41:0)	$[M + H]^+$	-0.0026	-	■	(25), (26)
	CerP(t46:1)	$[M + H]^+$	-0.0021	-	■	(25)
	HexCer(t40:0)	$[M + H]^+$	-0.0104	-	■	(25)
804.5445	LacCer(d30:2)	$[M + H]^+$	-0.0023	264.26	■	(25)
	PI-Cer(d36:3)	$[M + H]^+$	0.0059	264.26	■	(25)
	SHexCer(d36:3)	$[M + H]^+$	0.0155	264.26	■	(25)
	PC(38:7)	$[M + H]^+$	-0.0093	184.07	■	(25), (26)
	PC(*O*-39:11)	$[M + Na]^+$	0.0137	146.98, 184.07	■	(26)
	PC(36:4)	$[M + Na]^+$	-0.0069	146.98, 184.07	■	(25), (26)
806.5577	PC(38:6)	$[M + H]^+$	-0.01182	184.07	■	(25), (26)
	PI-Cer(d36:2)	$[M + H]^+$	0.00348	264.26	■	(25)
	LacCer(d30:1)	$[M + H]^+$	-0.00472	264.26	■	(25)
	PC(*O*-39:10)	$[M + Na]^+$	0.01118	146.98, 184.07	■	(26)
	PC(36:3)	$[M + Na]^+$	-0.00992	146.98, 184.07	■	(25), (26)
808.5609	PC(*O*-41:12)	$[M + H]^+$	-0.00365	184.07	■	(26)
	SHexCer(d36:1)	$[M + H]^+$	0.00055	264.26	■	(25)
	LacCer(d30:0)	$[M + H]^+$	-0.01725	264.26	■	(25)
808.6615	HexCer(d42:3)	$[M + H]^+$	-0.00461	264.26	■	(25)
	PI-Cer(d36:1)	$[M + H]^+$	0.09159	264.26	■	(25)
809.6492	SM(d40:1)	$[M + Na]^+$	-0.00154	184.07	■	(25)
810.5888	PC(*O*-41:11)	$[M + H]^+$	0.0087	124.99, 184.07	■	(26)
	PI-Cer(d36:0)	$[M + H]^+$	0.0033	264.26	■	(25)
	SHexCer(d36:0)	$[M + H]^+$	0.0128	264.26	■	(25)
	PC(*O*-39:8)	$[M + Na]^+$	0.011	146.98, 184.07	■	(26)
	PC(36:1)	$[M + Na]^+$	-0.0101	146.98, 184.07	■	(25), (26)
810.6745	PC(*O*-40:4)	$[M + H]^+$	0.0005	184.07	■	(26)
	GalCer(d18:1/24:1)	$[M + H]^+$	-0.0072	264.26	■	(25)
	PC(*O*-38:1)	$[M + Na]^+$	0.0028	146.98, 184.07	■	(26)
812.6874	PC(*O*-40:3)	$[M + H]^+$	-0.0023	184.07	■	(26)
	CerP(d48:2)	$[M + H]^+$	-0.0018	264.26	■	(25)
	HexCer(d42:1)	$[M + H]^+$	-0.0100	264.26	■	(25)
	PC(*O*-38:0)	$[M + Na]^+$	0.0000	146.98, 184.07	■	(26)

TABLE 3.1 (cont.)

813.6826	PE-Cer(d45:2)	$[M + H]^+$	-0.0018	282.73	■	(25)
	SM(d42:2)	$[M + H]^+$	-0.0018	124.80, 184.07	■	(25)
	SM(t39:0)	$[M + Na]^+$	0.037	146.98, 184.07	■	(25)
814.6712	PC(*O*-39:2); PC(*P*-39:1)	$[M + H]^+$	0.00232	184.07	■	(26)
816.6459	PC(38:1)	$[M + H]^+$	-0.0023	-	■	(25), (26)
	PE(41:1)	$[M + H]^+$	-0.0023	-	■	(25), (26)
	PS(*O*-40:2)	$[M + H]^+$	-0.0023	-	■	(26)
822.6360	LacCer(d31:0)	$[M + H]^+$	0.0423	264.26	■	(25)
826.6695	PC(*O*-40:3); PC(*P*-40:2)	$[M + H]^+$	0.0006	-	■	(25), (26)
	PE(*O*-43:3); PE(*P*-43:2)	$[M + H]^+$	0.0006	-	■	(25), (26)
	CerP(d49:2)	$[M + H]^+$	-0.0353	266.298	■	(25)
	HexCer(d43:1)	$[M + H]^+$	-0.0436	266.298	■	(25)
828.6846	PC(*O*-40:2); PC(*P*-40:1)	$[M + H]^+$	0.0000	184.07	■	(25), (26)
	CerP(d49:1)	$[M + H]^+$	-0.0359	282.28, 264.26	■	(25)
832.5721	PI-Cer(d38:3)	$[M + H]^+$	0.00218	-	■	(25)
	LacCer(d32:2)	$[M + H]^+$	-0.00602	-	■	(25)
	PC(40:7)	$[M + H]^+$	-0.01352	184.07	■	(25), (26)
834.5900	LacCer(d32:1)	$[M + H]^+$	-0.00367	-	■	(25)
	PI-Cer(d38:2)	$[M + H]^+$	0.00453	-	■	(25)
	PS(*O*-40:4)	$[M + Na]^+$	-0.00887	-	■	(26)
836.6515	PC(*O*-41:5); PC(*P*-41:4)	$[M + H]^+$	-0.0018	124.99, 184.07	■	(26)
842.6613	PC(40:2)	$[M + H]^+$	-0.0026	-	■	(25), (26)
	PE(43:2)	$[M + H]^+$	-0.0026	-	■	(25), (26)
	PS(*O*-42:3)	$[M + H]^+$	-0.0026	-	■	(26)
	PS(*O*-40:0)	$[M + Na]^+$	-0.0002	-	■	(26)
844.6774	PC(40:1)	$[M + H]^+$	-0.0021	-	■	(25), (26)
	PE(43:1)	$[M + H]^+$	-0.0021	-	■	(25), (26)
	PS(*O*-42:2)	$[M + H]^+$	-0.0021	-	■	(26)
848.6514	PC(*O*-42:6); PC(*P*-42:5)	$[M + H]^+$	-0.00189	184.07	■	(25), (26)
	LacCer(d33:1)	$[M + H]^+$	0.04201	282.28	■	(25)
	PI-Cer(d39:2)	$[M + H]^+$	0.05021	282.28	■	(25)
	PC(*P*-40:2); PC(*O*-40:3);	$[M + Na]^+$	0.00051	146.98, 184.07	■	(26)
850.6667	LacCer(d33:0)	$[M + H]^+$	0.0417	282.28	■	(25)
	PI-Cer(d39:1)	$[M + H]^+$	0.0499	282.28	■	(25)

TABLE 3.1 (cont.)

856.5674	PC(42:9)	$[M + H]^+$	-0.0182	184.07		(25), (26)
	PC(40:6)	$[M + Na]^+$	-0.0159	146.98, 184.07		(25), (26)
867.6149	-	-	-	146.98, 184.07		
870.5738	PC(43:9)	$[M + H]^+$	-0.0275	124.99, 184.07		(26)
886.5675	PS(44:9)	$[M + H]^+$	0.0077	-		(25), (26)
896.5893	PS(*O*-46:11); PS(*P*-46:10)	$[M + H]^+$	0.0088	-		(26)
912.5822	PS(46:10)	$[M + H]^+$	0.0073	-		(25), (26)
	PS(44:7)	$[M + Na]^+$	0.0091	-		(26)
925.616	PI(*O*-42:6); PI(*P*-42:5)	$[M + H]^+$	-0.0005	-		(25), (26)
	PI(*O*-40:3); PI(*P*-40:2)	$[M + Na]^+$	0.002	-		(25), (26)
929.5873	-	-	-	146.98, 184.07		
932.5473	PS(46:11)	$[M + Na]^+$	0.0061	146.98		(25), (26)
935.5682	PI(42:8)	$[M + H]^+$	0.0033	-		(25), (26)
	PI(40:5)	$[M + Na]^+$	0.0056	-		(25), (26)
940.6158	PS(48:10)	$[M + H]^+$	0.0091	-		(25), (26)
958.5637	PS(48:12)	$[M + Na]^+$	0.0063	146.98		(25), (26)
1072.5926	-	-	-	-		
1108.5481	-	-	-	-		
468.3997	Hydrogel network ion	$[M]^+$	-	-		
512.4255	Hydrogel network ion	$[M]^+$	-	-		
556.4512	Hydrogel network ion	$[M]^+$	-	-		
600.477	Hydrogel network ion	$[M]^+$	-	-		
644.5027	Hydrogel network ion	$[M]^+$	-	-		
688.5283	Hydrogel network ion	$[M]^+$	-	-		
732.5538	Hydrogel network ion	$[M]^+$	-	-		
776.5796	Hydrogel network ion	$[M]^+$	-	-		

[a] Molecular ions found in ■ all tissues (intact, Citrisolv- and CLARITY-delipidated), in ■ intact tissue only, and in ■ CLARITY-delipidated tissue only

[b] Acronyms: PC, PC(*O*), or PC(*P*) for diacyl-, alkyl ether-acyl or alkyl ether-akyl ether, or alkenyl ether-acyl glycerophosphocholine, respectively; LPC, LPC(*O*), LPC(*P*) corresponds to 1-acyl-*sn*-glycero-3-phosphocholine, 1-alkyl-*sn*-glycero-3-phosphocholine or 1-alkenyl-*sn*-glycero-3-phosphocholine. Where molecular identities are indicated, LPC(*P*-20:0) defines a molecular species belonging to the PC class lipids with a polar head group (PC) at the *sn*-3 position of the glycerol backbone, a hydrocarbon chain of 20 carbons with 0 double bonds at the *sn*-1 position via an vinyl ether linkage (P-), and a hydroxyl group at the sn-2 position (*lyso*).

[c] Δ m/z: Difference between observed m/z and actual m/z.

[d] Fragment ions observed following MS/MS analysis verifying identity.

[e] Validation level: Level 1(Not validated) *Bona* fide lipids detected in intact samples but absent from Clarity and Citrisolv-delipdated tissue; Hydrogel network detected Clarity tissue only; Level 2 (Partially-validated) Lipids identified by accurate mass search using the LIPID MAPS Structural Database and VaLID v3.0; *Bona* fide peptides detected in intact samples, Clarity, and Citrisolv-delipdated tissue and identified by accurate mass search using Human Metabolome Database; Sublimination matrix ions detected in sublimation layer and tissue and identified by literature; Level 3 (■ Fully Validated) Lipid identities confirmed by MALDI-MS/MS fragmentation.

3.7.2. Validation of AP-MALDI-IMS imaging of lipids in FF brain section

AP-MALDI_MS of m/z 100-350 profiles regions enriched in small metabolites, neurotransmitter peptides, and fatty acids. Some examples of non-lipid neural molecules expected to be present in abundance in this scan range are choline (theoretical m/z 104.1075), acetylcholine (m/z 146.1181), several amino acids such as glutamine (m/z 147.0691), lysine (m/z 147.1055), histidine (m/z 156.0695), carnitine (m/z 162.1052), and arginine (m/z 175.1117), nucleobase-derived metabolites such as adenine (m/z 136.0545), guanine (m/z 152.0494), adenosine-mono-phosphate (AMP) (m/z 348. 0631), and guanidine-mono-phosphate (GMP) (m/z 364.0579)[233-235]. These molecules are not expected to be affected by delipidation process and their presences in all tissues (intact and delipidated) can be used to confirm the utility of assignation in delipdated samples. Thus, we used this m/z range to verify that non-lipid metabolites are not lost following delipidation comparing with previous literature the abundances of small metabolites analysis by imaging mass spectrometry[232].

Surprisingly, among all metabolites that were examined, we found that only adenine was present in detectable amounts in intact FF tissue sections and, as expected, signal was not changed following delipidation. The lack of other metabolites and peptides could be due to the fact that all sections had been fixed chemically by formalin before mass spectrometric analysis. Fixation with formalin preserves the tissue integrity and cellular morphology via the formation of methylene cross-bridges between proteins, peptides and nucleic acids, owing to the presence of the amine groups. Fixed biomolecules, however, notably proteins and peptides, present a problem to MS analysis. Upon fixation, they resemble a complex, or a network, rather than individual molecules. This leads to difficulties in ionization and detection[151], posing challenges in detecting discrete metabolites. While we were able to detect multiple small metabolites in intact and delipidated brain sections, unlike adenine, these were present only in trace amounts. Previous studies with interests

in detecting and imaging small metabolites and neurotransmitters have exercised the use of flash frozen tissues and advised against using FF tissue[172, 232, 240]. Our analysis confirms this waring indicating that the presence of small metabolites and neurotransmitters in fixed tissues is complicated due to difficulties in ionization and their low concentration at physiological condition[240-242]. Excitingly, the robust lipid signals, verified by delipidation negative controls sustaining adenine in both intact and delipidated, provides converging evidence to indicate that FF tissue may be advantageous for lipidomic imaging studies as neural peptide ionization will be suppressed favouring enrichment and resolution of lipid imaging.

In support of this interpretation, formalin fixation did not affect the detection and visualization of lipids in intact brain section. We were able to detect cholesterol at high abundance, as well as other lipid species as listed in Table 3.1. Lipid species were only found in the intact brain sections and were completely absent in the delipidated brain sections (Citrisolv and CLARITY). Absence was defined as ion counts below limit of detection as assessed using ImageQuest (ThermoScientific). This was determined by examining the signal intensity of peaks at every m/z in each brain section (intact and both negative controls). For example, Figure 3.8A illustrated the image of the dehydrated form of cholesterol ion[243-246] at m/z 369.3467 (at bregma -2.00 mm) present in high abundance in the intact section (ion intensity of 10^5 ions, as displayed) and absent in the delipidated ones (completely absent in Citrisolv-delipidated slice and faintly present below 10^2 ion in CLARITY-delipidated sections).

We further show that the cost-effective, simple procedure of Citrosolv-delipidation is superior to the more labour-intensive CLARITY protocol. CLARITY introduced new ions into delipidated mass spectra used to validate lipid identities. These ions were defined by concatenations of m/z of 44 matching that of a primary amide ion in the backbone of peptides and proteins. One possible explanation for this observation is that these signals belong to biomolecules crosslinked to each

other and to the hydrogel polymers of CLARITY. An m/z difference of 44 is also indicative of the presence of PEG, including the triton-X present in the CLARITY delipidation buffer[236]. Despite best attempts to remove Triton-X following delipidation, recent reports indicate that even trace amounts of Triton-X are problematic for MALDI-IMS[236]. Thus, the signals that we observed in CLARITY slice may have also been due to the use of Triton-X in the CLARITY protocol (Figure 3.11).

All lipid ions were identified with high-resolution mass accuracy (≤ 5 ppm) with no detectable degradation of signal at a spatial resolution of 50 μm across the entire murine brain (coronal section), allowing for reliable localization. Multiple ions of the same nominal mass were distinguished by the characteristic high resolution of the Orbitrap mass analyzer and identities assigned for proximal lipids, with respect to m/z. These included the pair of ions at m/z 808.5609 and m/z 808.6615 which were distinctively identified as $[PC(O\text{-}41:12) + H]^+$ and $[HexCer(d42:3) + H]^+$, respectively, revealing different distributions in intact brain (Figure 3.10A). Other pairs of ions with similar nominal m/z included those at m/z 746.5696 and m/z 746.5996, m/z 774.5497 and m/z 774.6357, m/z 782.5566 and m/z 782.6385, and the pair at m/z 810.5888 and m/z 810.6745. The molecular ions in each pair were distinguished from each other and located by MALDI-IMS on the brain slices unambiguously by their accurate mass and their identities were determined with or without the assistance of MS/MS and listed in Table 3.1.

Validation levels were assigned to each lipid species identified in intact brain. Species present in intact but not delipidated sections were verified as lipids and assigned a level one validation. Ions verified at a level one assignation and matched to a lipid by high mass accuracy within a +/- 0.005 m/z difference were considered as partially validated and assigned a level two validation. Tandem mass spectrometry proved to be an invaluable tool in further validating structural identity.

The signature product ions produced from target lipid ions in the HCD cell facilitated determination and validation of the lipid identity at a level three validation. In this proof-of-principle study, we only performed a non-targeted data-dependent MS/MS experiment to test the efficiency of performing fragmentation directly from the tissue. It must be noted that not all lipid ions were successfully fragmented according to this protocol. Thus, in future studies, MS/MS will be optimized to target specific classes and subclasses of lipids unidentified in this study. Direct imaging of the signature fragments present in the tissue by MS/MS is also possible and will facilitate the visualization of particular lipid classes[247].

3.8 CONCLUSION

In this work, multiple approaches were combined to produce a working protocol for the analysis of lipids in FF brain tissue. AP-MALDI-IMS was used to determine the presence and location of lipids in coronal murine brain section. We show that the orbitrap mass analyzer of the Q-Exactive Plus mass spectrometer effectively identified lipid species based on their m/z using high-resolution mass accuracy. Finally, the presence of the higher-collision dissociation cell in the Q-Exactive Plus allowed an additional level of validation for the identity of lipid species via tandem mass spectrometry.

CHAPTER 4 - GENERAL DISCUSSION & CONCLUSION

4.1 SUMMARY OF FINDINGS

In this thesis, I utilized mass spectrometry to profile lipid metabolism post-mortem and assess localization in the brain. Data presented in this thesis identify fingerprints of GPC metabolic changes post-mortem indicative of a decrease in enzymatic activity associated with remodelling of PAF second messengers acutely following peri-mortem agonal respiration and early post-mortem anoxia followed by an increase in membrane metabolism at longer post-mortem intervals. Data presented in Chapter Two suggest that, for analyses of GPCs in post-mortem hippocampus, tissue harvested between 6 to 12 h after death can be combined to produce reproducible lipidomic analyses but that earlier post-mortem times <3 h should not be compared to tissue subjected to >3 h post-mortem interval. In Chapter Three, I elaborated the usefulness of mass spectrometry as a technology to further study lipids by visualization. Coupling an AP-MALDI source to an Orbitrap mass analyzer, I developed a method and protocol for IMS. This method was developed and optimized for GPC, Cer, and SM species, enhancing signals for and producing specific signature fragments of these lipids. This latter methodology will enable us to localize changes in lipid metabolism to sub-regions within given anatomical brain structures.

4.2 POST-MORTEM EFFECTS ON "OMIC" DISCOVERY

While this study represents, to my knowledge, the first post-mortem assessment of lipidomic changes, this research fits into a larger body of work focused on enabling researchers to appropriately match post-mortem tissue and ensure results are indicative of disease and not death-induced alterations. The useful information that RNA provides is directly derived from the genome makes it an invaluable source for post-mortem profiling. However, the fragility of RNA is a concern due its ability to self-attack that is inherent in its own structure (i.e., the hydrolysis reaction occurring between the 2'-hydroxyl group and the adjacent phosphodiester bond)[248]. In addition,

endogenous factors such as cellular RNAses and exogenous factors such as pH, presence of oxygen, metal ions, and water are also causes of RNA degradation. Studies on the stability and status of RNA in post-mortem tissues, from both human and non-human brain samples, are extensive. It has been reported that mRNA stability is variably affected during the agonal period by different factors, but remains relatively stable in post-mortem states[249]. This observation also correlates with brain acidosis, which occurs very quickly during the agonal stages and slows down after death[250]. Interestingly, there are conflicting reports on the post-mortem stability of total RNA in brain tissue. Some have found that global RNA level is stable over prolonged PMI and arrived at the conclusion that post-mortem tissues are still reliable for RNA profiling as long as agonal factors are minimized[174, 251-253]. Others have reported contradicting findings with loss of RNA integrity over post-mortem time[254]. A time-course study examining the effects post-mortem delays have on RNA subclasses such as mRNA and miRNA reveals that these RNAs do remain stable even up to 48-96 hours post-mortem in rat brain[255]. Nevertheless, it appears that there are variations in the stability of RNAs globally and specifically; it is the selection of tissues with similar pre-mortem influences and minimizing agonal factors that will result in the most reliable profiling of data. On the contrary, post-mortem degradation of brain proteins has been found to produce different patterns, with some still exhibiting high expression even days after death (up to 72 hours)[255], while others did not change their expression until 48 hours post-mortem[256]. Consequently, it has been suggested that post-mortem stability of proteins is species-specific where one may be degraded at a different rate and with different patterns than another given the same post-mortem factor[257]. Similarly, I found that there are variations in post-mortem disruptions to the GPC lipidome. Sub-family such as LPC showed global increase; however, certain species showed a decrease during the first-hour post-mortem and then increase while a couple of others specifically decreased during the entire course of PMI. On the contrary, PC(*O*) PAF showed great

fluctuations in its metabolism after-death. More than 50% of the detected PAF species showed no change due to post-mortem delay, the remaining species showed the most fluctuations within the first hour post-mortem. Some increases were observed to start at 3-hour post-mortem and these seemed to favor the species with a higher number of unsaturation in their *sn-1* fatty acyl chain. Changes in PAF species in post-mortem brain tissue did not seem to be due to a stimulated remodelling of their immediate precursor *lyso*-PAF (LPC(*O*)) because there was no significant disruption found in this sub-family. The *lyso*-plasmalogen PC metabolites also exhibit species-specific disruption in which increase in LPC(*P*-16:0/0:0) led to a three-fold increase in the overall abundance of LPC(*P*) content while the rest showed a significant decrease. Hence, my observation dictates that lipids, specifically GPC as being studied in this thesis, are vulnerable to post-mortem delay. Certain species, such as most of the detected LPCs and some of the PAFs, may be collected between 6 and 12 hours, if not immediately after death, where their changes are minimal. Altogether, the results of this study are 1) first to examine the effects post-mortem delays have on the lipidome, and 2) highlight the importance of collecting tissue samples at the time when their lipidome are least disrupted due to post-mortem delays.

4.3 MALDI-IMAGING MASS SPECTROMETRY AS A LIPIDOMIC APPROACH

The methodology for lipid imaging *in situ* expands on previous work. Previous IMS studies have been based mainly on the popular platform of vacuum-MALDI coupled to a TOF mass spectrometer, since 1997[142-144, 146, 148] during the early days of MALDI-imaging up until recently[258-261]. While this method is very robust and well-documented, it has limitations. As discussed in Chapter One, vacuum-MALDI encounters the challenge of in-source decay which may complicate the mass spectrum and produce high background noise. The work in Chapter Three of this thesis explores the utility of AP-MALDI source with added PDF technology for improved electron emission and reduced S/N. I also showed that it was possible and beneficial to couple a source

such as AP-MALDI to an Orbitrap mass analyzer due to its ease to install without compromising the vacuum environment of the instrument and to handle tissue samples for IMS work. Utilizing the AP-MALDI-Orbitrap platform, I developed an IMS protocol in which high spatial resolution (50 μm), high mass resolution and accuracy and tandem mass spectrometry were combined for the characterization and localization of phospholipids and sphingolipids in mouse brain. Few studies have explored the advantages of this platform[262-263]. Coupling MALDI to TOF originally answered the quest for analyzing intact, large biomolecules such as polypeptide or proteins of thousands to tens of thousands Dalton. A TOF mass analyzer is known for its extremely large mass range, hence, traditionally, it was not necessary to look for a tandem-mass-spectrometry option in an MALDI-TOF apparatus. Tandem-mass-spectrometry, on the other hand, is extremely useful for the identification of lipids due to the signature fragments that are associated with certain lipid families (discussed in Chapter One and Three). Thus, the work presented here highlighted the extremely robust performance of AP-MALDI-Orbitrap IMS as a lipidomic approach.

In this thesis, I also took advantage of sublimation, a less popular but more cost-efficient and simpler approach than the commonly-utilized robotic sprayer[23, 264], to perform matrix application on brain tissue for MALDI-IMS. I found that sublimation, as a dry method is compatible for the localization analysis of lipids, as suggested by Hankins[82]. The main limitation of the sublimation method is the time it takes for one process of matrix coating (slower than a robotic sprayer); however, the matrix layer that this method produces is uniform and sufficient for lipid analysis on brain tissue, as confirmed by microscopy in Chapter Three.

Finally, it is to my knowledge that it is the first time, an *in situ* delipidation process was carried out and used as a negative control for a mass-spectrometry-based lipid identification approach. All other previous MALDI-IMS work relied on lipid signal enrichment by the matrix, high mass accuracy and/or fragmentation for assigning peaks as belonging to lipids and not another

biomolecule class. I utilized the commonly-used histology method of clearing lipids with xylene, a hydrophobic reagent to dissolve most lipids from fixed brain slices. This method showed to be useful as it effectively removed the majority of lipids while still retained non-lipid metabolites on brain tissue such as adenine. By comparing between delipidated and non-delipidated (intact) brain slices, lipids were identified and further validated by their exact mass and fragmentation patterns by mass spectrometry. Altogether, these steps helped to confirm the reliability of the IMS methodology developed.

4.4 COMBINING MS METHODOLOGIES IS ESSENTIAL TO REALIZE THE POTENTIAL OF A LIPIDOMIC APPROACH

No MS methodology provides all of the information necessary to explore the impact of lipid abnormalities in neurodegenerative diseases. In Chapter Two of this thesis, the separation ability of LC and technology of triple-quadrupole MS were combined to target, identify and quantify individual lipid species within the GPC lipid class. This character of LC-ESI-MS/MS is powerful, since it allows for: 1) the separation of different lipid classes and isobaric lipid species with identical m/z, and 2) the relative quantification of each of these targeted lipid species. However, the necessity to extract lipid species to enable separation destroys all spatial information of lipid distribution. This limitation was the motivation for the work presented in Chapter Three, in which a MALDI-IMS protocol was developed and optimized on an AP-MALDI-Orbitrap MS platform. The technique proved to be extremely useful in retaining the distribution information of different lipid species occupying different regions in the brain at the same time. The protocol developed in Chapter Three of this thesis has also shown to effectively identify different lipid classes simultaneously, and with the imaging ability of MALDI, it was able to show the different locations of individual species.

The findings and methods developed in this thesis showcase the power of mass spectrometry-based lipidomic approaches and open new avenues to lipidomic analysis. I look forward to applying the IMS methodology developed in Chapter Three to further explain the findings in Chapter Two for a better understanding of the post-mortem disruption to the lipidome. This will aid in deducing any delocalization effects that are associated with the changes in GPC levels. In addition, as I have shown that the developed IMS method was also fit for detecting and identifying other lipid classes such as SM, Cers and other phospholipid sub-classes such as PS, PE, PI, it will be possible to examine post-mortem disruptions in a broader range of the lipidome. Future work that will further the IMS methodology such as a normalization program will be useful for the removal of 1) background noises and interferences that affect signal intensity on the tissue slice, and 2) systematic errors to only reveal biological variations in the generated images. Current operating programs of the Orbitrap mass analyzer are not effective in performing proper normalization for IMS data. Improving this shortcoming would allow the powers of AP-MALDI-Orbitrap platform to be fully exploited when applying it to compare tissue sections which represent different physiological or pathological states. In the context of this thesis, it will allow me to fully explore the post-mortem lipidome, qualitatively and quantitatively, by incorporating multiple different methods. Since the dawn of MALDI mass spectrometry, its use for aboslute quantification has always been a controversial topic[265]. The main reason lies in the ambiguous nature of MALDI ionization mechanism. The reproducibility of each laser shot is not guaranteed[266]. Previous and current efforts that have been spent on quantification by imaging mass spectrometry admitted the fundamental challenges posed by MALDI[267-269]. While it is not the focus of this Master's thesis or my future directions to focus on constructing an absolute quantification method for MALDI-IMS, it is important for MALDI-IMS methods and protocols to contain a stringent processing and normalization step, so that biologically-relevant information

from the molecular images can be revealed and fully appreciated, and comparable with other mass-spectrometry quantification approaches in lipidomics.

REFERENCES

1. Pond, C. M., The Fats of Life. *Cambridge, UK: Cambridge Univ. Press* **1998**, 26.

2. Vance, D. E.; Vance, J., Biochemistry of Lipids, Lipoproteins, and. **1991**.

3. Voet, D.; Voet, J. G., Biochemistry. **2010**.

4. Mouritsen, O. G.; Bagatolli, L. A., Life - as a matter of fat: Lipids in a membrane biophysics perspective (2nd Edition). **2016**.

5. Kennedy, E. P., Metabolism and Function of Membrane Lipids. *Klin Wochenschr* **1987,** *65*, 205-212.

6. Peretó, J.; López-García, P.; Moreira, D., Ancestral lipid biosynthesis and early membrane evolution. *Trends in Biochemical Sciences* **2004,** *29*, 469-477.

7. IUPAC-IUB Commission on Biochemical Nomenclature - The Nomenclature of Lipids. *Journal of Biological Chemistry* **1967,** *242*, 4845-4849.

8. Nomenclature, I.-I. C. o. B., The Nomenclature of Lipids. *Biochem. J.* **1978,** *171*, 21-35.

9. Hauser, H.; Poupart, G., Lipid Structure. In *The Structure of Biological Membranes*, Second ed.; Yeagle, P. L., Ed. CRC Press LLC: Boca Raton, FL, 2005; pp 1-52.

10. Farooqui, A. A., Glycerophospholipids. **2014**.

11. Shevchenko, A.; Simons, K., Lipidomics: coming to grips with lipid diversity. *Nat Rev Mol Cell Biol* **2010,** *11* (8), 593-8.

12. Xu, H.; Valenzuela, N.; Fai, S.; Figeys, D.; Bennett, S. A. L., Targeted lipidomics - Advances in profiling lysophosphocholine and platelet-activating factor second messengers. *FEBS Journal* **2013,** *280*, 5652-5667.

13. Farooqui, A. A., Glycerophospholipids. In *eLS*, John Wiley & Sons, Ltd: Chichester, 2014.

14. Melnikova, V.; Bar-Eli, M., Inflammation and melanoma growth and metastasis: the role of platelet-activating factor (PAF) and its receptor. *Cancer Metastasis Rev.* **2007,** *26*, 359-371.

15. Fahy, E.; Cotter, D.; Sud, M.; Subramaniam, S., Lipid classification, structures and tools. *Biochimica et Biophysica Acta - Molecular and Cell Biology of Lipids* **2011,** *1811*, 637-647.

16. Fernandis, A. Z.; Wenk, M. R., Membrane lipids as signaling molecules. *Current opinion in lipidology* **2007,** *18*, 121-128.

17. Bennett, S. A. L.; Valenzuela, N.; Xu, H.; Franko, B.; Fai, S.; Figeys, D., Using neurolipidomics to identify phospholipid mediators of synaptic (dys)function in Alzheimer's Disease. *Frontiers in Physiology* **2013,** *4 JUL*, 1-16.

18. Müller, C. P.; Reichel, M.; Mühle, C.; Rhein, C.; Gulbins, E.; Kornhuber, J., Brain membrane lipids in major depression and anxiety disorders. *Biochimica et Biophysica Acta (BBA) - Molecular and Cell Biology of Lipids* **2015,** *1851*, 1052-1065.

19. Barburina, I.; Jackowski, S., Cellular responses to excess phospholipid. *The Journal of biological chemistry* **1999,** *274*, 9400-9408.

20. Klein, J., Membrane breakdown in acute and chronic neurodegeneration: Focus on choline-containing phospholipids. *Journal of Neural Transmission* **2000,** *107*, 1027-1063.

21. Farooqui, A. A.; Horrocks, L. A., Phospholipid Metabolism in Brain. In *Glycerophospholipids in the Brain: Phospholipases A2 in Neurological Disorders*, Springer Science & Business Media: New York, 2007; pp 1-23.

22. Mulder, M.; Ravid, R.; Swaab, D. F.; de Kloet, E. R.; Haasdijk, E. D.; Julk, J.; van der Boom, J. J.; Havekes, L. M., Reduced levels of cholesterol, phospholipids, and fatty acids in cerebrospinal fluid of Alzheimer disease patients are not related to apolipoprotein E4. *Alzheimer Dis Assoc Disord* **1998,** *12*, 198-203.

23. Shimma, S.; Sugiura, Y., Effective Sample Preparations in Imaging Mass Spectrometry. *Mass Spectrom (Tokyo)* **2014,** *3* (Spec Issue), S0029.

24. Pettegrew, J. W.; Panchalingam, K.; Hamilton, R. L.; Mcclure, R. J., Brain membrane phospholipid alterations in Alzheimer's disease. *Neurochemical research* **2001,** *26*, 771-782.

25. Nitsch, R. M.; Blusztajn, J. K.; Pittas, A. G.; Slack, B. E.; Growdon, J. H.; Wurtman, R. J., Evidence for a membrane defect in Alzheimer disease brain. *Proceedings of the National Academy of Sciences of the United States of America* **1992,** *89*, 1671-5.

26. Lands, W. E. M., Stories about acyl chains. *Biochimica et Biophysica Acta - Molecular and Cell Biology of Lipids* **2000,** *1483*, 1-14.

27. Gwak, G.-Y.; Yoon, J.-H., Lysophosphatidylcholine. In *Encyclopedia of Cancer*, Schwab, M., Ed. Springer Berlin Heidelberg: Heidelberg, 2012; Vol. 1, pp 2127-2128.

28. Fuller, N.; Rand, R. P., The influence of lysolipids on the spontaneous curvature and bending elasticity of phospholipid membranes. *Biophys J.* **2001,** *81*, 243-254.

29. Chernomordik, L.; Chanturiya, A.; J., G.; Zimmerberg, J., The hemifusion intermediate and its conversion to complete fusion: regulation by membrane composition. *Biophys J.* **1995,** *69*, 922-929.

30. Poole, A. R.; Howell, J. I.; Lucy, J. A., Lysolecithin and cell fusion. *Nature* **1970,** *227*, 810-814.

31. Oishi, K.; Raynor, R. L.; Charp, P. A.; Kuo, J. F., Regulation of protein kinase C by lysophospholipids. *J. Biol. Chem.* **1988,** *263*, 6865-6871.

32. Yuan, Y.; Schoenwaelder, S. M.; Salem, H. H.; Jackson, S. P., The bioactive phospholipid, lysophosphatidylcholine, induces cellular effects via G-protein-dependent activation of adenylyl cyclase. *J. Biol. Chem.* **1996,** *271*, 27090-27098.

33. Bernoud, N.; Fenart, L.; Moliere, P.; Dehouck, M. P.; Lagarde, M.; Cecchelli, R.; Lecerf, J., Preferential transfer of 2-docosahexaenoyl-1-lysophosphatidylcholine through an in vitro blood-brain barrier over unesterified docosahexaenoic acid. *J. Neurochem.* **1999,** *72*, 338-345.

34. Farooqui, A. A.; Horrocks, L. A., Lyso-Glycerophospholipids. In *Glycerophospholipids in the Brain: Phospholipases A2 in Neurological Disorders*, Springer: New York, USA, 2007; pp 199-218.

35. Birgbauer, E.; Rao, T. S.; Webb, M., Lysolecithin induces demyelination in vitro in a cerebellar slice culture system. *J. Neurosci. Res.* **2004,** *78*, 157-166.

36. Das, S.; Castillo, C.; Stevens, T., Phospholipid remodeling/generation in Giardia: The role of the Lands cycle. *Trends in Parasitology* **2001,** *17*, 316-319.

37. Richmond, G. S.; Smith, T. K., Phospholipases A 1. *International Journal of Molecular Sciences* **2011,** *12*, 588-612.

38. Bogatcheva, N. V.; Sergeeva, M. G.; Dudek, S. M.; Verin, A. D., Arachidonic acid cascade in endothelial pathobiology. *Microvasc Res* **2005,** *69* (3), 107-27.

39. MacDonald, J. I.; Sprecher, H., Phospholipid fatty acid remodeling in mammalian cells. *Biochim Biophys Acta* **1991,** *1084* (2), 105-21.

40. Hishikawa, D.; Shindou, H.; Kobayashi, S.; Nakanishi, H.; Taguchi, R.; Shimizu, T., Discovery of a lysophospholipid acyltransferase family essential for membrane asymmetry and diversity. *Proceedings of the National Academy of Sciences* **2008,** *105* (8), 2830-2835.

41. Chen, X.; Hyatt, B. A.; Mucenski, M. L.; Mason, R. J.; Shannon, J. M., Identification and characterization of a lysophosphatidylcholine acyltransferase in alveolar type II cells. *Proceedings of the National Academy of Sciences of the United States of America* **2006,** *103* (31), 11724-9.

42. Shindou, H.; Hishikawa, D.; Nakanishi, H.; Harayama, T.; Ishii, S.; Taguchi, R.; Shimizu, T., A single enzyme catalyzes both platelet-activating factor production and membrane biogenesis of inflammatory cells. Cloning and characterization of acetyl-CoA:LYSO-PAF acetyltransferase. *The Journal of biological chemistry* **2007,** *282* (9), 6532-9.

43. Zhao, Y.; Chen, Y. Q.; Bonacci, T. M.; Bredt, D. S.; Li, S.; Bensch, W. R.; Moller, D. E.; Kowala, M.; Konrad, R. J.; Cao, G., Identification and characterization of a major liver lysophosphatidylcholine acyltransferase. *The Journal of biological chemistry* **2008,** *283* (13), 8258-65.

44. Nakanishi, H.; Shindou, H.; Hishikawa, D.; Harayama, T.; Ogasawara, R.; Suwabe, A.; Taguchi, R.; Shimizu, T., Cloning and Characterization of Mouse Lung-type Acyl-CoA:Lysophosphatidylcholine Acyltransferase 1 (LPCAT1): EXPRESSION IN ALVEOLAR TYPE II CELLS AND POSSIBLE INVOLVEMENT IN SURFACTANT PRODUCTION. *Journal of Biological Chemistry* **2006,** *281* (29), 20140-20147.

45. Prescott, S. M.; Zimmerman, G. A.; Stafforini, D. M.; McIntyre, T. M., Platelet-activating factor and reated lipid mediators. *Annu. Rev. Biochem.* **2000,** *69*, 419-45.

46. Baker, R. R., Lipid acetylation reactions and the metabolism of platelet-activating factor. *Neurochemical research* **2000,** *25* (5), 677-83.

47. Arai, H., Platelet-activating factor acetylhydrolase. *Prostaglandins & Other Lipid Mediators* **2002,** *68–69*, 83-94.

48. McIntyre, T. M.; Prescott, S. M.; Stafforini, D. M., The emerging roles of PAF acetylhydrolase. *Journal of Lipid Research* **2009,** *50* (Suppl), S255-S259.

49. Yamashita, A.; Sugiura, T.; Waku, K., Acyltransferases and transacylases involved in fatty acid remodeling of phospholipids and metabolism of bioactive lipids in mammalian cells. *J. Biochem. (Tokyo)* **1997,** *122*, 1-16.

50. Lands, W. E., The enzymatic acylation of lysolecithin. *J. Biol. Chem.* **1960,** *235*, 2233-2237.

51. Reinhold, S. L.; Zimmerman, G. A.; Prescott, S. M.; McIntyre, T. M., Phospholipid remodeling in human neutrophils. Parallel activation of a deacylation/reacylation cycle and platelet-activating factor synthesis. *J. Biol. Chem.* **1989,** *264*, 21652-21659.

52. Fenn, J. B.; Mann, M.; Meng, C. K.; Wong, S. F.; Whitehouse, C. M., Electrospray ionization-principles and practice. *Mass Spectrometry Reviews* **1990,** *9*, 37-70.

53. Karas, M.; Bachmann, D.; Bahr, U.; Hillenkamp, F., Matrix-assisted ultraviolet laser desorption of non-volatile compounds. *International Journal of Mass Spectrometry and Ion Processes* **1987,** *78*, 53-68.

54. de Hoffmann, E.; Stroobant, V., Formation and Fragmentation of Ions: Basic Rules. In *Mass Spectrometry: Principles and Applications*, Third ed.; John Wiley & Sons, Ltd: West Sussex, England, 2013; pp 76-80.

55. Tan, P. V.; Laiko, V. V.; Doroshenko, V. M., Atmospheric Pressure MALDI with Pulsed Dynamic Focusing for High-Efficiency Transmission of Ions into a Mass Spectrometer. *Analytical Chemistry* **2004,** *76*, 2462-2469.

56. Li, L.; Han, J.; Wang, Z.; Liu, J. a.; Wei, J.; Xiong, S.; Zhao, Z., Mass spectrometry methodology in lipid analysis. *International Journal of Molecular Sciences* **2014,** *15*, 10492-10507.

57. Vaz, F. M.; Pras-Raves, M.; Bootsma, A. H.; van Kampen, A. H. C., Principles and practice of lipidomics. *Journal of Inherited Metabolic Disease* **2014,** *38*, 41-52.

58. Kebarle, P.; Tang, L., From ions in solution to inos in the gas phase. *Analytical chemistry* **1993,** *65*, 972A-986A.

59. de Hoffmann, E.; Stroobant, V., Electrospray. In *Mass Spectrometry: Principles and Applications*, Third ed.; John Wiley & Sons, Ltd: West Sussex, England, 2013; pp 43-46.

60. Gomez, A.; Tang, K., Charge and fission of droplets in electrostatic sprays. *Physics of Fluids* **1994,** *6* (1), 404-414.

61. Mann, M., Electrospray: Its potential and limitations as an ionization method for biomolecules. *Organic Mass Spectrometry* **1990,** *25*, 575-587.

62. Dole, M., Molecular Beams of Macroions. *The Journal of Chemical Physics* **1968,** *49* (5), 2240.

63. Iribarne, J. V., On the evaporation of small ions from charged droplets. *The Journal of Chemical Physics* **1976,** *64* (6), 2287.

64. Pulfer, M.; Murphy, R. C., Electrospray mass spectrometry of phospholipids. *Mass Spectrometry Reviews* **2003,** *22*, 332-364.

65. Han, X.; Gross, R. W., Shotgun lipidomics: Electrospray ionization mass spectrometric analysis and quantitation of cellular lipidomes directly from crude extracts of biological samples. *Mass Spectrometry Reviews* **2005,** *24*, 367-412.

66. Ejsing, C. S.; Ekroos, K.; Jackson, S.; Duchslav, E.; Hao, Z.; Pelt, C. K. v.; Simins, K.; Shevchenko, A., Shotgun lipidomics: High throughput profiling of the molecular composition of phospholipids. *ASMS Abstract Archives* **2004**, 25.

67. Han, X., Mass spectrometry-based lipidomics approaches. In *Lipidomics: Comprehensive Mass Spectrometry of Lipids*, 1st ed.; John Wiley & Sons, Inc.: 2016; pp 53-87.

68. Han, X.; Gross, R. W., Electrospray ionization mass spectroscopic analysis of human erythrocyte plasma membrane phospholipids. *Proceedings of the National Academy of Sciences of the United States of America* **1994,** *91*, 10635-10639.

69. Brugger, B.; Erben, G.; Sandhoff, R.; Wieland, F. T.; Lehmann, W. D., Quantitative analysis of biological membrane lipids at the low picomole level by nano-electrospray ionization tandem mass spectrometry. *Proc. Natl. Acad. Sci. USA* **1997,** *94*, 2339-2344.

70. Han, X., Lipidomics: Comprehensive Mass Spectrometry of Lipids. **2016**, 466.

71. Harris, D. C., High-performance liquid chromatography. In *Quantitative Chemical Analysis*, Seventh Ed ed.; W.H.Freeman and Company: New York, USA, 2007; pp 556-570.

72. Moldoveanu, S.; David, V., Essentials in Modern HPLC Separations. **2013**.

73. Tsui, F. C.; Ojcius, D. M.; Hubbell, W. L., The intrinsic pKa values for phosphatidylserine and phosphatidylethanolamine in phosphatidylcholine host bilayers. *Biophysical Journal* **1986,** *49*, 459-468.

74. Marsh, D., Handbook of lipid bilayers. **2013**, 1174.

75. Marvin, L. F.; Roberts, M. A.; Fay, L. B., Matrix-assisted laser desorption/ionization time-of-flight mass spectrometry in clinical chemistry. *Clinica Chimica Acta* **2003,** *337*, 11-21.

76. Gross, J. H., *Mass spectrometry*. 2nd ed.; Springer-Verlag Berlin Heidelberg: Heidelberg, 2011; p 773.

77. Dreisewerd, K., The desorption process in MALDI. *Chemical Reviews* **2003,** *103*, 395-425.

78. Medina, N.; Huth-Fehre, T.; Westman, A.; Sundqvist, B. U. R., Matrix-assisted Laser Desorption: Dependence of the Threshold Fluence on Analyte Concentration. *Organic Mass Spectrometry* **1994,** *29*, 207-209.

79. Fuchs, B.; Schiller, J., Application of MALDI-TOF mass spectrometry in lipidomics. *European Journal of Lipid Science and Technology* **2009,** *111*, 83-98.

80. de Hoffmann, E.; Stroobant, V., Matrix-Assisted Laser Desorption Ionization. In *Mass Spectrometry: Principles and Applications*, Third ed.; John Wiley & Sons, Ltd: West Sussex, England, 2013; pp 33-41.

81. Schiller, J.; Arnhold, J.; Benard, S.; Müller, M.; Reichl, S.; Arnold, K., Lipid analysis by matrix-assisted laser desorption and ionization mass spectrometry: A methodological approach. *Analytical Biochemistry* **1999,** *267*, 46-56.

82. Hankin, J. A.; Barkley, R. M.; Murphy, R. C., Sublimation as a Method of Matrix Application for Mass Spectrometric Imaging. *J Am Soc Mass Spectrom.* **2007,** *18*, 1646-1652.

83. Schiller, J.; Fuchs, B., Lipids. In *MALDI MS: A Practical Guide to Instrumentation, Methods and Applications*, Second Edi ed.; Hillenkamp, F.; Peter-Katalinic, J., Eds. Wiley-VCH Verlag GmbH & Co. KGaA.: 2014; pp 273-311.

84. Fuchs, B.; Suss, R.; Schiller, J., An update of MALDI-TOF mass spectrometry in lipid research. *Prog Lipid Res* **2010,** *49* (4), 450-75.

85. Cramer, R., Advances in MALDI and Laser-Induced Soft Ionization Mass. **2016**, 287.

86. Harvey, D. J., Matrix-assisted Laser Desorption / Ionization Mass Spectrometry of Phospholipids. *Journal of Mass Spectrometry* **1995,** *30*, 1333-1346.

87. Thomas, A.; Charbonneau, J. L.; Fournaise, E.; Chaurand, P., Sublimation of new matrix candidates for high spatial resolution imaging mass spectrometry of lipids: Enhanced information in both positive and negative polarities after 1,5-diaminonapthalene deposition. *Analytical Chemistry* **2012,** *84*, 2048-2054.

88. Cerruti, C. D.; Benabdellah, F.; Laprevote, O.; Touboul, D.; Brunelle, A., MALDI imaging and structural analysis of rat brain lipid negative ions with 9-aminoacridine matrix. *Anal Chem* **2012,** *84* (5), 2164-71.

89. Steven, R. T.; Bunch, J., Repeat MALDI MS imaging of a single tissue section using multiple matrices and tissue washes. *Anal Bioanal Chem* **2013,** *405* (14), 4719-28.

90. Ye, H.; Gemperline, E.; Venkateshwaran, M.; Chen, R.; Delaux, P.-M.; Howes-Podoll, M.; Ané, J.-M.; Li, L., MALDI mass spectrometry-assisted molecular imaging of metabolites during nitrogen fixation in the Medicago truncatula–Sinorhizobium meliloti symbiosis. *The Plant Journal* **2013,** *75* (1), 130-145.

91. Guo, S.; Wang, Y.; Zhou, D.; Li, Z., Significantly increased monounsaturated lipids relative to polyunsaturated lipids in six types of cancer microenvironment are observed by mass spectrometry imaging. *Scientific Reports* **2014,** *4*, 5959.

92. Hillenkamp, F.; Jaskolla, T. W.; Karas, M., The MALDI Process and Method. *Maldi Ms* **2014**, 2-40.

93. Mowry, C. D.; Johnston, M. W., Simultaneous detection of ions and neutrals produced by matrix-assisted laser desorption. *Rapid communications in mass spectrometry : RCM* **1993,** *7*, 569-575.

94. Quist, A. P.; Huth-Fehre, T.; Sundqvist, B. U. R., Total yield measurements in matrix-assisted laser desorption using a quartz crystal microbalance. *Rapid communications in mass spectrometry : RCM* **1994,** *8*, 149-154.

95. Knochenmuss, R.; Dubois, F.; Dale, M. J.; Zenobi, R., The matrix suppression effect and ionization mechanisms in matrix-assisted laser desorption/ionization. *Rapid communications in mass spectrometry : RCM* **1996,** *10*, 871-877.

96. Knochenmuss, R., Ion formation mechanisms in UV-MALDI. *Analyst* **2006,** *131* (9), 966-86.

97. Knochenmuss, R.; Zenobi, R., MALDI Ionization: The Role of In-Plume Processes. *Chemical Reviews* **2002,** *103*, 441-452.

98. Zenobi, R.; Knochenmuss, R., Ion formation in MALDI mass spectrometry. *Mass Spectrome. Rev.* **1998,** *17*, 337-366.

99. Ehring, H.; Karas, M.; Hillenkamp, F., Role of photoionization and photochemistry in ionization processes or organic molecules and relevance for matrix-assisted laser desorption/ionization mass spectrometry. *Org. Mass Spectrom.* **1992,** *27*, 472-480.

100. Karas, M.; Glückmann, M.; Schäfer, J., Ionization in matrix-assisted laser desorption/ionization: Singly charged molecular ions are the lucky survivors. *Journal of Mass Spectrometry* **2000,** *35*, 1-12.

101. Lehmann, E.; Knochenmuss, R.; Zenobi, R., Ionization mechanisms in matrix-assisted laser desorption/ionization mass spectrometry: contribution of preformed ions. *Rapid Commun. Mass Spectrom.* **1997,** *11*, 1483-1492.

102. Jaskolla, T. W.; Karas, M.; Roth, U.; Steinert, K.; Menzel, C.; Reihs, K., Comparison Between Vacuum Sublimed Matrices and Conventional Dried Droplet Preparation in MALDI-TOF Mass Spectrometry. *Journal of the American Society for Mass Spectrometry* **2009,** *20*, 1104-1114.

103. O'Connor, P. B.; Dreisewerd, K.; Strupat, K.; Hillenkamp, F., MALDI Mass Spectrometry Instrumentation. In *MALDI MS: A Practical Guide to Instrumentation, Methods and Applications*, Hillenkamp, F.; Peter-Katalinic, J., Eds. Wiley-VCH Verlag GmbH & Co. KGaA.: Weinheim, 2007; pp 41-104.

104. Laiko, V. V.; Baldwin, M. A.; Burlingame, A. L., Atmospheric pressure matrix-assisted laser desorption/ionization mass spectrometry. *Analytical chemistry* **2000,** *72*, 652-657.

105. Paul, v. W.; Stenwedel, H., Ein neues Massenspektrometer ohne Magnetfeld. *Z. Naturforschg* **1953,** *8a*, 448-450.

106. de Hoffmann, E.; Stroobant, V., Quadrupole Analysers. In *Mass Spectrometry: Principles and Applications*, Third ed.; John Wiley & Sons, Ltd: West Sussex, England, 2013; pp 88-99.

107. Duckworth, H. E.; Barber, R. C.; Venkatasubramanian, V. S., Mass Spectrometry. **1990**, 354.

108. Paul, W.; Hans-Peter, R., Bonn; Heinz Frohlich, E., Method of separating ions of different specific charges. **1958**.

109. Uthe, P. M. Quadrupole mass analyzer. September 13, 1965, 1969.

110. Makarov, A., Electrostatic axially harmonic orbital trapping: A high-performance technique of mass analysis. *Analytical Chemistry* **2000,** *72*, 1156-1162.

111. Kingdon, K. H., A Method for the Neutralization of Electron Space Charge by Positive Ionization at Very Low Gas Pressures. *Physical Review* **1923,** *21* (4), 408-418.

112. Knight, R. D., Storage of ions from laser-produced plasmas. *Applied Physics Letters* **1981,** *38* (4), 221.

113. Oksman, P., A Fourier transform time-of-flight mass spectrometer. A SIMION calculation approach. *International Journal of Mass Spectrometry and Ion Processes* **1995,** *141*, 67-76.

114. Perry, R. H.; Cooks, R. G.; Noll, R., J., Orbitrap mass spectrometry: instrumentation, ion motion and applications. *Mass Spectrometry Reviews* **2008,** *27*, 661-699.

115. Gillig, K. J.; Bluhm, B. K.; Russell, D. H., Ion motion in a Fourier transform ion cyclotron resonance wire ion guide cell. *International Journal of Mass Spectrometry and Ion Processes* **1996,** *157-158*, 129-147.

116. Makarov, A.; Denisov, E.; Lange, O., Performance evaluation of a high-field Orbitrap mass analyzer. *J Am Soc Mass Spectrom* **2009,** *20* (8), 1391-6.

117. de Hoffmann, E.; Stroobant, V., The 2D Ion Trap. In *Mass Spectrometry: Principles and Applications*, Third ed.; John Wiley & Sons, Ltd: West Sussex, England, 2013; pp 117-121.

118. Makarov, A.; Denisov, E.; Kholomeev, A.; Balschun, W.; Lange, O.; Strupat, K.; Horning, S., Performance evaluation of a hybrid linear ion trap/orbitrap mass spectrometer. *Analytical Chemistry* **2006,** *78*, 2113-2120.

119. Makarov, A.; Denisov, E.; Lange, O.; Horning, S., Dynamic range of mass accuracy in LTQ Orbitrap hybrid mass spectrometer. *J Am Soc Mass Spectrom* **2006,** *17* (7), 977-82.

120. Kalli, A.; Smith, G. T.; Sweredoski, M. J.; Hess, S., Evaluation and Optimization of Mass Spectrometric Settings during Data-Dependent Acquisition Mode: Focus on LTQ- Orbitrap Mass Analyzers. *J Proteome Res.* **2013,** *12*, 3071-3086.

121. Schwartz, J. C.; Kovtoun, V. V., Automatic gain control (AGC) method for an ion trap and a temporarilly non-uniform ion beam. **2011**.

122. Köfeler, H. C.; Fauland, A.; Rechberger, G. N.; Trötzmüller, M., Mass Spectrometry Based Lipidomics: An Overview of Technological Platforms. *Metabolites* **2012,** *2*, 19-38.

123. Berry, K. A. Z.; Hankin, J. Z.; Barkley, R. M.; Spraggins, J. M.; Caprioli, R. M.; Murphy, R. C., MALDI Imaging of Lipid Biochemistry in Tissues by Mass Spectrometry. *Chem. Rev.* **2011,** *111*, 6491-6512.

124. Murphy, R. C., Tandem Mass Spectrometry of Lipids: Molecular Analysis of Complex Lipids. **2014**.

125. Gross, J. H., Tandem Mass Spectrometry. In *Mass Spectrometry*, 2nd ed.; Springer-Verlag Berlin Heidelberg: Heidelberg, 2011; pp 416-478.

126. Michalski, A.; Damoc, E.; Hauschild, J.-P.; Lange, O.; Wieghaus, A.; Makarov, A.; Nagaraj, N.; Cox, J.; Mann, M.; Horning, S., Mass Spectrometry-based Proteomics Using Q

Exactive, a High-performance Benchtop Quadrupole Orbitrap Mass Spectrometer. *Molecular & cellular proteomics : MCP* **2011,** *10*, M111.011015.

127. de Hoffman, E.; Stroobant, V., Mass Spectrometry: Principles and Applications. **2013**, 504.

128. McNaught, A. D.; Wilkinson, A., Resolution in mass spectrometry. In *IUPAC. Compendium of Chemical Terminology, 2nd ed. (the "Gold Book")*, 2.3.3 ed.; Jenkins, A., Ed. Blackwell Scientific Publications: Oxford, UK, 1997-2014.

129. Marshall, A. G.; Hendrickson, C. L., High-Resolution Mass Spectrometers. *Annu Rev Anal Chem (Palo Alto Calif)* **2008,** *1*, 20.

130. Balogh, M. P., Debating Resolution and Mass Accuracy in Mass Spectrometry. *Spectroscopy* **2004,** *19* (10), 7.

131. Price, P., Standard definitions of terms relating to mass spectrometry. *J Am Soc Mass Spectrom* **1991,** *2*, 336-348.

132. Brenton, A. G.; Godfrey, A. R., Accurate Mass Measurement: Terminology and Treatment of Data. *Journal of the American Society for Mass Spectrometry* **2010,** *21* (11), 1821-1835.

133. Makarov, A.; Denisov, E.; Lange, O., Performance Evaluation of a High-field Orbitrap Mass Analyzer. *Journal of the American Society for Mass Spectrometry* **2009,** *20*, 1391-1396.

134. Song, E.; Pyreddy, S.; Mechref, Y., Quantification of glycopeptides by multiple reaction monitoring LC-MS/MS. *Rapid Communications in Mass Spectrometry* **2013,** *26*, 1941-1954.

135. Gross, J. H., Hyphenated Methods. In *Mass Spectrometry*, 2nd ed.; Springer-Verlag Berlin Heidelberg: Heidelberg, 2011; pp 651-684.

136. Shaner, R. L.; Allegood, J. C.; Park, H.; Wang, E.; Kelly, S.; Haynes, C. a.; Sullards, M. C.; Merrill, A. H., Quantitative analysis of sphingolipids for lipidomics using triple quadrupole

and quadrupole linear ion trap mass spectrometers. *Journal of lipid research* **2009,** *50*, 1692-1707.

137. Mazereeuw, G.; Herrmann, N.; Xu, H.; Figeys, D.; Oh, P. I.; Bennett, S. A. L.; Lanctôt, K. L., Platelet-activating factors are associated with cognitive deficits in depressed coronary artery disease patients: a hypothesis-generating study. *J. Neuroinflammation* **2014,** *11*, 119.

138. Kennedy, M. A.; Moffat, T. C.; Gable, K.; Ganesan, S.; Niewola-Staszkowska, K.; Johnston, A.; Nislow, C.; Giaever, G.; Harris, L. J.; Loewith, R.; Zaremberg, V.; Harper, M. E.; Dunn, T.; Bennett, S. A.; Baetz, K., A Signaling Lipid Associated with Alzheimer's Disease Promotes Mitochondrial Dysfunction. *Sci Rep* **2016,** *6*, 19332.

139. Smith, J. C.; Hou, W.; Whitehead, S. N.; Ethier, M.; Bennett, S. A. L.; Figeys, D., Identification of lysophosphatidylcholine (LPC) and platelet activating factor (PAF) from PC12 cells and mouse cortex using liquid chromatography/multi-stage mass spectrometry (LC/MS3). *Rapid communications in mass spectrometry : RCM* **2008,** *22*, 3579-3587.

140. Hou, W.; Zhou, H.; Khalil, M. B.; Seebun, D.; Bennett, S. A. L.; Figeys, D., Lyso-form fragment ions facilitate the determination of stereospecificity of diacyl glycerophospholipids. *Rapid communications in mass spectrometry : RCM* **2011,** *25*, 205-217.

141. Chan, R. B.; Oliveira, T. G.; Cortes, E. P.; Honig, L. S.; Duff, K. E.; Small, S. A.; Wenk, M. R.; Shui, G.; Paolo, G. D., Comparative lipidomic analysis of mouse and human brain with Alzheimer's Disease. *Journal of Biological Chemistry* **2012,** *287*, 2678-2688.

142. Caprioli, R. M.; Farmer, T. B.; Gile, J., Molecular imaging of biological samples: localization of peptides and proteins using MALDI-TOF MS. *Analytical chemistry* **1997,** *69*, 4751-60.

143. Chaurand, P.; Stoeckli, M.; Caprioli, R. M., Direct profiling of proteins in biological tissue sections by MALDI mass spectrometry. *Analytical Chemistry* **1999,** *71*, 5263-5270.

144. Stoeckli, M.; Farmer, T. B.; Caprioli, R. M., Automated mass spectrometry imaging with a matrix-assisted laser desorption ionization time-of-flight instrument. *Journal of the American Society for Mass Spectrometry* **1999,** *10*, 67-71.

145. Schwartz, S. A.; Reyzer, M. L.; Caprioli, R. M., Direct tissue analysis using matrix-assisted laser desorption/ionization mass spectrometry: Practical aspects of sample preparation. *Journal of Mass Spectrometry* **2003,** *38*, 699-708.

146. Schwamborn, K.; Krieg, R. C.; Reska, M.; Jakse, G.; Knuechel, R.; Wellman, A., Identifying prostate carcinoma by MALDI-Imaging. *International journal of molecular medicine* **2007,** *20*, 155-159.

147. Wisztorski, M.; Lemaire, R.; Stauber, J., New developments in MALDI imaging for pathology proteomic studies. *Current Pharmaceutical Design* **2007,** *13*, 3317-3324.

148. Shimma, S.; Sugiura, Y.; Hayasaka, T.; Hoshikawa, Y.; Noda, T.; Setou, M., MALDI-based imaging mass spectrometry revealed abnormal distribution of phospholipids in colon cancer liver metastasis. *Journal of Chromatography B: Analytical Technologies in the Biomedical and Life Sciences* **2007,** *855*, 98-103.

149. Römpp, A.; Spengler, B., Mass spectrometry imaging with high resolution in mass and space. *Histochemistry and Cell Biology* **2013,** *139*, 759-783.

150. Goto-Inoue, N.; Hayasaka, T.; Zaima, N.; Setou, M., Imaging mass spectrometry for lipidomics. *Biochimica et biophysica acta* **2011,** *1811*, 961-9.

151. Shi, S.-R.; Liu, C.; Balgley, B.; Lee, C.; Taylor, C., Protein Extraction from Formalin-fixed, Paraffin-embedded Tissue Sections: Quality Evaluation by Mass Spectrometry. *J. Histochem. Cytochem.* **2006,** *54*, 739-743.

152. Bindhu, P.; Krishnapillai, R.; Thomas, P.; Jayanthi, P., Facts in artifacts. *J Oral Maxillofac Pathol.* **2013,** *17*, 397-401.

153. Kawamoto, T., Use of a new adhesive film for the preparation of multi-purpose fresh-frozen sections from hard tissues, whole animals, insects and plants. *Arch Histol Cytol* **2003,** *66*, 123-143.

154. Altelaar, A.; van Minnen, J.; Jiménez, C.; Heeren, R.; Piersma, S., Direct molecular imaging of lymnaea stagnalis nervous tissue at subcellular spatial resolution by mass spectrometry. *Anal Chem.* **2005,** *77*, 735-.

155. Strohalm, M.; Strohalm, J.; Kaftan, F.; Krasny, L.; Volny, M.; Novak, P.; Ulbrich, K.; Havlicek, V., Poly N-(2-hydroxypropy) methacrylamide-based tissue-embedding medium compatible with MALDI mass spectrometry imaging experiments. *Anal Chem.* **2011,** *83*, 5458-5462.

156. Canene-Adams, K., Preparation of formalin-fixed paraffin-embedded tissue for immunohistochemistry. In *Methods in Enzymology*, 1 ed.; Elsevier Inc.: San Diego, CA, USA, 2013; Vol. 533, pp 225-233.

157. Tomer, R.; Ye, L.; Hsueh, B.; Deisseroth, K., Advanced CLARITY for rapid and high-resolution imaging of intact tissues. *Nature Protocols* **2014,** *9*, 1682-97.

158. Pietrowska, M.; Gawin, M., Tissue fixed with formalin and processed without paraffin embedding is suitable for imaging of both peptides and lipids by MALDI-IMS. *Proteomic* **2016,** *16*, 1670-1677.

159. Aerni, H.-R.; Cornett, D. S.; Caprioli, R. M., Automated Acoustic Matrix Deposition for MALDI Sample Preparation. *Anal Chem* **2006,** *78*, 827-834.

160. Murphy, R. C.; Hankin, J. A.; Barkley, R. M.; Zemski Berry, K. A., MALDI imaging of lipids after matrix sublimation/deposition. *Biochim Biophys Acta* **2011,** *1811* (11), 970-5.

161. Yalcin, E. B.; de la Monte, S. M., Review of matrix-assisted laser desorption ionization-imaging mass spectrometry for lipid biochemical histopathology. *J Histochem Cytochem* **2015,** *63* (10), 762-71.

162. Yang, J.; Caprioli, R. M., Matrix sublimation/recrystallization for imaging proteins by mass spectrometry at high spatial resolution. *Anal Chem* **2011,** *83* (14), 5728-34.

163. Yang, J.; Caprioli, R. M., Matrix Pre-Coated Targets for Direct Lipid Analysis and Imaging of Tissue. *Anal Chem.* **2013,** *85*, 2907-2912.

164. Anderson, D. M. G.; Spraggins, J. M.; Rose, K. L.; Schey, K. L., High spatial resolution imaging mass spectrometry of human optic nerve lipids and proteins. *Journal of the American Society for Mass Spectrometry* **2015,** *26*, 940-947.

165. Nitin, K., Matter in our surrounding. In *Longman Science Chemistry 9*, Dorling Kindersley (India) Pvt.: Delhi, 2008; pp 14-16.

166. Brown, T. L., Intermolecular Forces: Gases. In *Chemistry: The Central*, Third ed.; Pearson Australia: Frenchs Forest, 2014; pp 360-367.

167. Inc., M. *AP / MALDI PDF + and AP / MALDI HR Source for Thermo Mass Spectrometers*; Columbia, MD, 2015.

168. Jurchen, J. C.; Rubakhin, S. S.; Sweedler, J. V., MALDI-MS imaging of features smaller than the size of the laser beam. *Journal of the American Society for Mass Spectrometry* **2005,** *16*, 1654-1659.

169. Cotter, R. J., Time-of-flight Mass Spectrometry: Instrumentation and Applications in Biological Research. **1997**, 1-350.

170. de Hoffmann, E.; Stroobant, V., The Electrostatic Trap or 'Orbitrap'. In *Mass Spectrometry: Principles and Applications*, Third ed.; John Wiley & Sons, Ltd: West Sussex, England, 2013; pp 122-125.

171. Gross, J., Isotopic Composition and Accurate Mass. In *Mass Spectrometry*, 2nd ed.; Springer-Verlag Berlin Heidelberg: Heidelberg, 2011; pp 67-116.

172. Fujimura, Y.; Miura, D., MALDI Mass Spectrometry Imaging for Visualizing In Situ Metabolism of Endogenous Metabolites and Dietary Phytochemicals. *Metabolites* **2014,** *4*, 319-46.

173. Hawkes, J. A.; Dittmar, T.; Patriarca, C.; Tranvik, L.; Bergquist, J., Evaluation of the Orbitrap Mass Spectrometer for the Molecular Fingerprinting Analysis of Natural Dissolved Organic Matter. *Analytical Chemistry* **2016,** *88*, 7698-7704.

174. Tomita, H.; Vawter, M. P.; Walsh, D. M.; Evans, S. J.; Choudary, P. V.; Li, J.; Overman, K. M.; Atz, M. E.; Myers, R. M.; Jones, E. G.; Watson, S. J.; Akil, H.; Bunney, W. E., Effect of Agonal and Postmortem Factors on Gene Expression Profile: Quality Control in Microarray Analyses of Postmortem Human Brain. *Biological psychiatry* **2004,** *55* (4), 346-352.

175. Bruder, L., Anoxia. In *Encyclopedia of Child Behavior and Development*, Goldstein, S.; Naglieri, J. A., Eds. Springer US: Boston, MA, 2011; pp 108-109.

176. Poulsen, K. A.; Young, J. F.; Theil, P.; Kolko, M.; Oksbjerg, N.; Lambert, I. H., Role of Phospholipase A2 in the Induction of Drip Loss in Porcine Muscle. *Journal of Agricultural and Food Chemistry* **2007,** *55* (5), 1970-1976.

177. Lutz, P. L.; Nilsson, G. E.; Prentice, H. M., The Brain in Crisis - Lipolysis. In *The Brain Without Oxygen: Causes of Failure-Physiological and Molecular Mechanisms for Survival*, Kluwer Academic Publishers: New York, 2007; p 90.

178. Nachas, N.; Pinson, A., Anoxic injury accelerates phosphatidylcholine degradation in cultured cardiac myocytes by phospholipase C. *FEBS Letters* **1992,** *298*, 301-305.

179. Hagve, T. A.; Sprecher, H.; Hohl, C. M., The effect of anoxia on lipid metabolism in isolated adult rat cardiac myocytes. *Journal of molecular and cellular cardiology* **1990,** *22*, 1467-75.

180. Yoshiki, A.; Moriwaki, K., Mouse Phenome Research: Implications of Genetic Background. *ILAR Journal* **2006,** *47* (2), 94-102.

181. Campbell, J. L.; Le Blanc, J. C. Y.; Kibbey, R. G., Differential mobility spectrometry: a valuable technology for analyzing challenging biological samples. *Bioanalysis* **2015,** *7* (7), 853-856.

182. Blanchard, A. P.; McDowell, G. S. V.; Valenzuela, N.; Xu, H.; Gelbard, S.; Bertrand, M.; Slater, G. W.; Figeys, D.; Fai, S.; Bennett, S. A. L., Visualization and Phospholipid Identification (VaLID): online integrated search engine capable of identifying and visualizing glycerophospholipids with given mass. *Bioinformatics* **2013,** *29* (2), 284-285.

183. Sud, M.; Fahy, E.; Cotter, D.; Brown, A.; Dennis, E. A.; Glass, C. K.; Merrill, A. H., Jr.; Murphy, R. C.; Raetz, C. R.; Russell, D. W.; Subramaniam, S., LMSD: LIPID MAPS structure database. *Nucleic Acids Res* **2007,** *35* (Database issue), D527-32.

184. Xia, J.; Psychogios, N.; Young, N.; Wishart, D. S., MetaboAnalyst: a web server for metabolomic data analysis and interpretation. *Nucleic Acids Research* **2009,** *37* (Web Server issue), W652-W660.

185. Xia, J.; Sinelnikov, I. V.; Han, B.; Wishart, D. S., MetaboAnalyst 3.0—making metabolomics more meaningful. *Nucleic Acids Research* **2015,** *43* (Web Server issue), W251-W257.

186. Xia, J.; Wishart, D. S., Using MetaboAnalyst 3.0 for Comprehensive Metabolomics Data Analysis. *Current protocols in bioinformatics* **2016,** *55*, 14.10.1-14.10.91.

187. Xia, J.; Wishart, D. S., Web-based inference of biological patterns, functions and pathways from metabolomic data using MetaboAnalyst. *Nat. Protocols* **2011,** *6* (6), 743-760.

188. Xia, J.; Wishart, D. S., Metabolomic data processing, analysis, and interpretation using MetaboAnalyst. *Current protocols in bioinformatics* **2011,** *Chapter 14*, Unit 14.10.

189. de Hoon, M. J. L.; Imoto, S.; Nolan, J.; Miyano, S., Open source clustering software. *Bioinformatics* **2004,** *20* (9), 1453-1454.

190. Saldanha, A. J., Java Treeview—extensible visualization of microarray data. *Bioinformatics* **2004,** *20* (17), 3246-3248.

191. Benjamini, Y.; Krieger, A. M.; Yekutieli, D., Adaptive linear step-up procedures that control the false discovery rate. *Biometrika* **2006,** *93* (3), 491-507.

192. Rhoades, R. H., Sodium Pentobarbital. In *Euthanasia Reference Manual*, Second ed.; The Humane Society of the United States: 2013; p 95.

193. Abdollahi, M.; Baghaei, A., Pentobarbital Sodium A2 - Wexler, Philip. In *Encyclopedia of Toxicology (Third Edition)*, Academic Press: Oxford, 2014; pp 783-785.

194. Lindsberg, P. J.; Hallenbeck, J. M.; Feuerstein, G., Platelet-activating factor in stroke and brain injury. *Annals of neurology* **1991,** *30* (2), 117-29.

195. Bazan, N. G.; Rodriguez de Turco, E. B.; Allan, G., Mediators of injury in neurotrauma: intracellular signal transduction and gene expression. *Journal of neurotrauma* **1995,** *12* (5), 791-814.

196. Farooqui, A. A.; Horrocks, L. A., Involvement of Phospholipids and Phospholipases A2 in Neurological Disorders. In *Glycerophospholipids in the Brain: Phospholipases A2 in Neurological Disorders*, Springer Science & Business Media: New York, 2007; pp 239-260.

197. Alexandrov, P. N.; Cui, J.-G.; Lukiw, W. J., Hypoxia-sensitive domain in the human cytosolic phospholipase A2 promoter. *Neuroreport* **2006,** *17* (3), 303-307.

198. Farooqui, A. A.; Horrocks, L. A., Phospholipases A2 in Brain. In *Glycerophospholipids in the Brain: Phospholipases A2 in Neurological Disorders*, Springer: New York, 2007; pp 67-92.

199. Farooqui, A. A.; Horrocks, L. A., Glycerophospholipids and Phospholipases A2 in Neuropsychiatric Disorders. In *Glycerophospholipids in the Brain: Phospholipases A2 in Neurological Disorders*, Springer Science & Business Media: New York, 2007; pp 341-366.

200. Farooqui, A. A.; Horrocks, L. A.; Farooqui, T., Glycerophospholipids in brain: their metabolism, incorporation into membranes, functions, and involvement in neurological disorders. *Chemistry and physics of lipids* **2000,** *106* (1), 1-29.

201. Farooqui, A. A.; Horrocks, L. A.; Farooqui, T., Deacylation and reacylation of neural membrane glycerophospholipids. *Journal of molecular neuroscience : MN* **2000,** *14* (3), 123-35.

202. Zaleska, M. M.; Wilson, D. F., Lipid hydroperoxides inhibit reacylation of phospholipids in neuronal membranes. *Journal of neurochemistry* **1989,** *52* (1), 255-60.

203. Aguilar, P. S.; De Mendoza, D., Control of fatty acid desaturation: a mechanism conserved from bacteria to humans. *Molecular Microbiology* **2006,** *62* (6), 1507-1514.

204. Reis, A.; Spickett, C. M., Chemistry of phospholipid oxidation. *Biochim Biophys Acta* **2012,** *1818* (10), 2374-87.

205. Farooqui, A. A.; Farooqui, T.; Horrocks, L. A., Biosynthesis of Plasmalogens in Brain. In *Metabolism and Functions of Bioactive Ether Lipids in the Brain*, Springer New York: New York, NY, 2008; pp 17-37.

206. Braverman, N. E.; Moser, A. B., Functions of plasmalogen lipids in health and disease. *Biochim Biophys Acta* **2012,** *1822* (9), 1442-52.

207. Farooqui, A. A.; Farooqui, T.; Horrocks, L. A., Occurrence and Importance of Ether Lipids in Brain. In *Metabolism and Functions of Bioactive Ether Lipids in the Brain*, Springer New York: New York, NY, 2008; pp 1-16.

208. Hardeman, D.; van den Bosch, H., Topography of ether phospholipid biosynthesis. *Biochim Biophys Acta* **1989,** *1006* (1), 1-8.

209. Broniec, A.; Klosinski, R.; Pawlak, A.; Wrona-Krol, M.; Thompson, D.; Sarna, T., Interactions of plasmalogens and their diacyl analogs with singlet oxygen in selected model systems. *Free radical biology & medicine* **2011,** *50* (7), 892-8.

210. Grimm, M. O.; Grosgen, S.; Riemenschneider, M.; Tanila, H.; Grimm, H. S.; Hartmann, T., From brain to food: analysis of phosphatidylcholins, lyso-phosphatidylcholins and phosphatidylcholin-plasmalogens derivates in Alzheimer's disease human post mortem brains and mice model via mass spectrometry. *Journal of chromatography. A* **2011,** *1218* (42), 7713-22.

211. McCord, J. M., The evolution of free radicals and oxidative stress. *The American journal of medicine* **2000,** *108* (8), 652-9.

212. Gilgun-Sherki, Y.; Melamed, E.; Offen, D., Oxidative stress induced-neurodegenerative diseases: the need for antioxidants that penetrate the blood brain barrier. *Neuropharmacology* **2001,** *40* (8), 959-75.

213. Muller, F., The nature and mechanism of superoxide production by the electron transport chain: Its relevance to aging. *Journal of the American Aging Association* **2000,** *23* (4), 227-253.

214. Murphy, Michael P., How mitochondria produce reactive oxygen species. *Biochemical Journal* **2009,** *417* (Pt 1), 1-13.

215. Christie, W. W.; Han, X., Chapter 1 - Lipids: their structures and occurrence. In *Lipid Analysis (Fourth edition)*, Woodhead Publishing: 2012; pp 3-19.

216. Leventis, P. A.; Grinstein, S., The distribution and function of phosphatidylserine in cellular membranes. *Annual review of biophysics* **2010,** *39*, 407-27.

217. Corda, D.; Zizza, P.; Varone, A.; Bruzik, K. S.; Mariggio, S., The glycerophosphoinositols and their cellular functions. *Biochemical Society transactions* **2012,** *40* (1), 101-7.

218. D'Souza, K.; Epand, R. M., Enrichment of phosphatidylinositols with specific acyl chains. *Biochim Biophys Acta* **2014,** *1838* (6), 1501-8.

219. Aichler, M.; Walch, A., MALDI Imaging mass spectrometry: current frontiers and perspectives in pathology research and practice. *Laboratory investigation; a journal of technical methods and pathology* **2015,** *95*, 422-31.

220. Rojas-Chertó, M.; Kasper, P. T.; Willighagen, E. L.; Vreeken, R. J.; Hankemeier, T.; Rejimers, T. H., Elemental composition determination based on MS(n). *Bioinformatics* **2011,** *27*, 2376-2383.

221. Cicchi, R.; Sampson, D.; Massi, D.; Pavone, F., Contrast and depth enhancement in two-photon microscopy of human skin ex vivo by use of optical clearing agents. *Optics express* **2005,** *13*, 2337-44.

222. Tuchin, V. V., A clear vision for laser diagnostics. *IEEE J. Sel. Top. Quantum Electron.* **2007,** *13*, 1621-1628.

223. Parra, S. G.; Chia, T. H.; Zinter, J. P.; Levene, M. J., Multiphoton microscopy of cleared mouse organs. *Journal of biomedical optics* **2010,** *15*, 036017.

224. Chung, K.; Wallace, J.; Kim, S.-Y.; Kalyanasundaram, S.; Andalman, A. S.; Davidson, T. J.; Mirzabekov, J. J.; Zalocusky, K. A.; Mattis, J.; Denisin, A. K.; Pak, S.; Bernstein, H.; Ramakrishnan, C.; Grosenick, L.; Gradinaru, V.; Deisseroth, K., Structural and molecular interrogation of intact biological systems. *Nature* **2013,** *497*, 332-7.

225. Zhang, M. D.; Tortoriello, G.; Hsueh, B.; Tomer, R.; Ye, L.; Mitsios, N.; Borgius, L.; Grant, G.; Kiehn, O.; Watanabe, M.; Uhlén, M.; Mulder, J.; Deisseroth, K.; Harkany, T.; Hokfelt, T. G., Neuronal calcium-binding proteins 1/2 localize to dorsal root ganglia and excitatory spinal neurons and are regulated by nerve injury. *Proc Natl Acad Sci U S A.* **2014,** *111*, E149-58.

226. Epp, J. R.; Niibori, Y.; Liz Hsiang, H. L.; Mercaldo, V.; Deisseroth, K.; Josselyn, S. A.; Frankland, P. W., Optimization of CLARITY for Clearing Whole-Brain and Other Intact Organs(1,2,3). *eNeuro* **2015,** *2*, pii: ENEURO.0022-15.2015.

227. Saboor, F.; Reckmann, A. N.; Tomczyk, C. U.; Peters, D. M.; Weissmann, N.; Kaschtanow, A.; Schermuly, R. T.; Michurina, T. V.; Enikolopov, G.; Muller, D.; Mietens, A.; Middendorff, R., Nestin-expressing vascular wall cells drive development of pulmonary hypertension. *Eur Respir J.* **2016,** *47*, 876-88.

228. Lemaire, R.; Desmons, a.; Tabet, J. C.; Day, R.; Salzet, M.; Fournier, I., Direct Analysis and MALDI Imaging of Formalin-Fixed , Paraffin-Embedded Tissue Sections research articles. **2007**, 1295-1305.

229. Myers, D. S.; Ivanova, P. T.; Milne, S. B.; Brown, H. A., Quantitative analysis of glycerophospholipids by LC-MS: Acquisition, data handling, and interpretation. *Biochimica et Biophysica Acta - Molecular and Cell Biology of Lipids* **2011,** *1811*, 748-757.

230. Horai, H.; Arita, M.; Kanaya, S.; Nihei, Y.; Ikeda, T.; Suwa., K.; Ojima, Y.; Tanaka, K.; Tanaka, S.; Aoshima, K.; Oda, Y.; Kakazu, Y.; Kusano, M.; Tohge, T.; Matsuda, F.; Sawada, Y.; Hirai, M. Y.; Nakanishi, H.; Ikeda, K.; Akimoto, N.; Maoka, T.; Takahashi, H.; Ara, T.; Sakurai, N.; Suzuki, H.; Shibata, D.; Neumann, S.; Iida, T.; Tanaka, K.; Funatsu, K.; Matsuura, F.; Soga, T.; Taguchi, R.; Saito, K.; Nishioka, T., MassBank: A public repository for sharing mass spectral data for life sciences. *J. Mass Spectrom.* **2010,** *45*, 703-714.

231. Dwivedi, P.; Puzon, G.; Tam, M.; Langlais, D.; Jackson, S.; Kaplan, K.; Siems, W. F.; Schultz, A. J.; Xun, L.; Woods, A.; Hill, H. H., Jr., Metabolic profiling of Escherichia coli by ion mobility-mass spectrometry with MALDI ion source. *J Mass Spectrom* **2010,** *45* (12), 1383-93.

232. Ye, H.; Wang, J.; Greer, T.; Strupat, K.; Li, L., Visualizing neurotransmitters and metabolites in the central nervous system by high resolution and high accuracy mass spectrometric imaging. *ACS Chemical Neuroscience* **2013,** *4*, 1049-1056.

233. Wishart, D. S.; Knox, C.; Guo, A. C.; al., e., HMDB: a knowledgebase for the human metabolome. *Nucleic Acid Res* **2009,** *37*, D603-610.

234. Wishart, D. S.; Jewison, T.; Guo, A. C.; al., e., HMDB 3.0 - The Human Metabolome Database in 2013. *Nucleic Acid Res* **2013,** *41*, D801-7.

235. Wishart, D. S.; Tzur, D.; Knox, C.; al., e., HMDB: the Human Metabolome Database. *Nucleic Acid Res* **2007,** *35*, D521-6.

236. Schiller, J.; Suss, R.; Arnhold, J.; Fuchs, B.; Lessig, J.; Muller, M.; Petkovic, M.; Spalteholz, H.; Zschornig, O.; Arnold, K., Matrix-assisted laser desorption and ionization time-of-flight (MALDI-TOF) mass spectrometry in lipid and phospholipid research. *Prog Lipid Res* **2004,** *43* (5), 449-88.

237. Ferreira, C. R.; Saraiva, S. a.; Catharino, R. R.; Garcia, J. S.; Gozzo, F. C.; Sanvido, G. B.; Santos, L. F. a.; Lo Turco, E. G.; Pontes, J. H. F.; Basso, A. C.; Bertolla, R. P.; Sartori, R.; Guardieiro, M. M.; Perecin, F.; Meirelles, F. V.; Sangalli, J. R.; Eberlin, M. N., Single embryo and oocyte lipid fingerprinting by mass spectrometry. *Journal of lipid research* **2010,** *51*, 1218-1227.

238. McDowell, G. S. V.; Blanchard, A. P. B.; Figeys, D.; Fai, S.; Bennett, S. A. L., Advancing Lipidomic Bioinformatic Technologies: Visu- alization and Phospholipid Identification (VaLID) version 3.0. **2014**, 670-680.

239. Paglia, G.; D'Apolito, O.; Gelzo, M.; Dello Russo, A.; Corso, G., Direct analysis of sterols from dried plasma/blood spots by an atmospheric pressure thermal desorption chemical ionization mass spectrometry (APTDCI-MS) method for a rapid screening of Smith–Lemli–Opitz syndrome. *The Analyst* **2010,** *135*, 789.

240. Liu, Q.; Xiao, Y.; Pagan-Miranda, C.; Chiu, Y. M.; He, L., Metabolite Imaging Using Matrix-Enhanced Surface-Assisted Laser Desorption/Ionization Mass Spectrometry (ME-SALDI-MS). *Journal of the American Society for Mass Spectrometry* **2009,** *20*, 80-88.

241. Stoeckli, M.; Staab, D.; Schweitzer, A., Compound and metabolite distribution measured by MALDI mass spectrometric imaging in whole-body tissue sections. *International Journal of Mass Spectrometry* **2007,** *260*, 195-202.

242. Ye, H.; Greer, T.; Li, L., Probing neuropeptide signaling at the organ and cellular domains via imaging mass spectrometry. *Journal of Proteomics* **2012,** *75*, 5014-5026.

243. Smith, L. L., Cholesterol Purity and Stability. In *Cholesterol Autoxidation*, Springer Science & Business Media: New York, 1981; pp 459-522.

244. Touboul, D.; Halgand, F.; Brunelle, A.; Kersting, R.; Tallarek, E.; Hagenhoff, B.; Laprévote, O., Tissue Molecular Ion Imaging by Gold Cluster Ion Bombardment. *Analytical Chemistry* **2004,** *76*, 1550-1559.

245. Baker, M. J.; Zheng, L.; Winograd, N.; Lockyer, N. P.; Vickerman, J. C., Mass spectral imaging of glycophospholipids, cholesterol, and glycophorin A in model cell membranes. *Langmuir* **2008,** *24*, 11803-11810.

246. Radowska, P. D.; Seah, M. P.; Vorng, J.-L.; Gilmore, I. S., Determination of the sputtering yield of cholesterol using Arn(+) and C60+(+) cluser ions. *Analyst* **2016,** *141*, 4893-4901.

247. Garrett, T. J.; Prieto-Conaway, M. C.; Kovtoun, V.; Bui, H.; Izgarian, N.; Stafford, G.; Yost, R. A., Imaging of small molecules in tissue sections with a new intermediate-pressure MALDI linear ion trap mass spectrometer. *International Journal of Mass Spectrometry* **2007,** *260* (2-3), 166-176.

248. Brown, D. M.; Todd, A. R., 13. Nucleotides. Part X. Some observations on the structure and chemical behaviour of the nucleic acids. *Journal of the Chemical Society (Resumed)* **1952,** (0), 52-58.

249. Kingsbury, A. E.; Foster, O. J.; Nisbet, A. P.; Cairns, N.; Bray, L.; Eve, D. J.; Lees, A. J.; Marsden, C. D., Tissue pH as an indicator of mRNA preservation in human post-mortem brain. *Brain research. Molecular brain research* **1995,** *28* (2), 311-8.

250. Monoranu, C. M.; Apfelbacher, M.; Grünblatt, E.; Puppe, B.; Alafuzoff, I.; Ferrer, I.; Al-Saraj, S.; Keyvani, K.; Schmitt, A.; Falkai, P.; Schittenhelm, J.; Halliday, G.; Kril, J.; Harper, C.; McLean, C.; Riederer, P.; Roggendorf, W., pH measurement as quality control on human post mortem brain tissue: a study of the BrainNet Europe consortium. *Neuropathology and applied neurobiology* **2009,** *35* (3), 329-337.

251. Ervin, J. F.; Heinzen, E. L.; Cronin, K. D.; Goldstein, D.; Szymanski, M. H.; Burke, J. R.; Welsh-Bohmer, K. A.; Hulette, C. M., Postmortem delay has minimal effect on brain RNA integrity. *Journal of neuropathology and experimental neurology* **2007,** *66* (12), 1093-9.

252. Durrenberger, P. F.; Fernando, S.; Kashefi, S. N.; Ferrer, I.; Hauw, J. J.; Seilhean, D.; Smith, C.; Walker, R.; Al-Sarraj, S.; Troakes, C.; Palkovits, M.; Kasztner, M.; Huitinga, I.; Arzberger, T.; Dexter, D. T.; Kretzschmar, H.; Reynolds, R., Effects of antemortem and postmortem variables on human brain mRNA quality: a BrainNet Europe study. *Journal of neuropathology and experimental neurology* **2010,** *69* (1), 70-81.

253. Preece, P.; Cairns, N. J., Quantifying mRNA in postmortem human brain: influence of gender, age at death, postmortem interval, brain pH, agonal state and inter-lobe mRNA variance. *Brain research. Molecular brain research* **2003,** *118* (1-2), 60-71.

254. Birdsill, A. C.; Walker, D. G.; Lue, L.; Sue, L. I.; Beach, T. G., Postmortem interval effect on RNA and gene expression in human brain tissue. *Cell and tissue banking* **2011,** *12* (4), 311-8.

255. Nagy, C.; Maheu, M.; Lopez, J. P.; Vaillancourt, K.; Cruceanu, C.; Gross, J. A.; Arnovitz, M.; Mechawar, N.; Turecki, G., Effects of postmortem interval on biomolecule integrity in the brain. *Journal of neuropathology and experimental neurology* **2015,** *74* (5), 459-69.

256. Crecelius, A.; Gotz, A.; Arzberger, T.; Frohlich, T.; Arnold, G. J.; Ferrer, I.; Kretzschmar, H. A., Assessing quantitative post-mortem changes in the gray matter of the human frontal cortex proteome by 2-D DIGE. *Proteomics* **2008,** *8* (6), 1276-91.

257. Hynd, M. R.; Lewohl, J. M.; Scott, H. L.; Dodd, P. R., Biochemical and molecular studies using human autopsy brain tissue. *Journal of neurochemistry* **2003,** *85* (3), 543-62.

258. Briggs, M. T.; Ho, Y. Y.; Kaur, G.; Oehler, M. K.; Everest-Dass, A. V.; Packer, N. H.; Hoffmann, P., N-Glycan matrix-assisted laser desorption/ionization mass spectrometry imaging protocol for formalin-fixed paraffin-embedded tissues. *Rapid communications in mass spectrometry : RCM* **2017,** *31* (10), 825-841.

259. Ermini, L.; Morganti, E.; Post, A.; Yeganeh, B.; Caniggia, I.; Leadley, M.; Faria, C. C.; Rutka, J. T.; Post, M., Imaging mass spectrometry identifies prognostic ganglioside species in rodent intracranial transplants of glioma and medulloblastoma. *PloS one* **2017,** *12* (5), e0176254.

260. Hong, J. H.; Kang, J. W.; Kim, D. K.; Baik, S. H.; Kim, K. H.; Shanta, S. R.; Jung, J. H.; Mook-Jung, I.; Kim, K. P., Global changes of phospholipids identified by MALDI imaging mass

spectrometry in a mouse model of Alzheimer's disease. *Journal of Lipid Research* **2016,** *57*, 36-45.

261. Zemski Berry, K. A.; Murphy, R. C.; Kosmider, B.; Mason, R. J., Lipidomic characterization and localization of phospholipids in the human lung. *J Lipid Res* **2017,** *58* (5), 926-933.

262. Schober, Y.; Guenther, S.; Spengler, B.; Römpp, A., Single cell matrix-assisted laser desorption/ionization mass spectrometry imaging. *Analytical chemistry* **2012,** *84*, 6293-7.

263. Chagovets, V.; Lisa, M.; Holcapek, M., Effects of fatty acyl chain length, double-bond number and matrix on phosphatidylcholine responses in matrix-assisted laser desorption/ionization on an Orbitrap mass spectrometer. *Rapid communications in mass spectrometry : RCM* **2015,** *29* (24), 2374-84.

264. Yuki, D.; Sugiura, Y.; Zaima, N.; Akatsu, H.; Takei, S.; Yao, I.; Maesako, M.; Kinoshita, A.; Yamamoto, T.; Kon, R.; Sugiyama, K.; Setou, M., DHA-PC and PSD-95 decrease after loss of synaptophysin and before neuronal loss in patients with Alzheimer's disease. *Scientific reports* **2014,** *4*, 7130.

265. Porta, T.; Lesur, A.; Varesio, E.; Hopfgartner, G., Quantification in MALDI-MS imaging: what can we learn from MALDI-selected reaction monitoring and what can we expect for imaging? *Anal Bioanal Chem* **2015,** *407* (8), 2177-87.

266. Williams, T. L.; Andrzejewski, D.; Lay, J. O.; Musser, S. M., Experimental factors affecting the quality and reproducibility of MALDI TOF mass spectra obtained from whole bacteria cells. *J Am Soc Mass Spectrom* **2003,** *14* (4), 342-51.

267. McDonnell, L. A.; van Remoortere, A.; van Zeijl, R. J. M.; Deelder, A. M., Mass Spectrometry Image Correlation: Quantifying Colocalization. *Journal of Proteome Research* **2008,** *7* (8), 3619-3627.

268. Minerva, L.; Ceulemans, A.; Baggerman, G.; Arckens, L., MALDI MS imaging as a tool for biomarker discovery: methodological challenges in a clinical setting. *Proteomics. Clinical applications* **2012,** *6* (11-12), 581-95.

269. Lietz, C. B.; Gemperline, E.; Li, L., Qualitative and quantitative mass spectrometry imaging of drugs and metabolites. *Advanced drug delivery reviews* **2013,** *65* (8), 1074-1085.

"A hundred times every day I remind myself that my inner and outer life depend on the labours of other men, living and dead, and that I must exert myself in order to give in the same measure as I have received and am still receiving."

Albert Einstein